PDF and QCD effects in the precision measurement of the W boson mass at CDF

Daniel Beecher

Submitted for the degree of Doctor of Philosophy

University College London

I, Daniel Beecher, confirm that the work presented in this thesis is my own. Where information has been derived from other sources, I confirm that this has been indicated in the thesis.

ABSTRACT

A sample of $W \to e\nu$ ($W \to \mu\nu$) and $Z^0 \to e^+e^-$ ($Z^0 \to \mu^+\mu^-$) events recorded by the CDF detector for $p\bar{p}$ collisions at $\sqrt{\hat{s}} = 1.96$ TeV with a total integrated luminosity of 2.3 fb^{-1} are used to evaluate the systematic uncertainty in the determination of the W boson mass arising from uncertainties in the parton distribution functions and higher-order QCD effects. The systematic contribution of PDFs is determined to be 10 MeV for MSTW2008 NLO and 12 MeV for CTEQ6.6. The total systematic contribution arising from higher-order QCD effects in 9 MeV.

The unfolded Z^0 transverse momentum distribution is presented, and estimates of parameters in a phenomenological model describing low transverse momentum Z^0 events are extracted.

Dedicated to Courtney

Acknowledgements

I would like to thank all who have helped me during the years of my study. In particular I would like to thank my supervisor for his patience and guidance. The rest of the CDF team at UCL also deserve thanks: Dave, Emily, Sarah, Tom and Troy. In particular, I thank Ilija for his taxi service while out in Chicago braving the winter snow storms.

I also must thank Louise for picking up where Ilija left off, and for the many cups of coffee. My stay in Chicago would not have been as entertaining without Bo, Joey and Toby so they deserve a mention as well.

But most of all I thank my family for their support and patience.

Contents

List of Figures

List of Tables

Chapter 1

Standard model of particle physics

1.1 Introduction

One of the lasting ideas of the ancient world was that all things were affected by four distinct forces: earth, air, wind and water. It is an amusing coincidence that modern physics also refers to four forces: the electromagnetic interaction that provides the illusion of solid structure when objects consist mainly of empty space; the strong interaction that binds atomic nuclei; the weak interaction that the world primarily encounters through radioactivity; and gravity, the force that attracts matter together.

The first three of these forces, electromagnetic, weak and strong, are described by a well tested framework, the standard model of particle physics. Gravity is described by the general theory of relativity and attempts to merge it with the standard model have so far failed; however, the influence of gravity in the regime described by the standard model on Earth is very weak, and it is safely neglected.

1.2 Particles

The particles in the standard model can be separated into three groups: leptons, quarks and gauge bosons. Together the leptons and quarks are known as fermions, spin-$\frac{1}{2}$ particles that obey Fermi-Dirac statistics. Correspondingly, bosons have integer spin and obey Bose-Einstein statistics.

1.2.1 Quarks

Quarks, exotically named by Murray Gell-Mann, are one half of the family of fermions. There are three families of quarks each successively more massive than the next: up and down; charm and strange; top and bottom. The up, charm and top quarks all have $\frac{2}{3}$ electric charge, the down, strange and bottom quarks all have -$\frac{1}{3}$ electric charge. The interaction of quarks is predominantly via the strong force. All quarks carry one of the three colour charges.

The lightest of the quark families, the up and down quarks, are the most abundant. The strange, charm and bottom quarks were added to the list of known quarks during the 40s, 60s and 70s, but it was not until the discovery of the top quark at the Tevatron in 1995 [1, 2] that the third generation was complete.

Why there are only three families of quarks remains a mystery. An additional fourth family of quarks is permitted in speculative unification models with masses around 220–280 GeV [3]; however, attempts to find a fourth family of heavier quarks have set a lower limit of 250 GeV on the masses of additional bottom-like [4, 5, 6] or top-like [4, 7] quarks.

1.2.2 Leptons

The other half of the fermion family are the leptons. As with the quarks, the leptons exist in three families: a charged lepton, the electron, muon and tau;

and an associated neutrino of the same flavour.

The electron, discovered by Thomson in the late 19th century, was known about before all of the quarks. It, along with all of the other charged leptons, has a -1 electric charge. The charged leptons interact via the electromagnetic and weak interaction but not via the strong interaction. The neutrinos, originally posited by Pauli to preserve conservation laws in β-decay, have no electric charge and only interact via the weak interaction making them very elusive objects. Neutrinos were originally thought to be massless; however, non-zero differences between neutrino masses were suggested by some theorists to be consistent with the standard model [8]. The observation of neutrino flavour oscillation in the late 20th century confirmed the existence of these mass differences and of the existence of massive neutrinos [9, 10].

1.3 Forces

As previously mentioned, there are three forces in the standard model, each described by a quantum field theory: the strong interaction is described by quantum chromodynamics (QCD) [11]; the electromagnetic interaction is described by quantum electrodynamics (QED); and the weak interaction is described by the electroweak theory of Glashow [12], Weinberg [13] and Salam [14]. Each of these interactions are mediated by the exchange of gauge bosons, integer-spin carriers of force.

1.3.1 Quantum electrodynamics

Quantum electrodynamics governs the interaction of leptons and quarks. It is a quantum field theory that obeys U(1) symmetry and has the following Lagrangian:

$$\mathcal{L} = \bar{\psi}\left(i\gamma^{\mu}D_{\mu} - m\right)\psi - \frac{1}{4}F_{\mu\nu}F^{\mu\nu} \tag{1.1}$$

where $F_{\mu\nu} = \partial_\mu A_\nu - \partial_\nu A_\mu$ is the field strength tensor and the covariant derivative, D_μ, is introduced to maintain local gauge invariance[1] of the Lagrangian:

$$D_\mu = \partial_\mu - ieA_\mu. \tag{1.2}$$

The A_μ field introduced in the covariant derivative can be identified with the photon and it is the mediator of the electromagnetic force. The photon is required to be massless because terms in the QED Lagrangian that would grant mass to the photon, such as $m^2 A_\mu A^\mu$, break the local gauge invariance of QED.

1.3.2 Quantum chromodynamics

The interaction of quarks is described by quantum chromodynamics (QCD). Each quark carries one of three colour charges usually called red, green and blue. QCD is a quantum field theory that obeys SU(3) symmetry and has the following Lagrangian:

$$\mathcal{L} = \bar{\psi}\left(i\gamma^\mu D_\mu - m\right)\psi - \frac{1}{4}G^a_{\mu\nu}G^{\mu\nu}_a \tag{1.3}$$

where eight gluon fields, $G^a_{\mu\nu}$, are introduced. The covariant derivative is

$$D_\mu = \partial_\mu - igT_a G^a_\mu \tag{1.4}$$

where T_a is one of the eight non-commuting generators of SU(3) in a traceless matrix representation. As with QED, the introduction of mass terms for any of the gluon fields breaks the local gauge invariance of QCD which implies that the gluons are massless. The gluon field tensor is

$$G^a_{\mu\nu} = \partial_\mu G^a_\nu - \partial_\nu G^a_\mu - g f_{abc} G^b_\mu G^c_\nu \tag{1.5}$$

[1] Local gauge invariance is satisfied when a local phase dependence imposed on the interacting fields, $\psi \to e^{i\alpha(x)}\psi$, leaves the Lagrangian unchanged.

where $gf_{abc}G^b_\mu G^c_\nu$ represents the gluon self-interaction which arises from the non-Abelian nature of the generators: $[T_a, T_b] = f_{abc}T_c$. These self-interaction terms missing in QED permit the gluon to interact with other gluons.

1.3.3 Electroweak interaction

The electroweak theory is an extension of QED which unifies electromagnetic and weak interactions. It was developed separately by Weinberg, Glashow and Salam during the 1970s. It is a quantum field theory that obeys SU(2)×U(1) symmetries where the U(1) group has an associated field, B_μ, and the SU(2) group has three fields, W^i_μ. As with QED and QCD, a Lagrangian can be constructed:

$$\mathcal{L} = \bar{\psi}\left(i\gamma^\mu D_\mu - m\right)\psi - \frac{1}{4}B_{\mu\nu}B^{\mu\nu} - \frac{1}{4}W^i_{\mu\nu}W^{i,\mu\nu} \tag{1.6}$$

where the field strength tensors are

$$W^i_{\mu\nu} = \partial_\mu W^i_\nu - \partial_\nu W^i_\mu - g_W \epsilon_{ijk} W^j_\mu W^k_\nu \tag{1.7}$$

$$B_{\mu\nu} = \partial_\mu B_\nu - \partial_\nu B_\mu \tag{1.8}$$

following the same structure for U(1) in QED and a similar structure from QCD for SU(2). The three W^i generators have a matrix representation, T_i, where T is called weak isospin and has the following commutation relations:

$$[W_i, W_k] = \epsilon_{ijk} W_i \tag{1.9}$$

where

$$\epsilon_{ijk} = \begin{cases} +1 & \text{if } ijk \text{ is 123, 231 or 312} \\ -1 & \text{if } ijk \text{ is 321, 213 or 132} \\ 0 & \text{Otherwise} \end{cases} . \tag{1.10}$$

With these the covariant derivative used to preserve the local gauge invariance of Equation (1.6) can be constructed:

$$D_\mu = \delta_{ij}\partial_\mu + ig_W \left(T \cdot W_\mu\right)_{ij} + i\delta_{ij} Y g'_W B_\mu \tag{1.11}$$

where g_W is the coupling strength of the SU(2) interaction, g'_W is the coupling strength of the U(1) interaction, and Y is weak hypercharge, the charge of the U(1) interaction. Weak hypercharge is related to the third component of weak isospin so that

$$Q = \frac{Y}{2} + T_3 \tag{1.12}$$

where Q is the electric charge and all are conserved quantum numbers in weak interactions.

Right-handed leptons form isospin singlets and left-handed leptons form isospin doublets:

$$\psi_L = \begin{pmatrix} \nu_e \\ e^- \end{pmatrix}, \begin{pmatrix} \nu_\mu \\ \mu^- \end{pmatrix}, \begin{pmatrix} \nu_\tau \\ \tau^- \end{pmatrix} \text{ and} \tag{1.13}$$

$$\psi_R = e^-, \mu^-, \tau^-. \tag{1.14}$$

Left-handed quarks also form isospin doublets:

$$\psi_L = \begin{pmatrix} u \\ d' \end{pmatrix}, \begin{pmatrix} c \\ s' \end{pmatrix}, \begin{pmatrix} t \\ b' \end{pmatrix} \tag{1.15}$$

where the primed quarks are weak eigenstates. These weak eigenstates that take part in the electroweak interaction are related to the mass eigenstates by the Cabbibo-Kobayashi-Maskawa (CKM) [15, 16] matrix:

$$\begin{pmatrix} d' \\ s' \\ b' \end{pmatrix} = \begin{pmatrix} V_{ud} & V_{us} & V_{ub} \\ V_{cd} & V_{cs} & V_{cb} \\ V_{td} & V_{ts} & V_{tb} \end{pmatrix} \begin{pmatrix} d \\ s \\ b \end{pmatrix}. \tag{1.16}$$

which has a unitarity constraint, $V^\dagger V = 1$, and leads to the following relations: $\sum_{i=1}^{3} |V_{ij}|^2 = 1$, $\sum_{j=1}^{3} |V_{ij}|^2 = 1$, and $\sum_{k=i}^{3} V_{ki}^* V_{kj} = 0$ for $i \neq j$.

The W_μ^1 and W_μ^2 fields can be re-written as:

$$W_\mu^\pm = \frac{1}{\sqrt{2}} \left(W_\mu^1 \mp W_\mu^2 \right) \tag{1.17}$$

and the remaining W_μ^3 field can be mixed with B_μ to form:

$$A_\mu = \cos\theta_W B_\mu + \sin\theta_W W_\mu^3 \text{ and} \tag{1.18}$$

$$Z_\mu = -\sin\theta_W B_\mu + \cos\theta_W W_\mu^3. \tag{1.19}$$

This allows four massless bosons to be identified with the electroweak interaction: W_μ^+, W_μ^-, Z_μ and A_μ where θ_W is the Weinberg angle or weak mixing angle. The Weinberg angle is related to ratio of the electroweak coupling strengths:

$$\sin\theta_W = \frac{g'_W}{\sqrt{g_W^2 + g_W'^2}} \text{ and} \tag{1.20}$$

$$\cos\theta_W = \frac{g_W}{\sqrt{g_W^2 + g_W'^2}}, \tag{1.21}$$

and links the weak interaction coupling strengths with the coupling of QED:

$$e = g_W \sin\theta_W = g'_W \cos\theta_W. \tag{1.22}$$

1.3.4 Higgs mechanism

The short range of the weak interaction had lead theorists to believe that it was mediated by massive bosons, a view that was later confirmed by the observation of the massive W and Z^0 bosons by UA1 [17, 18] and UA2 [19, 20] at CERN's Super Proton Synchrotron (SPS). As with QED and QCD, the addition of boson mass terms would break the local gauge invariance of the corresponding Lagrangian.

This problem had already been fixed by means of the Higgs mechanism. A complex doublet of scalar fields is added to the SU(2)×U(1) electroweak Lagrangian. A Higgs potential of the form $\mathcal{V}\left(\phi^\dagger\phi\right) = \lambda\left(\phi^\dagger\phi\right)^2 - \mu^2\phi^\dagger\phi$ is added to the covariant derivative in Equation (1.11). When $\mu^2 > 0$ this forms

a characteristic "Mexican hat" potential well with a minimum not located at $\phi = 0$; instead there are degenerate minima at:

$$|\phi| = \sqrt{\frac{\mu^2}{\lambda}} = \frac{v}{\sqrt{2}}. \tag{1.23}$$

The SU(2)×U(1) symmetry is broken by picking one of the minima and expanding around this minimum. The electroweak Lagrangian acquires additional terms [11]:

$$\mathcal{L}_M = \frac{g_W^2 v^2}{4} W_\mu^+ W^{-\mu} + \frac{(g_W^2 + g_W'^2)\, v^2}{8} Z_\mu Z^\mu \tag{1.24}$$

which correspond to W and Z^0 bosons with masses given by:

$$M_W = \frac{1}{2} v g_W \text{ and} \tag{1.25}$$

$$M_Z = \frac{1}{2} v \sqrt{g_W^2 + g_W'^2}, \tag{1.26}$$

where g_W and g'_W are the electroweak coupling strengths (see Section 1.3.3). Equations (1.25) and (1.26) are used with Equation (1.21) to obtain the ratio of boson masses in terms of the Weinberg angle:

$$\cos\theta_W = \frac{M_W}{M_Z}. \tag{1.27}$$

In addition, the Lagrangian also gains self-energy terms involving the new field [11]:

$$\mathcal{L}_H = \frac{1}{2}\partial_\mu H \partial^\mu H - \mu^2 H^2 - \lambda v H^3 - \frac{1}{4}\lambda H^4 \tag{1.28}$$

which implies the existence of an additional massive boson with a mass $\sqrt{2}\mu = \sqrt{2\lambda}v$, the Higgs boson.

To date there has been no observation of the Higgs boson. Limits of $M_H > 114$ GeV [21] and $158 < M_H < 175$ GeV [22, 23] have been set by LEP and the Tevatron, respectively. The observation of the Higgs boson is one of the major objectives of the physics programme at the Large Hadron Collider [24, 25].

Chapter 2

Tevatron and CDF

The Fermi National Accelerator Laboratory (FNAL), commonly known as Fermilab, is a research facility co-operated by the U.S Department of Energy and a collaboration of universities. Its stated mission is to advance "the understanding of the fundamental nature of matter and energy by providing leadership and resources for qualified researchers to conduct basic research at the frontiers of high energy physics and related disciplines" [26].

Located in the suburbs of Chicago, Fermilab is home to the Tevatron, formerly the world's highest energy particle collider. Operating at a centre-of-mass energy of 1.96 TeV, the Tevatron is a circular machine which collides 980 GeV protons with 980 GeV antiprotons every 396 ns for high energy physics studies over a number of hours.

2.1 Particle accelerator chain

The production, acceleration and distribution of protons and antiproton beams involves multiple linear accelerators and synchrotrons designed to maximise the energy and instantaneous luminosity of the colliding $p\bar{p}$ beams. Increased energy is desirable because it allows the production of more massive particles

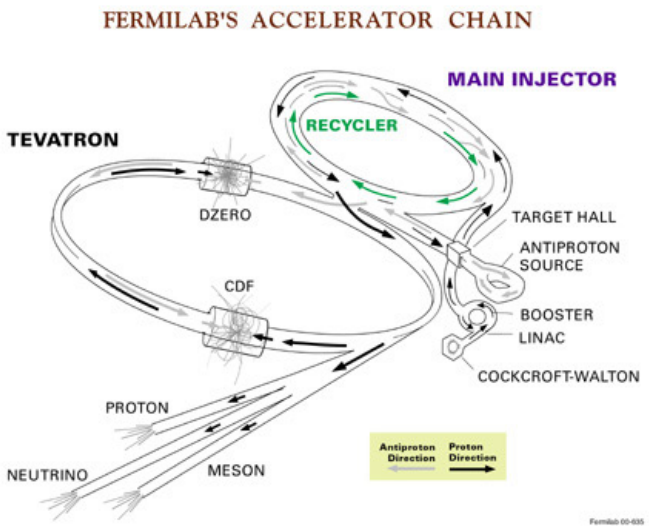

Figure 2.1: A schematic representation of the accelerator chain at Fermilab [27].

and greater luminosity, the number of particles passing through a unit area in unit time, is desired because it increases the number of interactions when the beams collide.

2.1.1 Proton source

The combined machines which produce the initial proton beam are the Pre-accelerator, the Linear Accelerator (Linac) and the Booster, collectively known as the "proton source".

Pre-accelerator

A magnetron produces hydrogen ions from hydrogen gas every 66 ms. An electric field strips the electrons off the protons and the resulting plasma is passed over caesium, where the protons pick up two electrons. The H^- beam is accelerated through a drift tube by a Cockcroft-Walton generator up to 0.75 MeV before it is sent toward the linear accelerator.

The linear accelerator

The linac is formed in two major sections. The first section consists of five cylindrical Alvarez drift chambers which accelerate the hydrogen ion beam from 0.75 MeV to 116 MeV. The second section consists of seven side-coupled cavity modules which accelerate the 116 MeV beam up to 400 MeV. The linac can operate in several different modes. Whenever the linac sends the hydrogen beam toward the Booster it is operating in its High Energy Physics mode. Alternatively, the linac can also provide particles for the cancer treatment facility on site [28].

Booster

The minimum energy the Main Injector accepts is 8 GeV which would require a linear accelerator many miles in length. This is not feasible so the Booster is an intermediate synchrotron which serves as the coupling between the linear accelerator and the Main Injector.

A further purpose of the Booster is to strip away the electrons from the H^- ions leaving a proton beam. The H^- bunches are passed through a thin carbon foil which removes the electrons. The machine is 150 m in diameter and consists of 19 radio-frequency cavities, taking 22 ms for a proton to complete one loop of the Booster.

2.1.2 Antiproton source

The production of antiprotons is one of the more time-intensive aspects of the accelerator chain. An 8 GeV beam of protons is diverted away from the Main Injector and directed towards a nickel fixed-target. The collision produces many secondary particles and the resulting antiprotons are extracted.

Debuncher and Accumulator

The beam of antiprotons is sent toward a pair of machines, the Debuncher and Accumulater, designed to collect and store the batches of antiprotons produced from the fixed target collisions. The main role of the Debuncher is to prepare the antiproton bunches for storage in the Accumulator by reducing the momentum of the antiprotons and the transverse size of the beam. The Accumulator, suggestively, accumulates antiprotons over a number of hours. Both machines are housed in the same tunnel.

Recycler

The Recycler is a storage ring for antiprotons located in the same tunnel as the Main Injector. It accepts antiprotons from the Accumulator via the Main Injector and cools them further. An 8 GeV beam of thermally cool electrons is passed over the hotter 8 GeV antiproton beam and glancing collisions between the beams transfers longitudinal momentum. This gives more compact antiproton bunches which allows for more luminous collisions. Unlike many of the machines, the Recycler does not accelerate particles and it mainly uses permanent magnets to direct the beams as opposed to electromagnets.

2.1.3 Main Injector

The Main Injector serves as a connecting machine between the proton source and a variety of different experimental apparatus. It has a circumference seven times larger than the Booster. The Main Injector is a replacement for the older Main Ring accelerator which, as the Main Ring was housed in the same tunnel as the Tevatron, was deemed to interfere too much with the Tevatron and degraded the quality of the colliding beams[1]. It accepts the 8 GeV proton

[1]Originally the Main Ring was the primary synchrotron at Fermilab with the Tevatron a more powerful addition in the same tunnel. The building of CDF and DØ required the

beam from the Booster and is capable of accelerating the protons up to different energies depending on the destination.

The Main Injector has a number of different modes of operation which relate to its need to provide 150 GeV protons for the Tevatron, 120 GeV protons for the NuMI apparatus [29], and to redirect antiprotons from the Accumulator to the nearby Recycler.

2.1.4 Tevatron

The Tevatron is the primary synchrotron at Fermilab and, with colliding beam energies of 980 GeV and a centre-of-mass collision energy of 1.96 TeV, held the title of the highest-energy particle collider in the world until the Large Hadron Collider began operating at higher energies. The Tevatron accepts 150 GeV protons and antiprotons from the Main Injector and accelerates the particle beams up to the collision energies of 980 GeV. Once the particle beams are accelerated the Tevatron is effectively a storage ring for the particles while they circle the machine. To avoid particle interactions when not desired, the proton and antiproton beams are held in different helical orbits.

The radius of the machine is one kilometre and the ring consists of six major sections named A to F. The beginning of each section is named A0 to F0. B0 and D0 serve as "interaction points" where the circling proton and antiproton beams are passed through one another. Each of these points is home to one of the two detectors at the Tevatron: the Collider Detector at Fermilab (CDF) at B0 and DØ at D0.

The fixed collection of protons and antiprotons that circle the Tevatron for the purpose of high energy physics studies is know as a "store." A store may

Main Ring to be redirected to avoid passing through their detection volume and this added to the problems with the Tevatron and Main Ring sharing a tunnel.

last for a number of hours while the rest of the accelerator complex delivers particles for the NuMI neutrino beam and produces antiprotons for future stores. Over the lifetime of the store the instantaneous luminosity of the colliding beams decreases and when the instantaneous luminosity gets too low for useful physics the store is ended.

A new store is prepared by moving proton bunches from the Main Injector to the Tevatron. The Main Injector accepts proton bunches from the Booster and coalesces them into a larger "super-bunch". A single proton super-bunch is injected at a time and is separated by 396 ns from the previous bunch. There are 36 bunches in total with larger abort gaps (2.617 μs) between a "train" of 12 bunches. Once the protons are orbiting within the Tevatron, the 36 bunches of antiprotons are extracted from the Recycler by the Main Injector and inserted into the Tevatron. The antiprotons bunches are also separated by 396 ns. The proton and antiproton beams are accelerated from 150 GeV to 980 GeV, and the beam size is squeezed to increase the luminosity of the collisions. Collimators are used to remove particles that have dispersed away from the centre of the beam in order to protect detection equipment from radiation damage.

The Tevatron has been performing well for a number of years, as can seen in Figure 2.2, and has provided CDF and DØ with $p\bar{p}$ collision data with more than 9 fb^{-1} of integrated luminosity at a 1.96 TeV centre-of-mass energy. The Tevatron is scheduled to run until October 2011 where it is hoped to have accumulated data with an integrated luminosity of 12 fb^{-1}.

2.2 The Collider Detector at Fermilab

The Collider Dectector at Femilab (CDF) [31, 32, 33] is one of the two general purpose particle detectors at Tevatron. It has a cylindrical design where a

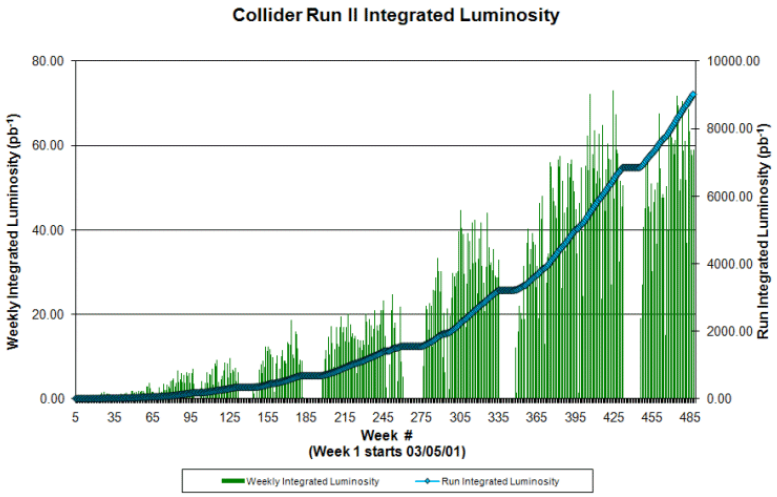

(a) Integrated luminosity

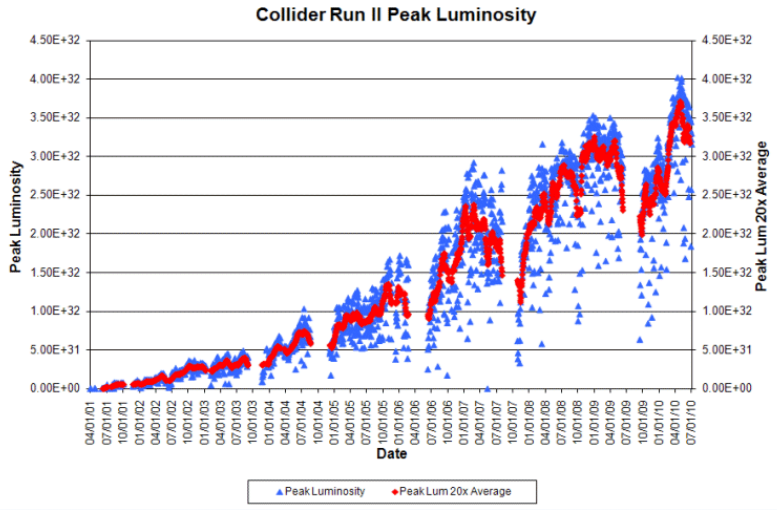

(b) Peak instantaneous luminosity

Figure 2.2: The performance of the Tevatron over the lifetime of Run II. (a) The integrated luminosity of the $p\bar{p}$ data provided to CDF and DØ for high energy physics studies and over 9 fb^{-1} has been delivered to date (Summer 2010). (b) The peak instantaneous luminosity of $p\bar{p}$ collisions which can be seen to have increased over time, showing an increased performance of the Tevatron in providing high luminosity physics collisions [30].

number of detection systems surround the beam pipe at an increasing radius in the "central" region with further systems in the flat end-caps known as the "plug". A cut-away of the detector is shown in Figure 2.4.

The design of CDF makes it natural to work in a cylindrical coordinate system where the positive z-axis is directed along the beam pipe and in the direction of the traveling protons. Figure 2.3 and Equation (2.1) to Equation (2.4) show the relationship between the radial axis, r, azimuth, ϕ, and Cartesian coordinates.

$$x = \rho \cos\phi \sin\theta = r \cos\phi \tag{2.1}$$

$$y = \rho \sin\phi \sin\theta = r \sin\phi \tag{2.2}$$

$$z = \rho \cos\theta \tag{2.3}$$

$$r = \rho \sin\theta. \tag{2.4}$$

The pseudorapidity serves as an alternative angular unit and is defined by Equation (2.5). Expressed using particle momentum, $\mathbf{p}$, pseudorapidity is comparable with rapidity, Equation (2.7), using a massless particle approximation[2].

$$\eta = -\ln\tan\frac{\theta}{2} \tag{2.5}$$

$$= \frac{1}{2}\ln\frac{|\mathbf{p}| - |\mathbf{p}_L|}{|\mathbf{p}| + |\mathbf{p}_L|} \tag{2.6}$$

$$y = \frac{1}{2}\ln\frac{E - |\mathbf{p}_L|}{E + |\mathbf{p}_L|}. \tag{2.7}$$

Differences between rapidities are unchanged by Lorentz boosts along the beam axis; therefore, pseudorapidity differences are unaffected. This makes pseudorapidity a more natural unit for describing particle collisions than θ. The

[2]For relativistic particles, the rest mass of the particle can be neglected and $P^2 = E^2 - |\mathbf{p}|^2c^2 = 0$. Throughout this analysis, P denotes a four-vector, E is the energy and $\mathbf{p}$ is the momentum vector with $p \equiv |\mathbf{p}|$. The convention $c = 1$ is used.

central region of CDF is symmetric in ϕ and extends to approximately 1 in $|\eta|$. The plug detectors cover $1 < |\eta| < 2.6$.

In the central region, the detector is optimised to measure properties in the plane transverse to the beam pipe. This is because many transverse properties are invariant with respect to Lorentz boosts along the z-axis. In addition, the hadronic decays of the spectator quarks are typically lost down the beam pipe which makes it impossible to impose the conservation of momentum in the z-axis as a kinematic constraint.

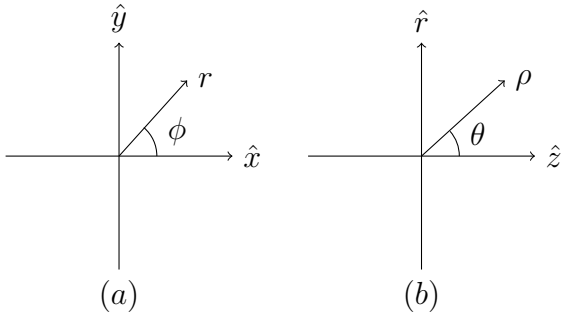

Figure 2.3: The coordinate system used at CDF. (a) The radial axis, r, and azimuth, ϕ are shown in the $x - y$ plane transverse to the beam pipe. The detector is designed to be ϕ-symmetric. (b) The pseudorapidity, $\eta = -\ln\tan(\theta/2)$, is defined in the $r - z$ plane.

2.2.1 Particle tracking

CDF has two main tracking systems: the silicon detectors and the gas drift chambers. The silicon detectors [34] are referred to as Layer 00 (L00), Silicon Vertex detector (SVXII) and Intermediate Silicon Layers (ISL), and are primarily looking for the decays of short-lived particles close to the beam pipe. The innermost silicon detector is Layer 00 which rests on the beam pipe and covers 1.35 cm to 1.62 cm in the radial direction. Located so close to the passing beam it needs to be radiation-tolerant, capable of withstanding 5–10 MRad [34]. The SVXII [35] consists of five double-sided layers of silicon in

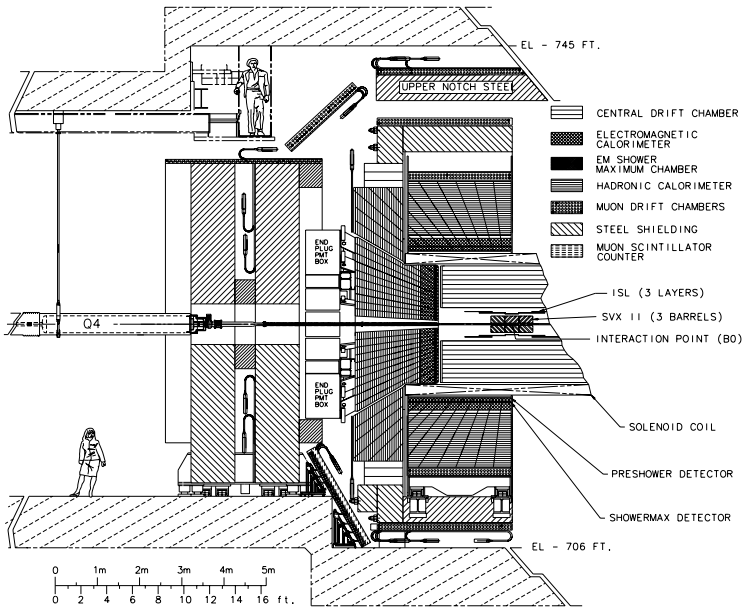

Figure 2.4: An elevation view of half of CDF showing the various detector subsystems [33].

three cylindrical barrels. Altogether, the SVXII detector covers a range from 2.5 cm to 10.6 cm in the radial direction. The final silicon tracking system, the ISL [36], spans from 19.7 cm to 29.0 cm in the radial direction.

The other main tracking system at CDF is the Central Outer Tracker (COT) [37]. It is a drift chamber, 300 cm in length along z, and covers the entire central region in $|\eta|$. It spans from 44 cm to 132 cm in the radial direction. The original design of the detector had an even mixture of argon and ethane but degradation of the chamber necessitated the introduction of small quantities of oxygen to slow down the accumulation of polymers on the surface of the wires [38, 39].

The COT contains 96 layers of sense wires that are grouped into eight concentric "superlayers" of twelve layers. Each superlayer has one of two orientations: "axial", where all the sense wires run parallel to the beam and give a good resolution in the $r - \phi$ plane; and "stereo", where the layers in a superlayer alternate between having a 2° inclination with respect to the beam

and a 2° declination. Stereo superlayers allow for reconstruction in the $r-z$ plane. The superlayers alternate between the axial and stereo configurations and the combination allows for a 3D reconstruction of a charged particle's path through the chamber.

Surrounding the COT at a radius of 1.5 m is a solenoid that is 4.8 m in length [33]. The 1.4 T magnetic field it provides aids with particle identification. Charged particle and antiparticles are distinguished from one other by the direction of the Lorentz force and the reconstructed paths are used to estimate their momenta transverse to the beam pipe:

$$p_T = \frac{eB}{2|C|} = \frac{eB}{2}\frac{2R}{|q|} \tag{2.8}$$

where e is the charge of an electron, B is the magnetic field strength, and $C \equiv q/(2R)$ is the curvature for a particle with charge q and radius R. The value of $eB/2$ at CDF is 2.11593×10^3 GeV/cm [40]. The momentum resolution of the tracking systems is $\Delta p_T/p_T^2 = 0.15\%$ for COT tracking only, and $\Delta p_T/p_T^2 = 0.07\%$ when using the COT, SVX and ISL.

2.2.2 Calorimetry

The calorimetry systems at CDF measure the energies of particles produced by the collision between the proton and antiproton beams. In the central region, $|\eta| < 1$, there is an electromagnetic calorimeter (CEM) which primarily records the energy deposition of photons and electrons. Behind the electromagnetic calorimeter there is the hadronic calorimeter (CHA) which records the more deeply penetrating hadrons. Muons leave only a minimal deposition in both the electromagnetic and hadronic calorimeters and neutrinos escape undetected. In the plug there is also an electromagnetic calorimeter (PEM) in front of a hadronic calorimeter (PHA) covering the forward range in $|\eta|$.

Central electromagnetic calorimeter

The central electromagnetic calorimeter [41] is a lead-scintillator sampling calorimeter comprised of a modular "tower" geometry pointing toward the interaction point. Each calorimeter tower is 0.1 units in $|\eta|$ by 15° in ϕ. Ten adjacent η-towers form one ϕ-wedge, and twenty-four wedges form one half of the CEM detector. Where the halves meet a $\eta = 0$ there is no CEM coverage and it is known as the "central gap".

Each CEM tower contains thirty-one 5 mm polystyrene scintillator layers interwoven with thirty layers of aluminium clad lead. The lead is 4.23 mm thick with 0.38 mm of aluminium on both sides. When electrons or photons enter the calorimeter they scatter off the metal nuclei producing more electrons and photons leading to an avalanche of particles known as a "shower". Photomultiplier tubes, connected to the scintillators by waveguides, convert the light into a signal. The energy resolution of the CEM was studied using test beam data [41] and is:

$$\frac{\Delta E}{E} = \frac{13.5\%}{\sqrt{E_T}} \oplus \kappa_{\mathrm{CEM}} \tag{2.9}$$

where $E_T \equiv E \sin\theta$ is the energy of the electromagnetic shower in the $r - \phi$ plane transverse to the beam pipe, κ_{CEM} is the effect of additional energy resolution that does not follow a $1/\sqrt{E_T}$ relationship and is obtained from data separately. The $\oplus$ represents an addition in quadrature. The κ_{CEM} term is typically of the order of 1–2%.

Between the eight and ninth lead-scintillator layers are proportional strip chambers, the central electromagnetic strip chambers (CES). The CES is located at this depth in the tower as this corresponds to the expected maximum transverse profile. Anode wires in the plane transverse to the beam pipe and

cathode strips along the z-axis collect charge proportional to the energy of the showering particle. Particles showering in the CEM have different transverse profiles and this aids in particle identification. The location of a shower in the CES is defined by the global z-axis parallel to the beam pipe, and by the local x-axis of the CES module which is transverse to the beam. In CES coordinates, the central gap is defined by $|z_{\rm CES}| < 4.2$ cm, and $|x_{\rm CES}| > 23.1$ cm defines the region of a ϕ-wedge where the response of the modules is degraded due to gaps between adjacent modules in ϕ.

The lateral shower profile can also be used in particle identification. The $L_{\rm shr}$ variable, Equation (2.10), is used to compare how the observed energies for the adjacent towers in η, $E_i^{\rm adj}$, compare with the expected energies, $E_i^{\rm exp}$, from test beam data [42]:

$$L_{\rm shr} = 0.14 \sum_i \frac{E_i^{\rm adj} - E_i^{\rm exp}}{\sqrt{0.14^2 E_i^{\rm adj} + (\Delta E_i^{\rm exp})^2}}. \tag{2.10}$$

A small $L_{\rm shr}$ is the result of less leaking of the electromagnetic shower energy in the lateral direction. Showers with small lateral profiles are identified as electrons.

Central hadronic calorimeter

The central hadronic calorimeter (CHA) [43] has a modular design similar to the CEM with a projective geometry pointing toward the interaction point and towers segmented by 0.1 units in η and 15° in ϕ. Each tower is comprised of layers of 2.5 cm steel and 1 cm of a doped acrylic scintillator.

The energy resolution of the CHA is obtained from test beam studies [43] and is:

$$\frac{\Delta E}{E} = \frac{50\%}{\sqrt{E_T}} \oplus \kappa_{\rm CHA} \tag{2.11}$$

where $E_T \equiv E \sin\theta$ is the energy of the hadronic shower in the $r - \phi$ plane transverse to the beam pipe.

2.2.3 Muon chambers

Muons deposit minimal energy as they pass through CDF because of their mass and the consequent reduced likelihood of bremsstrahlung. Hence, there are specific drift chambers beyond the calorimetry systems designed to track and identify muons. Coverage of muons in the central region is provided by three separate detectors: the central muon detector (CMU), the central muon upgrade (CMP), and the central muon extension (CMX). The CMU [44] and CMP [45] cover the range $|\eta| \leq 0.6$. The rest of the coverage in the central region is provided by the CMX, $0.6 \leq |\eta| \leq 1.0$ [45].

The CMU is attached to the outer ring of the central hadronic calorimeter at a radius of 347 cm. It is partitioned into 15° wedges in ϕ but the active detection range is only 12.6° leaving a small gap between wedges. To reduce the residual pion signal, the CMP is placed behind steel sheets in a box around the detector. The different geometry of the CMP gives it a smaller surface area in the $\eta - \phi$ plane compared with the CMU (see Figure 2.5). A muon track reconstructed in both the CMU and CMP is known as a CMUP "stub". The drift times for the CMU and CMP are 800 ns and 1800 ns which is longer than two bunch crossings; therefore, it is important for the muon stub to be matched with the correct COT track so that the original $p\bar{p}$ interaction is identified.

The CMX is a combination of conical arches covering 270° in ϕ and flat chambers where the conical arches would otherwise pass through the floor ("miniskirt"). It has its own scintillator (CSX) to allow for the fast timing information to reject muon stubs from events that do not coincide with a recent $p\bar{p}$ collision.

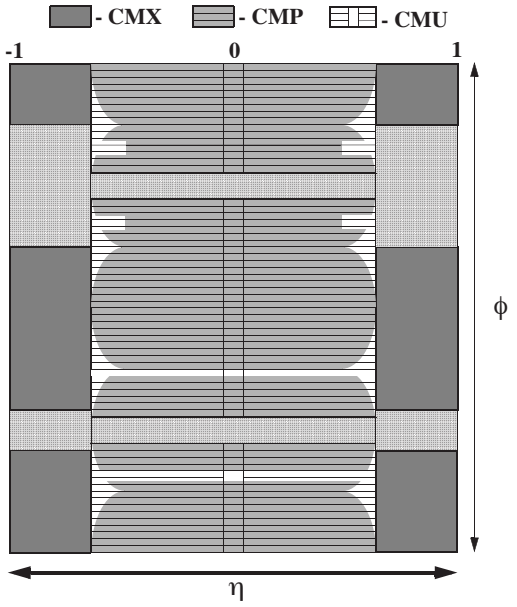

Figure 2.5: The coverage of the muon chambers in the $\eta - \phi$ plane [32].

2.2.4 Trigger

The Tevatron collides a proton bunch with an antiproton bunch every 396 ns which is far too frequent in order to extract and store all the events that could occur. Furthermore, not every event is of interest; therefore, it is essential to have a way of quickly identifying interesting interactions. This gives rise to the three stage trigger system at CDF shown in Figure 2.6.

The most primitive stage, level 1, is a hardware based trigger using fast algorithms to decide whether the basic tracking and calorimetric signals demand further processing. While the level 1 trigger is making its decision some extra information needed for level 2, such as silicon track information, is read out and placed into one of four buffers. With a beam crossing every 396 ns this corresponds to a readout rate of 2.5 MHz.

If a level 2 decision is required the buffered information collected while level 1 was running is used to make a more advanced decision: the silicon tracking

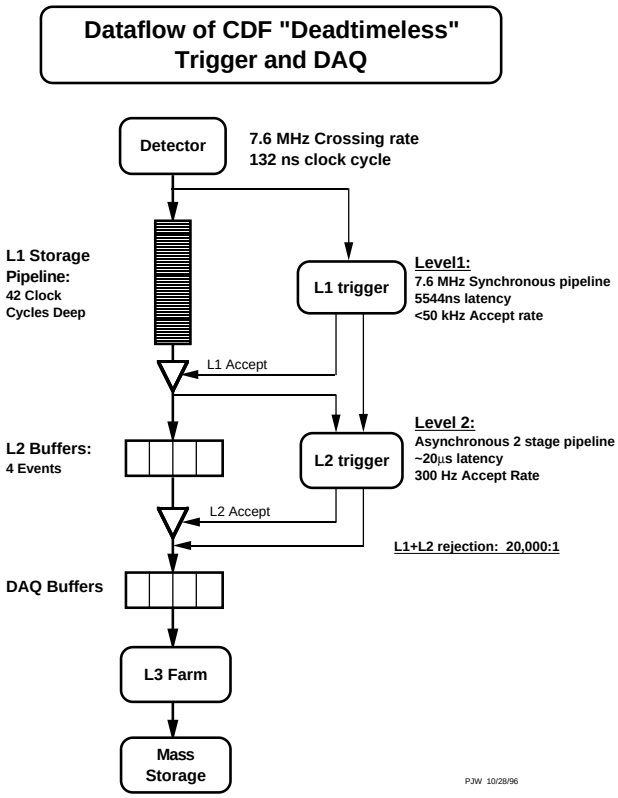

Figure 2.6: An overview of the three level trigger used by CDF [46].

trigger forms secondary vertices, the CES provides showering information for electron and photon identification, and the subsystems used to form a level 1 decision run more sophisticated algorithms.

Should level 2 accept the event then the full software reconstruction of the event is carried out on an external computer farm and the level 3 trigger decides whether to record the event to tape.

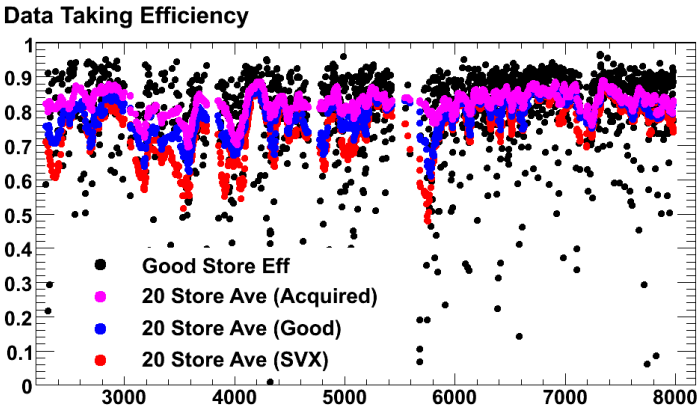

Figure 2.7: The performance of the CDF detector over the lifetime of Run II. The data taking efficiency is presented as a function of store number [47].

2.2.5 Performance

The plots in Figure 2.7 show the performance of CDF over the Run-II data taking period to date. The data taking efficiency of CDF is relatively stable over the Run-II period at approximately 80%.

Chapter 3

W mass measurement

In Section 1.3.4 the importance of the Higgs boson was introduced and the mass of the W boson is related to the vacuum expectation value of the Higgs field at leading order, Equation (1.25).

3.1 Importance and role in electroweak fits

The influence of the Higgs boson on the mass of the W can be seen through its role in higher order diagrams. The radiative corrections can be related to the masses of the weak bosons in the standard model by the following [11]:

$$1 - \frac{M_W^2}{M_Z^2} = \frac{1}{2}\left[1 - \left(1 - \frac{4\pi\alpha}{\sqrt{2}G_F M_W^2\,(1-\Delta r)}\right)^{\frac{1}{2}}\right] \tag{3.1}$$

where G_F is the Fermi coupling constant, α is the electromagnetic coupling constant, and Δr are the radiative corrections. The one loop radiative corrections have been calculated [48] to give:

$$\Delta r \approx \frac{\alpha}{\alpha(M_Z^2)} + \frac{G_F}{8\sqrt{2}\pi^2}\left(-3\cot^2\theta_W M_t + \frac{11}{3}M_W^2 \ln\frac{M_H^2}{M_W^2}\right) \tag{3.2}$$

where θ_W is the Weinberg angle, $\alpha(M_Z^2)$ is the electromagnetic coupling constant evaluated at the scale of the Z^0 mass. M_t, M_W and M_H are the masses of the top quark, W boson and Higgs boson, respectively.

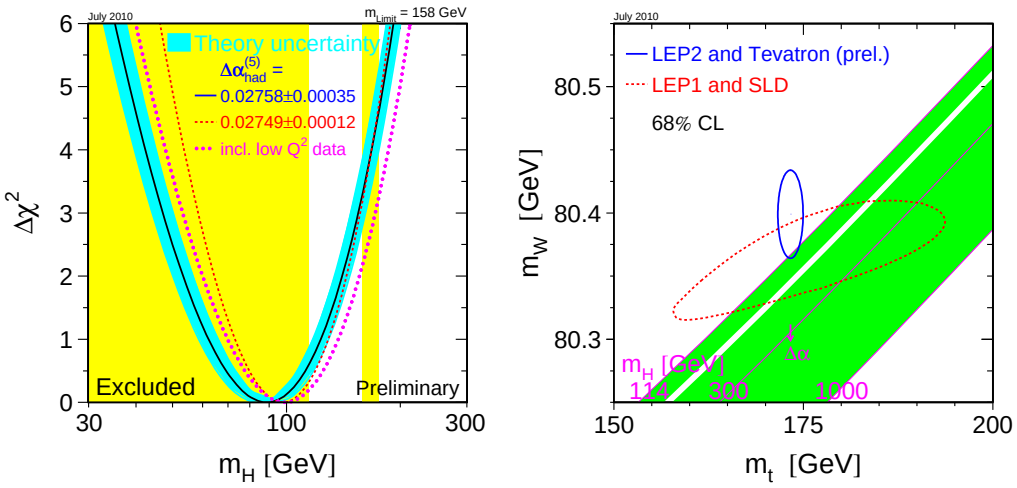

(a) (b)

Figure 3.1: The standard model Higgs prediction from the recent LEP and Tevatron Electroweak Working group results [49, 50]. (a) The "blue band" plot showing the best fit value for the Higgs mass obtained using ZFITTER [51] with the LEP low-mass and Tevatron high-mass direct exclusions shown as shaded regions. (b) The constraint on a standard model Higgs boson from electroweak measurements. The contours show the 68% confidence intervals for direct (LEP2 and Tevatron) and indirect (LEP1 and SLD) measurements of the W and top quark masses. The diagonal stripe is the corresponding Higgs mass prediction. Unshaded regions of the plot are where a standard model Higgs has been excluded.

The implication of Equation (3.2) is that the mass of the Higgs boson and the mass of the W have a logarithmic relationship. Precision measurements of the top quark and W can be used to constrain the standard model prediction, Figure 3.1 [50]. In Figure 3.1(a), the best fit value for the Higgs mass within the standard model is presented with the LEP low-mass and Tevatron high-mass direct exclusion regions. The 68% confidence interval contours of the top mass and W mass measurements are shown with compatible standard model Higgs masses in Figure 3.1(b). The constraint on the top and W masses from direct measurements of the particles at LEP2 and the Tevatron form one contour, and the indirect constraints from LEP1 and SLD results form the other.

Figure 3.2 shows how the electroweak fit predictions for the Higgs mass

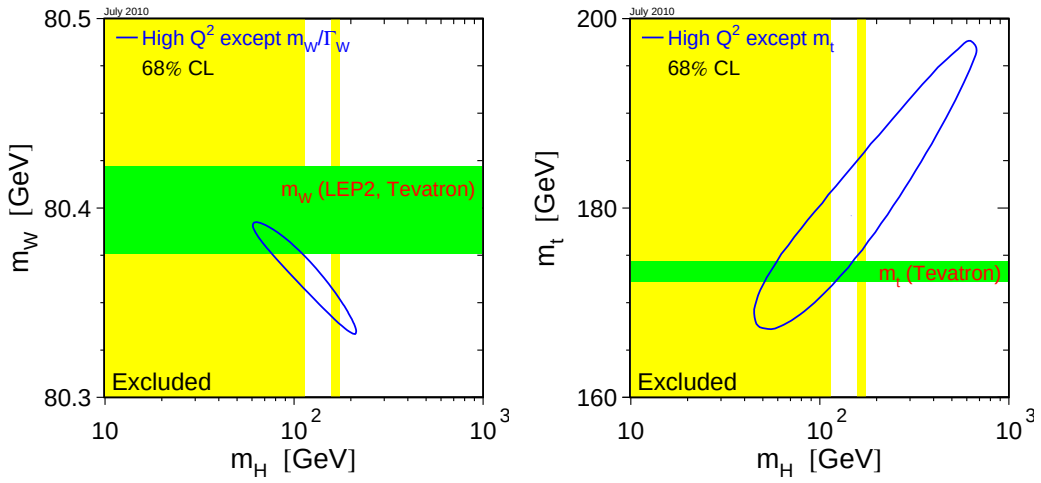

(a) (b)

Figure 3.2: The standard model Higgs prediction contours from the recent LEP Electroweak Working group results [49, 50]. (a) The contour is the 68% confidence interval excluding W mass data, where the horizontal shaded area represents direct measurements of M_W and one standard deviation error. (b) The contour is the 68% confidence interval excluding top mass data, where the horizontal shaded area represents direct measurements of M_t and one standard deviation error. Vertical shaded regions of the plot are where a standard model Higgs has been excluded.

vary with respect to the W boson and top quark masses. The contours indicate that reducing the uncertainty in M_W would have a greater impact on the Higgs mass than would be obtained by a top mass constraint; therefore, significantly reducing the W boson mass uncertainty will have important implications. In particular, Figure 3.2(a) suggests that a more massive M_W corresponds to a lighter Higgs boson within the standard model. The standard model prediction of M_W is 80379 MeV [50], and the current world average is 80399 ± 23 MeV [4]. If the uncertainty is reduced while the central value remains unchanged or migrates higher then it may move the electroweak fit prediction of the Higgs boson mass toward the region excluded by direct searches at LEP [52]. This provides ample motivation to reduce M_W uncertainty.

3.2 W fit variables

The W mass must be measured from the experimental observable properties associated with the decay products of the boson. Decays into hadrons are difficult to resolve from background processes at a proton-antiproton collider; therefore, the leptonic decay products, a charged lepton and neutrino, are used. One such observable is the transverse momentum of the charged lepton.

Consider a proton with four-momentum P_p colliding with an antiproton with four-momentum $P_{\bar{p}}$ as depicted in Figure 3.3. At the Tevatron the proton and antiprotons are traveling at 980 GeV and are highly relativistic ; hence, the squared centre-of-mass energy of the proton-antiproton system is

$$s = \left(P_p + P_{\bar{p}}\right)^2 \approx 2P_p \cdot P_{\bar{p}}; \tag{3.3}$$

hence, for a head-on collision with $E_p = E_{\bar{p}} = 980$ GeV and $\mathbf{p}_p = -\mathbf{p}_{\bar{p}}$, the centre-of-mass energy is

$$s \approx 2P_p \cdot P_{\bar{p}} = 2\left(E_p E_{\bar{p}} + |\mathbf{p}_p||\mathbf{p}_{\bar{p}}|\right) = (1960)^2 \text{ GeV}^2. \tag{3.4}$$

The simplest interaction producing a W involves a quark from the proton annihilating with an antiquark from the antiproton. The proton emits a quark which carries x_1 of the total momentum and the antiproton emits an antiquark with x_2 of the total momentum. The squared centre-of-mass energy for the quark-antiquark system, $\hat{s}$, is given by

$$\hat{s} = (x_1 P_p + x_2 P_{\bar{p}})^2 \approx 2x_1 x_2 P_p \cdot P_{\bar{p}} \quad , \tag{3.5}$$

and it is evident that $\hat{s} = x_1 x_2 s$ by comparing Equation (3.3) and Equation (3.5).

The colliding quark and antiquark with a centre-of-mass energy, $\sqrt{\hat{s}}$, produce a W which decays into a charged lepton and associated neutrino. The

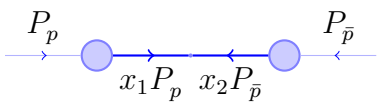

Figure 3.3: The centre-of-mass energy system for a quark and antiquark emitted from a head-on collision between parallel proton and antiproton beams. There is no net transverse momentum in the quark-antiquark system.

energy is shared equally between each particle in the centre-of-mass system. The neutrino is not measured by CDF which makes reconstructing the four-vector of the W difficult. In the central region, CDF is optimised to measure properties in the $r-\phi$ plane transverse to the beam pipe, and the transverse energy and momentum of the lepton in the centre-of-mass frame can be defined as:

$$E_T^l \equiv \frac{\sqrt{\hat{s}}}{2}\sin\theta \text{ and } p_T^l \approx \frac{\sqrt{\hat{s}}}{2}\sin\theta \tag{3.6}$$

where θ is the polar angle in the $r-z$ plane measured from the positive z-axis (proton direction), and from Equation (3.6) it is evident that:

$$\sin\theta = \frac{2E_T^l}{\sqrt{\hat{s}}} \text{ and } \cos\theta = \sqrt{1-\frac{4E_T^2}{\hat{s}}} \quad . \tag{3.7}$$

The transverse properties of the neutrino can be inferred by energy and momentum conservation and transverse properties have the additional benefit of being unaffected by longitudinal Lorentz boosts.

To first order, a lepton of charge q that results from the decay of a W boson follows a characteristic angular distribution (the angular distribution is discussed in more detail in Section 5.4.2):

$$\frac{d\sigma}{d(\cos\theta)} \propto 1 - q\cos^2\theta \quad . \tag{3.8}$$

Which can be rewritten in terms of E_T^l:

$$\frac{d\sigma}{dE_T^l} = \frac{d(\sin\theta)}{dE_T^l} \cdot \frac{d(\cos\theta)}{d(\sin\theta)} \cdot \frac{d\sigma}{d(\cos\theta)} \quad . \tag{3.9}$$

Substituting Equation (3.7) into Equation (3.9) and the transverse energy distribution of charged leptons is:

$$\frac{d\sigma}{dE_T^l} \propto \frac{4E_T^l}{\hat{s}} \frac{2 - \frac{4(E_T^l)^2}{\hat{s}}}{\sqrt{1 - \frac{4(E_T^l)^2}{\hat{s}}}} \tag{3.10}$$

which is singular when E_T^l is $\sqrt{\hat{s}}/2$. This result adds a characteristic feature to transverse energy distributions known as the Jacobian edge, where the distribution rises sharply as the transverse energy of the charged lepton approaches the cut off and falls sharply beyond it.

The singularity in this distribution is made finite by replacing a fixed centre-of-mass energy, $\hat{s}$, with a Breit-Wigner distribution, $\hat{s}\,(M_W, \Gamma_W)$, which depends on the mass of the W boson, M_W, and the width, Γ_W:

$$\frac{d\sigma}{d\hat{s}} \propto \frac{1}{\left(\hat{s} - M_W^2\right)^2 + \Gamma_W^2 M_W^2}. \tag{3.11}$$

The E_T distribution remains peaked at $\sqrt{\hat{s}}/2$ but now with a sharply falling tail. The sensitivity of the Jacobian edge to the mass of the W boson, via $\hat{s}\,(M_W, \Gamma_W)$, makes the transverse energy one possible kinematic distribution from which M_W can be measured.

Up to this point it has been assumed that the quark and antiquark collide head on and the intrinsic transverse momentum of the W boson has been neglected. Prior to the collision, one or both of the quarks that produce the W may emit gluons which carry off a fraction of the quark's momentum. The colliding quarks now have some net momentum in the transverse plane as a result of gluon radiation which is propagated into the W and resulting leptons. An example is depicted in Figure 3.4.

Consider the charged lepton in the centre-of-mass frame of the W boson with transverse energy, $|E_T^l|_{\text{com}}$, and transverse momentum, $|\mathbf{p}_T^l|_{\text{com}}$; the lepton

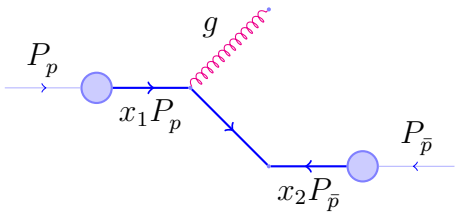

Figure 3.4: The centre-of-mass energy system for a quark and antiquark emitted from a head-on collision between parallel proton and antiproton beams with initial state gluon emission. The gluon emitted prior to the quark-antiquark interaction imparts some net transverse momentum on the quark-antiquark system.

is highly relativistic hence $|E_T^l|_{\rm com} = |\mathbf{p}_T^l|_{\rm com}$. The net transverse momentum of the colliding quarks imparts a transverse momentum, $\mathbf{p}_T^W$, on the W with a transverse energy, E_T^W. The kinematics of the lepton in the lab frame are related to those in the centre-of-mass frame by:

$$\begin{pmatrix} E_T^l \\ |\mathbf{p}_T^l| \end{pmatrix}_{\rm lab} = \begin{pmatrix} \gamma & \gamma\beta_T \\ \gamma\beta_T & \gamma \end{pmatrix} \begin{pmatrix} E_T^l \\ |\mathbf{p}_T^l| \end{pmatrix}_{\rm com} \tag{3.12}$$

where $\beta_T = |\mathbf{p}_T^W|/E_T^W$ and $\gamma = (1-\beta_T^2)^{1/2}$. From Equation (3.12) the properties of the lepton in the W centre-of-mass frame can be defined in terms of the observed energy and momentum in the detector:

$$|E_T^l|_{\rm lab} = \gamma|E_T^l|_{\rm com} + \gamma\beta_T|\mathbf{p}_T^l|_{\rm com} \tag{3.13}$$

$$|\mathbf{p}_T^l|_{\rm lab} = \gamma|\mathbf{p}_T^l|_{\rm com} + \gamma\beta_T|E_T^l|_{\rm com}. \tag{3.14}$$

Expanding γ to first order in β_T and substituting into Equation (3.14) gives, to first order ($\gamma \approx 1 + \frac{\beta_T^2}{2}$):

$$|E_T^l|_{\rm lab} \approx |\mathbf{p}_T^l|_{\rm com} + \beta_T|E_T^l|_{\rm com} + \frac{\beta_T^2}{2}|\mathbf{p}_T^l|_{\rm com} + \cdots \tag{3.15}$$

$$\approx |\mathbf{p}_T^l|_{\rm com} + |E_T^l|_{\rm lab}\frac{|\mathbf{p}_T^W|}{E_T^W}. \tag{3.16}$$

Recalling that the most probable configuration of energies is $E_T^l = E_T^\nu$ which implies that $E_T^W = E_T^l + E_T^\nu = 2E_T^l$; therefore,

$$|E_T^l|_{\rm lab} \approx |E_T^l|_{\rm com} + \frac{|\mathbf{p}_T^W|}{2}. \tag{3.17}$$

The transverse energy of the charged lepton as measured in the lab frame has a first order dependence upon the transverse momentum of the W. $\mathbf{p}_T^W$ is defined as $\mathbf{p}_T^l + \mathbf{p}_T^\nu$ but $\mathbf{p}_T^\nu$ is not measured directly. As such, $\mathbf{p}_T^W$ is not measured experimentally with particular accuracy which manifests itself as a uncertainty on M_W. The steps from Equation (3.12) to Equation (3.17) can be repeated for the neutrino energy and momentum and recalling that $|\mathbf{p}_T^l|_{\text{com}} = -|\mathbf{p}_T^\nu|_{\text{com}}$ by conservation of momentum:

$$|E_T^\nu|_{\text{lab}} \approx -|E_T^l|_{\text{com}} + \frac{|\mathbf{p}_T^W|}{2}. \tag{3.18}$$

Another experimental variable that can be used to measure M_W is the transverse mass of the W boson. It is defined in the lab frame as:

$$(M_T^W)^2 = \left(|E_T^l|_{\text{lab}} + |E_T^\nu|_{\text{lab}}\right)^2 - \left(|\mathbf{p}_T^l|_{\text{lab}} + |\mathbf{p}_T^\nu|_{\text{lab}}\right)^2 \tag{3.19}$$

where E_T^l and E_T^ν are the transverse energies of the charged lepton and neutrino, and $\mathbf{p}_T^l$ and $\mathbf{p}_T^\nu$ are the transverse momenta of the charged lepton and neutrino. This can be rewritten in terms of the transverse momenta and angle of separation between the charged lepton and neutrino in the $r-\phi$ plane, $\Delta\phi$:

$$M_T = \sqrt{2|\mathbf{p}_T^l|_{\text{lab}}|\mathbf{p}_T^\nu|_{\text{lab}}\left(1-\cos\Delta\phi\right)} \tag{3.20}$$

where the relativistic approximation $E_T^l = |\mathbf{p}_T^l|$ is made.

Substituting Equations (3.17) and (3.18), which both contain terms to first order in $|\mathbf{p}_T^W|/|E_T^l|_{\text{com}}$, into Equation (3.20) and neglecting any second order terms in $|\mathbf{p}_T^W|/|E_T^l|_{\text{com}}$ yields

$$M_T = \sqrt{2|E_T^l|_{\text{com}}|E_T^\nu|_{\text{com}}\left(1-\cos\Delta\phi\right)} \tag{3.21}$$

which is equivalent to Equation (3.20); therefore, the transverse mass of the W is not sensitive to the transverse momentum to first order which is not

the case for the transverse energy of the lepton. This can be observed in Figure 3.5 where the charged lepton transverse momentum and W transverse mass are shown with and without the influence of W transverse momentum. It is for this reason that the primary fit variable used to estimate the W mass is the transverse mass of the W, M_T^W. The transverse energies of the charged lepton and neutrino can be used to fit for M_W but suffer from larger systematic uncertainties, such as a greater dependence on the determination of $\mathbf{p}_T^W$, and are used to cross check the M_T^W fit.

As previously mentioned, the neutrino escapes detection which hampers efforts to measure $\mathbf{p}_T^W$; however, the transverse energy of the neutrino can be inferred by balancing the total energy measured in the calorimeter against the energy of the charged lepton. This hadronic recoil, $\mathbf{U}$, is a vector in the $r-\phi$ plane and is comprised of the hadronic decay products of the spectator quarks, the decay products of the initial state and final state radiation, and the decay products of any multiple interactions. The recoil vector is calculated by a vector sum over all the calorimeter towers in the central region excluding any towers associated with the charged lepton. The total transverse momentum must be conserved, $\mathbf{U} + \mathbf{p}_T^l + \mathbf{p}_T^\nu = 0$, which implies:

$$\not\!\!E_T \equiv |\mathbf{p}_T^\nu| = -|\mathbf{U} + \mathbf{p}_T^l| \tag{3.22}$$

where an alternative definition of the neutrino energy, assumed to be the missing transverse energy, $\not\!\!E_T$, has been introduced.

The most likely M_W is measured by performing a template fit of weighted Monte Carlo events to data in the transverse mass of the W boson, M_T^W, the transverse momentum of the lepton produced in the decay of the W, E_T^l, and the missing transverse energy, $\not\!\!E_T$. As has been shown, all of these distributions have a Jacobian edge where the Briet-Wigner distribution controls the

singularity with the values of M_W and Γ_W affecting the falling tail of the distributions. A range of possible M_W are tested against data by re-weighing Monte Carlo events. For each M_W value in the fit, the Monte Carlo events are re-weighted to be consistent with the Breit-Wigner distribution for that particular mass. This produces a number of Monte Carlo template distributions that correspond to different values of M_W but are otherwise the same. Each template distribution is compared with data to obtain a χ^2. The range of χ^2 values is used to find the most likely M_W.

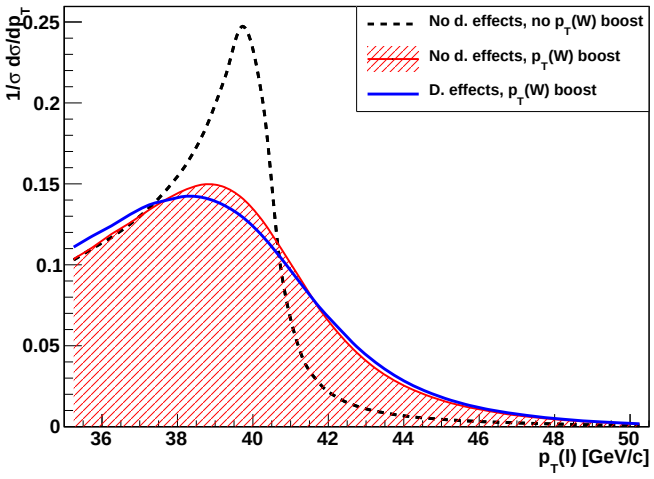

(a) Charged lepton transverse energy

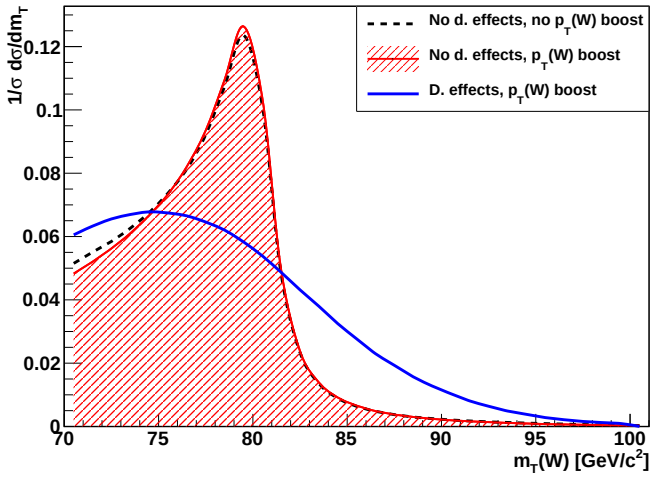

(b) W transverse mass

Figure 3.5: The effect of the W transverse momentum, $|\mathbf{p}_T^W|$, on the Jacobian edge for (a) the charged lepton transverse energy and (b) the transverse mass of the W. The dotted line is the variable in the lab frame before simulating detector resolution or acceptance for $|\mathbf{p}_T^W| = 0$. The shaded area is the variable in the lab frame before simulating detector resolution or acceptance for $|\mathbf{p}_T^W| \neq 0$. The solid line is the variable in the lab frame after simulating detector resolution and acceptance for $|\mathbf{p}_T^W| \neq 0$.

Chapter 4

Event selection

This analysis uses data collected at CDF from Feburary 4, 2002 to August 4, 2007. After removing data periods where the detector's data quality was deemed unacceptable, the total integrated luminosity of the dataset is 2.3 fb^{-1}. 640913 candidate $\text{W} \rightarrow e\nu$ and 657193 candidate $\text{W} \rightarrow \mu\nu$ events are selected according to the W, electron and muon criteria. 22487 candidate $\text{Z}^0 \rightarrow e^+e^-$ and 47176 candidate $\text{Z}^0 \rightarrow \mu^+\mu^-$ events are selected according to the Z^0, electron and muon criteria.

Particle and event identification uses several reconstructed kinematic variables and experimental signatures. The barrel design of CDF is optimised for the measurement of transverse properties in the $r - \phi$ plane transverse to the beam pipe.

4.1 Lepton selection criteria

The lepton selection for both electrons and muons is described in the following section and is summarised in Table 4.1. In many cases the large number of expected leptonic candidates allows for stringent kinematic constraints around the expected values to improve the purity of the sample despite the reduction in sample size.

Transverse momentum

The momentum of charged leptons in the transverse plane, p_T^l, is calculated from the reconstructed track curvature in a magnetic field, Equation (2.8). In the absence of detector smearing and resolution effects, the most probable energies of leptons produced from W and Z^0 decays are 40 GeV and 45 GeV. This is smeared out by resolution effects and longitudinal boosts which can lead to lower measured values so a lower bound of 30 GeV is set. An upper limit of 65 GeV is to reduce the contribution of hadronic decays containing high transverse momentum leptons.

Event vertex

The primary interaction vertex, z_0, is required to be within 60 cm of the centre of the detector. Studies at CDF using minimum bias data estimate that this accepts 95.8% of events [53].

Tracking superlayer hits

In order to pass the COT tracking cut and to ensure a higher quality sample, a reconstructed COT track must leave a minimum of 5 hits each on at least 4 axial and 4 stereo superlayers.

4.1.1 Electrons

In addition to the criteria outlined in Section 4.1, the following also apply for a candidate lepton to be classified as an electron. Figure 4.1 shows several cut variables prior to any selection for electron candidates.

Track transverse momentum

The transverse momentum, Equation (2.8), of the electron candidate must be greater then 18 GeV to satisfy the cut imposed by the level 3 trigger.

Calorimeter energy ratio

Electrons are not expected to penetrate much further than the CEM; however, some small leakage of energy from the electromagnetic to hadronic calorimeters is expected. A cut is made on the fraction of energies deposited in the hadronic calorimeter (E_{HAD}) and electromagnetic calorimeter (E_{EM}) where $E_{\mathrm{HAD}}/E_{\mathrm{EM}}$ must be less then 0.1 for an electron.

Energy-momentum ratio

The ratio of electron energy and momentum, E/p, should be one ignoring detector resolution effects and in-flight energy loss. Bremsstrahlung, ionisation and photon conversion can reduce the measured track momentum more so than the energy deposited in the CEM, giving E/p a long tail above one. The leakage of energy into adjacent towers and CEM resolution can lead to a lower energy being reconstructed for an electron of a given momentum, leading to a tail below one. Electrons are required to have E/p less than 1.6.

Lateral shower shape

Some electron energy may escape into adjacent calorimeter towers. L_{shr}, the lateral shower profile, Equation (2.10), is used to compute the difference between the observed energies in η-adjacent towers and the energies expected from test beam data [42]. L_{shr} must be less than 0.3 to be consistent with an electron shower.

COT CES gap

Candidate electrons are required to have no more than 5 cm separating the extrapolated COT track from the CES cluster in the $r-\phi$ plane, $|\Delta z|$.

Cluster location

The electron shower must be reconstructed within a well instrumented volume of the CES. A constraint on the local z-cordinate ($12 < |z_{\mathrm{CES}}| < 230$ cm) avoids the gap between the two halves of the CEM, and a constraint on the local x-coordinate ($|x_{\mathrm{CES}}| < 18$ cm) avoids regions where there is likely to be more leakage between gaps in the electromagnetic and hadronic calorimeters (see Section 2.2.2).

4.1.2 Muons

In addition to the criteria outlined in Section 4.1, the following also apply for a candidate lepton to be classified as a muon.

Calorimeter energy

Muons penetrate the calorimeter and do not leave a large energy deposit in either the electromagnetic or hadronic calorimeters. Candidate leptons are required to leave less than 2 GeV in the electromagnetic calorimeter (E_{EM}) and less than 6 GeV in the hadronic calorimeter (E_{HAD}) to be reconstructed as a muon.

Decay-in-flight muons

To remove muons originating from hadronic decays away from the interaction point, a cut on the quality of the track fit to COT hits is made ($\chi^2/\mathrm{dof} < 3$). In addition, a cut on the track impact parameter, the closest point on a track to the interaction point in the transverse plane, is made to remove a fraction of muon decays not associated with the primary interaction ($|d_0| < 0.1$ cm).

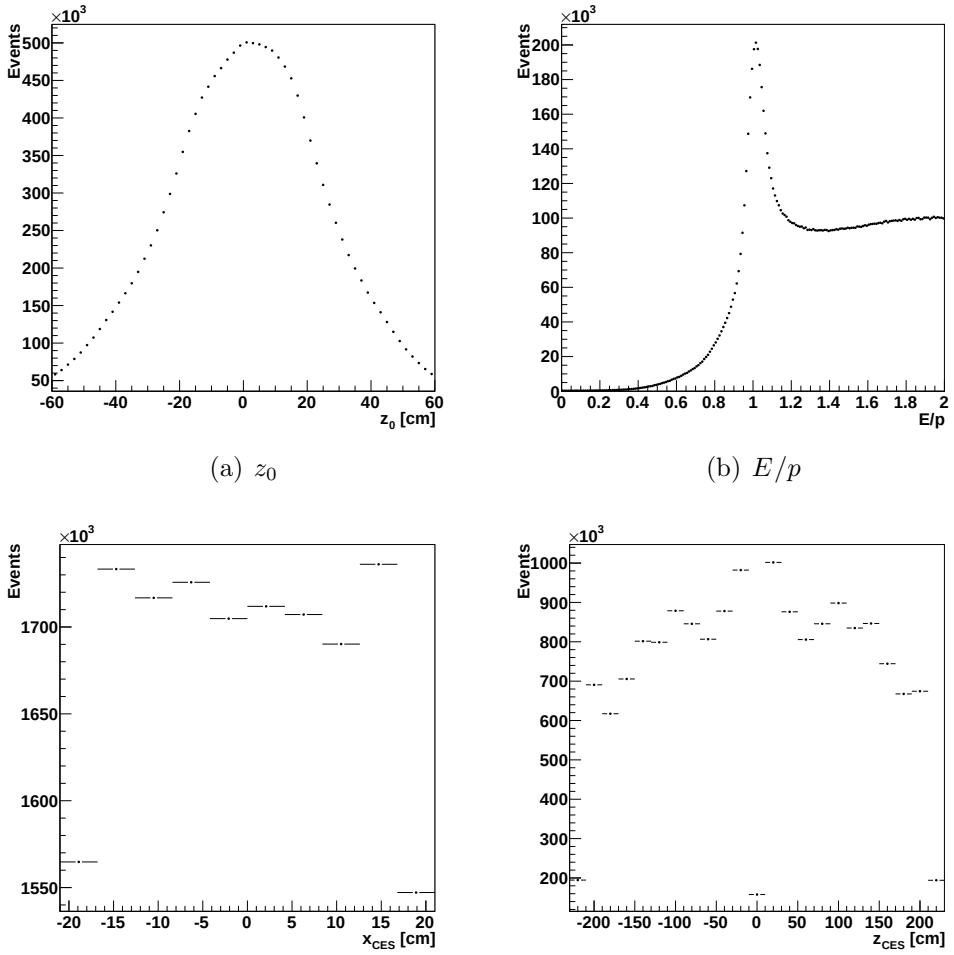

(a) z_0 (b) E/p

(c) x_{CES} (d) z_{CES}

Figure 4.1: Cut variables for electron candidates before cuts are applied. (a) The distribution of the primary interaction point, z_0. (b) The E/p distribution has a peak at unity and the tail below unity that is produced by calorimeter resolution and energy leaking out of the calorimeter. The high tail above unity is caused by bremsstrahlung from the primary electron in the decay. (c) The lower response at the edge of a calorimeter wedge is observed for $|x_{\mathrm{CES}}| > 18$ cm. (d) The gap between calorimeter halves is observed for $|z_{\mathrm{CES}}| < 12$ cm.

Lepton	$\lvert z_0 \rvert \leq 60$ cm
	$30 < p_T^l < 65$ GeV
	Four axial superlayers with at least five hits each
	Four stereo superlayers with at least five hits each
Electron	$p_T^{\text{track}} > 18$ GeV
	$E/p \ < 2$
	$\lvert x_{\text{CES}} \rvert < 18$ cm
	$12 < \lvert z_{\text{CES}} \rvert < 230$ cm
	$E_{\text{HAD}}/E_{\text{EM}} < 0.1$
	$L_{\text{shr}} < 0.3$
	$\lvert \Delta z \rvert < 5$ cm
	Energy deposited in fiducial volume (tower 9 excluded)
Muon	$\lvert d_0 \rvert \leq 0.1$ cm
	$\chi^2/\text{dof} < 3$
	$E_{\text{EM}} < 2$ GeV
	$E_{\text{HAD}} < 6$ GeV
	$(\Delta x_{\text{CMU}}\ , \Delta x_{\text{CMP}}\ , \Delta x_{\text{CMX}}) < (3, 5, 6)$ cm

Table 4.1: The lepton identification cuts. Electron and muon candidates are required to pass the 'lepton' cuts in addition to the specific lepton flavour cuts.

Muon stub reconstuction

The muon stub (see Section 2.2.3) is required to fall in a well-instrumented region of the muon chambers. The muon stub is also expected to be well matched to the associated COT track. Once extrapolated to the appropriate muon chamber, the distance in the $r-\phi$ plane between the extrapolated track and chamber must be less than 3 cm for the CMU, 5 cm for the CMP and 6 cm for the CMX.

4.2 Event selection criteria

Once the lepton candidates have been identified according to the criteria defined in Sections 4.1.1 and 4.1.2, further requirements for a candidate event are utilised to demand that the event be consistent with the production of a W or Z^0. These are described in Sections 4.2.1 and 4.2.2. Reconstructed muon

events must also pass the cosmic muon veto where the pair of muons must both be moving away from the beamline in the $r - \phi$ plane: a cosmic muon is expected to pass straight through the detector and to have one track pointing in toward the beam line and one track pointing out. The cuts are summarised in Table 4.2.

4.2.1 W

At least one candidate lepton is selected according to Section 4.1. The neutrino is not directly measured. Cuts on the kinematic variables used to measure M_W (see Section 3.2) are made as follows.

Transverse mass

The transverse mass, Equation (3.20), is required to be between 60 and 100 GeV. The selects events around the expected peak and Jacobian edge of the transverse mass distribution.

Missing transverse energy

The neutrino produced with the primary lepton in the W decay is not detected and its energy in the $r - \phi$ plane is not recorded. This missing transverse energy ($\not\!\!E_T$), Equation (3.22), is required to be between 30 GeV and 55 GeV, consistent with a missing neutrino.

Lepton transverse momentum

In addition to the p_T^l cuts in Section 4.1, the transverse momentum of the lepton is required to be less than 55 GeV, further selecting events around the expected values and reduces contamination from Z^0 decays in the W sample.

Hadronic recoil

The hadronic recoil ($U = |\mathbf{U}|$) of the event against the W (see Section 3.2) is required to be less than 15 GeV. The recoil is proportional to the energy recorded by the calorimeter and events with a higher measured recoil are more likely to have contamination from background QCD processes. A recoil cut indirectly cuts on the transverse momentum of the boson.

4.2.2 Z^0

Z^0 events require that at least two charged candidate leptons are selected according to Section 4.1.

Invariant mass

The reconstructed mass of the two leptons must fall within the region 66 GeV to 116 GeV. This selects events around the expected Z^0 peak of approximately 91 GeV.

Time of flight

In order to reduce background from cosmic events, a candidate event is required to pass from the interaction point and through the COT in less than 4 ms (ΔT_0). This is to remove events depositing energy in the calorimeters that occur "out of time" with the crossing of the $p\bar{p}$ beams.

Transverse momentum

The momentum of the Z^0 in the $r - \phi$ plane, p_T^Z, is required to be less than 30 GeV. This cut makes the transverse momentum and recoil in Z^0 events comparable with W events affected by the 15 GeV recoil cut.

Z^0 event	$66 < M_Z < 116$ GeV
	$\lvert\Delta T_0\rvert < 4$ ms
	$p_T^Z < 30$ GeV
	Cosmic veto cut (muons only)
W event	$60 < M_T^W < 100$ GeV
	$30 < \not{E}_T < 55$ GeV
	$p_T^l < 55$ GeV
	$\lvert U\rvert < 15$ GeV
	Cosmic veto cut (muons only)

Table 4.2: The event selection cuts. Z^0 candidate events are required to have two identified charged leptons. W candidate events require one identified charged lepton.

Chapter 5

Event generation

This analysis uses a bespoke fast simulation of the CDF detector developed from a previous analysis of the W decay width [54]. It is necessary to develop a fast simulation of CDF because of finite computing power. In order to measure systematic effects on the W mass to within 5–10 MeV, it is desirable for the statistical uncertainty arising from Monte Carlo events to be 0.5 MeV or smaller. This precision requires $\mathcal{O}$(500 million) of events. The CDF collaboration has built a simulation of the detector, `cdfSim`, based upon `GEANT3` [55] but generating $\mathcal{O}$(500M) events takes too long to be of utility in the W mass analysis. This fast simulation is being used in conjunction with the fast simulation developed for the previous W mass measurement at CDF [40] for the current W mass analysis in preparation [56].

The production and decay of weak bosons in Drell-Yan [57] events is simulated at next-to-leading order (NLO) in electroweak physics using `HORACE` [58], with the final state boosted by randomly sampled transverse momenta generated using a resummed calculation of next-to-leading order quantum chromodynamics (QCD) [59]. The QCD calculation is the same approach as used in the `RESBOS` [60] event generator.

The response of the detector to particles from QCD radiation, spectator quarks and multiple (minimum bias) interactions are described by a parametric model tuned to Z^0 decays.

5.1 W and Z^0 production

A Monte Carlo event generator produces particles by randomly assigning the momentum fractions, x_1 and x_2 to the colliding quark and antiquark, as well as the flavour of the colliding quarks. As seen in Equation (3.5), the x_1 and x_2 of the quark-antiquark pair is used to calculate the squared centre-of-mass energy for the collision of the event, $\hat{s} = x_1 x_2 s$. At leading order in QCD and electroweak theory, Figure 5.1, there is no net transverse momentum between the colliding quark and antiquark. This implies

$$P_1 = \frac{\sqrt{s}}{2}(x_1, 0, 0, x_1) \text{ and} \tag{5.1}$$

$$P_2 = \frac{\sqrt{s}}{2}(x_2, 0, 0, -x_2) \tag{5.2}$$

where P_1 is assumed to be the quark or antiquark emitted by the proton and P_2 is from the antiproton. The produced boson has energy and longitudinal momentum given by

$$E_W = \frac{\sqrt{s}}{2}(x_1 + x_2) \text{ and} \tag{5.3}$$

$$|\mathbf{p}_L^W| = \frac{\sqrt{s}}{2}(x_1 - x_2) \tag{5.4}$$

with a rapidity

$$y_W = \frac{1}{2}\ln\frac{E_W - |\mathbf{p}_L^W|}{E_W + |\mathbf{p}_L^W|} = \frac{1}{2}\ln\frac{x_1}{x_2} \quad . \tag{5.5}$$

The final state leptons are constructed in the centre-of-mass frame and assigned a random direction in θ and ϕ. The final state of the event is Lorentz boosted into the lab frame, Equation (3.12), where $\beta_L = |\mathbf{p}_L^W|/E_W$.

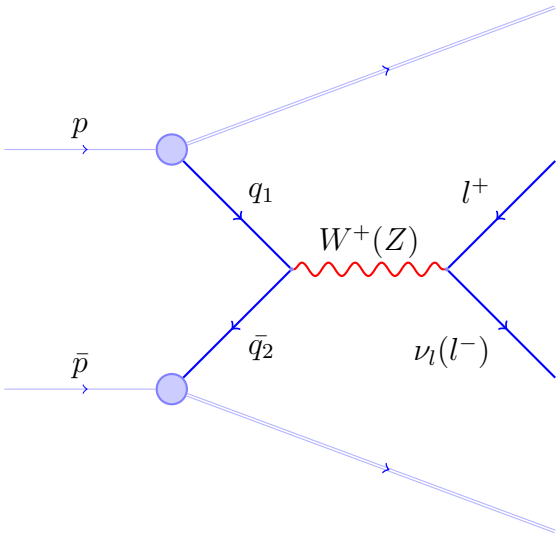

Figure 5.1: The generic production and decay of a weak boson from colliding beams of $p\bar{p}$ particles.

The event is given a series of multiplicative weights. The cross section as calculated from the matrix element of the process is included as an event weight. The event is given a further weight to account for the deviation of the event's $\sqrt{\hat{s}}$ from the Breit-Wigner resonance at M_W or M_Z:

$$\frac{1}{\left(\hat{s} - M^2\right)^2 + \Gamma^2 M^2} \tag{5.6}$$

where M is the mass of the boson and Γ is the decay width. The event is also given a weight to ensure that the charged lepton obeys the correct angular distribution, this is discussed in Section 5.4.2. The probabilities associated with the momentum fractions of the colliding quarks are obtained from the correct parton distribution functions, assigned as a weight. This is discussed in more depth in Section 5.2.

5.2 Parton density functions

As mentioned in Section 5.1, the events are assigned additional weights to account for the composite nature of the colliding proton and antiprotons. The

structure of the colliding hadrons are described by parton distribution functions (PDFs) produced by dedicated researchers. For this analysis the Les Houches Accord PDF Interface (LHAPDF) [61] is used to obtain $f_q(x_q, Q_q^2)$, the probability of a quark (antiquark) of flavour q being emitted by the colliding proton (antiproton) with a momentum fraction, x, and squared centre-of-mass energy, Q^2. The $f_q(x_q, Q_q^2)$ for the quark from the proton and antiquark from the antiproton are both included as multiplicative event weights. The x_1 and x_2 affect the rapidity of the weak boson as Equation (5.5) shows, and this analysis is restricted to the central region of CDF which is approximately $|\eta| < 1$. The rapidity of the boson affects the pseudorapidity of the charged lepton; hence, the acceptance of the detector is indirectly affected by the boson rapidity which depends upon the PDF used and its uncertainty. A detailed study of PDFs and their increasing importance in M_W measurements is discussed in Section 6.1.

5.3 Electroweak corrections

The effect of additional quantum electrodynamic (QED) and electroweak interactions is simulated by using the `HORACE` [58, 62] event generator to produce the final state leptons. It can produce W [62] and Z^0 [58] bosons using a matrix element calculation that is correct to $\mathcal{O}(\alpha)$ in perturbative electroweak theory.

The $\mathcal{O}(\alpha)$ matrix element calculation contains both the virtual and real corrections to the leading order matrix element. The real corrections are partitioned into two pieces by means of an energy cut: the emission of a "hard" photon in the matrix element off one of the charged leptons in the final state (bremsstrahlung); and the emission of "soft" photons which are low-energy or are emitted collinear to the parent lepton. These soft real photons cause the

calculation to diverge but this divergence is cancelled by including soft virtual photons in the final result [62]. In addition to virtual soft photons, the virtual corrections include vertex, box and boson self-energy corrections which become important at high $\hat{s}$ [63].

The emission of more than one photon is simulated by means of a next-to-leading-logarithm (NLL) photon showering process analogous to parton showering. The NLL photon shower is matched to the NLO matrix element expansion so that they are identical at $\mathcal{O}(\alpha)$. This matched mode of operation is used in this analysis. The HORACE authors have checked their numerical results against alternative next-to-leading order event generators and found excellent agreement [64, 65].

5.4 QCD corrections

The effect of beyond leading-order quantum chromodynamics (QCD) is included in the generation of W and Z^0 bosons by modelling the dominant processes that depart from the leading-order interaction. Examples of such processes are shown in Figure 5.2. Ideally, the effect of next-to-leading order and resummed QCD would be included with next-to-leading order electroweak physics but no such generator exists. This forces a choice between using an NLO QCD generator such as RESBOS [60] and modelling the effect of electroweak physics, the method used in the first Run-II measurement of M_W [40], or using an NLO electroweak generator and modelling QCD as used in the first Run-II measurement of Γ_W [54]. While there is no single generator that contains all the effects of interest in the M_W measurement, such a tool may be available in the future [66].

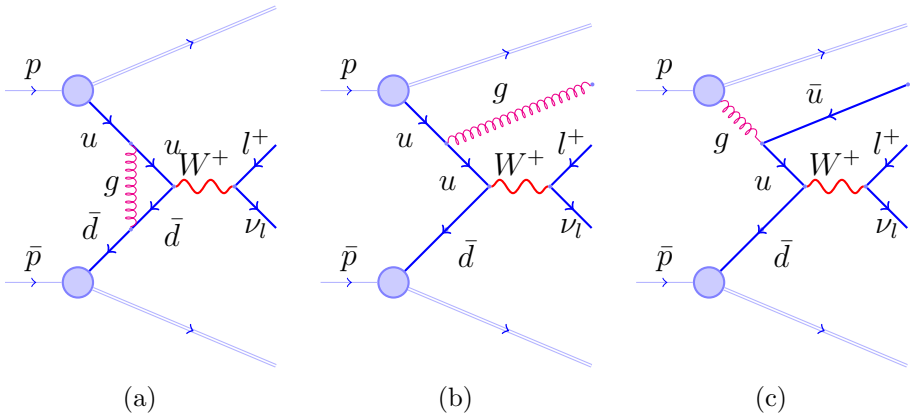

Figure 5.2: Examples of W production and leptonic decay with next-to-leading order QCD effects: (a) a gluon exchanged between the quarks; (b) the emission of a gluon off one of the quarks prior to the collision; and (c) the emission of a gluon from the colliding proton which produces a quark-antiquark pair that interacts with an antiquark emitted from the antiproton.

5.4.1 Transverse momentum

One of the dominant contributions of higher-order QCD is the emission of initial state gluon radiation as discussed in Section 3.2 and shown in Figure 5.2. The emission of gluons imparts a transverse momentum on the colliding quark and antiquark which is manifest in the transverse momentum of the W, $|\mathbf{p}_T^W|$. While the primary fit distribution, M_T^W, only has a second order kinematic sensitivity to $|\mathbf{p}_T^W|$, the transverse momentum is an input for the parameterisation of the hadronic recoil which is used to infer the neutrino properties (see Section 5.5.5).

The higher-order corrections to the differential cross-section of weak boson production are of the form [11]:

$$\frac{1}{\sigma}\frac{d\sigma}{dp_T^2} \approx \frac{1}{p_T^2}\left[C_1\alpha_s \ln\frac{M^2}{p_T^2} + C_2\alpha_s^2 \ln^3\frac{M^2}{p_T^2} + C_n\alpha_s^n \ln^{2n-1}\frac{M^2}{p_T^2} + \cdots\right] \tag{5.7}$$

where M is the mass of the boson and the C_i coefficients are calculated separately. For transverse momenta less than 10–15 GeV the higher-order logarithmic terms begin to dominate the cross-section, and the series diverges as

the transverse momentum approaches zero [11]. Events with high-$|\mathbf{p}_T^W|$ are the result of hard gluon initial state radiation and are well described in perturbative QCD; however, the low-$|\mathbf{p}_T^W|$ region is dominated by multiple soft and collinear gluon emissions where the divergence in the perturbative QCD calculation require the resummation formalism of Collins, Soper and Sterman (CSS) [67]:

$$\frac{d^3\sigma}{d\hat{s}dp_T^2dy} = \frac{1}{(2\pi)^2}\delta\left(\hat{s} - M^2\right)\int \widetilde{W}(b_*)\widetilde{W}^{NP}(b)e^{i\vec{p}_T\cdot\vec{b}}d^2b + Y(p_T) \tag{5.8}$$

where M is the mass of the boson. The CSS approach splits the cross-section into components calculable in perturbative NLO QCD, $\widetilde{W}(b_*)$ and $Y(p_T)$, and a non-perturbative component, $\widetilde{W}^{NP}(b)$. The $\widetilde{W}(b_*)$ and $\widetilde{W}^{NP}(b)$ components are integrated in b-space, the Fourier inverse of the transverse momentum, where b_* is defined in Equation (5.9):

$$b_*(b, b_{\max}) = \frac{b}{\sqrt{1 + (b/b_{\max})^2}}. \tag{5.9}$$

The $\widetilde{W}^{NP}(b)$ term is an ad hoc phenomenological model constrained by low-energy Drell-Yan and Run-I Tevatron data. There have been multiple versions suggested by various authors: Davies, Webber and Stirling (DWS), Equation (5.10) [68]; Ladinsky and Yuan (LY), Equation (5.11) [60]; and Brock, Landry, Nadolsky and Yuan (BLNY), Equation (5.12) [69, 70]. The BLNY model is used in this analysis and the global fit values are presented in Table 5.1.

$$\widetilde{W}^{NP}_{DWS}(b) = \exp\left(-g_1 - g_2\ln\left(\frac{Q}{2Q_0}\right)\right)b^2 \tag{5.10}$$

$$\widetilde{W}^{NP}_{LY}(b) = \exp\left(b^2\left[-g_1 - g_2\ln\left(\frac{Q}{2Q_0}\right)\right] - bg_1g_3\ln\left(100\cdot x_1x_2\right)\right) \tag{5.11}$$

$$\widetilde{W}^{NP}_{BLNY}(b) = \exp\left(-g_1 - g_2\ln\left(\frac{Q}{2Q_0}\right) - g_1g_3\ln\left(100\cdot x_1x_2\right)\right)b^2 \tag{5.12}$$

g_1	0.21 ± 0.01 GeV^2
g_2	$0.68^{+0.01}_{-0.02}$ GeV^2
g_3	$-0.6^{+0.05}_{-0.04}$ GeV^2

Table 5.1: The value of the phenomenological tuning parameters obtained by Brock *et al.* for their choice of $\widetilde{W}^{NP}$, Equation (5.12), with $Q_0 = 1.6$ GeV and $b_{\max} = 0.5$ GeV^{-1} [70].

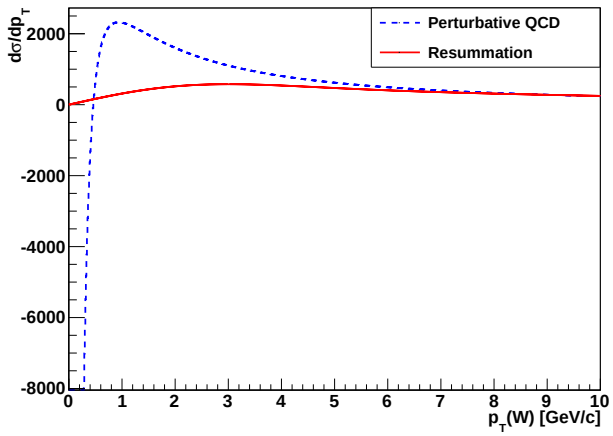

Figure 5.3: The next-to-leading order QCD prediction for $|\mathbf{p}_T^W|$ at a fixed rapidity ($y = 0.35$) compared with the soft gluon resummation prediction. The divergence in the perturbative QCD calculation can clearly be seen.

This analysis uses Arnold, Brockway, Ellis and Reno's calculation [59] of perturbative NLO QCD matched to Arnold, Brockway, Kauffman and Russel's soft gluon resummation [71], albeit modified to use the BLNY non-perturbative component. The perturbative calculation is compared with the resummed cross-section in Figure 5.3.

For a nominal choice of phenomenological input g_i parameters, boson rapidity, y_0, and centre-of-mass energy, $\hat{s}_0$, a probability density function is created and sampled to obtain a specific $|\mathbf{p}_T|$ for a Z^0 or W event. The event is Lorentz boosted by this amount in the transverse plane. As this probability density function is produced using nominal values for y_0 and $\hat{s}_0$ and every event has values for y_{gen} and $\hat{s}_{\text{gen}}$ obtained from the quark momentum fractions, Equation (3.5) and Equation (5.5), the event weight is adjusted by the

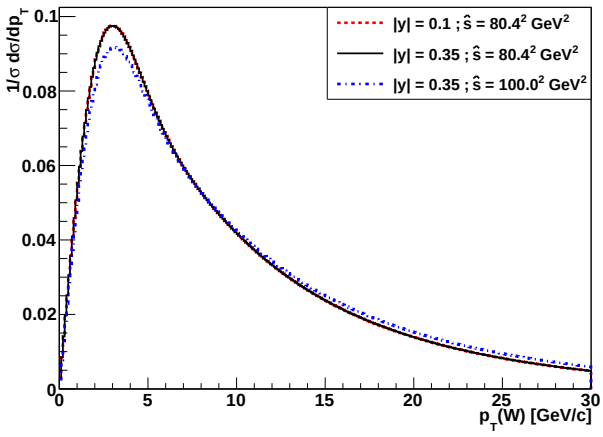

Figure 5.4: The different predictions for $d\sigma/dp_T$ in W events at different rapidities, y, and centre-of-mass energies, $\hat{s}$. The distributions have been normalised to unity. The generator obtains a random $|\mathbf{p}_T^W|$ by sampling $d\sigma/dp_T$ at $|y| = 0.35$ and $\sqrt{\hat{s}} = 80.403$ GeV. A weight it applied to events to correct for the different $y = 0.5\ln(x_1/x_2)$ and $\hat{s} = x_1 x_2 s$ in the event.

following multiplicative weights:

$$w(|\mathbf{p}_T^W|, y_{\text{gen}}, \hat{s}_{\text{gen}}) = \frac{\frac{d\sigma}{d|\mathbf{p}_T^W|}(|\mathbf{p}_T|; y_{\text{gen}}, \hat{s}_{\text{gen}})}{\frac{d\sigma}{d|\mathbf{p}_T^Z|}(|\mathbf{p}_T|; y_0, \hat{s}_0)} \text{ or} \tag{5.13}$$

$$w(|\mathbf{p}_T^Z|, y_{\text{gen}}) = \frac{\frac{d\sigma}{d|\mathbf{p}_T^Z|}(|\mathbf{p}_T|; y_{\text{gen}}, \hat{s}_0)}{\frac{d\sigma}{d|\mathbf{p}_T^Z|}(|\mathbf{p}_T|; y_0, \hat{s}_0)} \tag{5.14}$$

where $\frac{d\sigma}{d|\mathbf{p}_T^V|}(|\mathbf{p}_T|; y, \hat{s})$ is the prediction of the Arnold calculation for the V weak boson ($V \in \mathrm{W}, \mathrm{Z}^0$) cross-section differential in $|\mathbf{p}_T^V|$ at a squared centre-of-mass energy, $\hat{s}$, and boson rapidity, y. Figure 5.4 shows examples of the distributions used to obtain the re-weighting functions and the corresponding re-weighing functions are presented in Figure 5.5.

5.4.2 Angular momentum

W bosons produced from valence quarks at leading-order in QCD with no transverse momentum are polarised along the beam axis with a differential cross-section described by

$$\frac{d\sigma}{d(\cos\theta)} \propto (1 - q_v \cos\theta)^2 \tag{5.15}$$

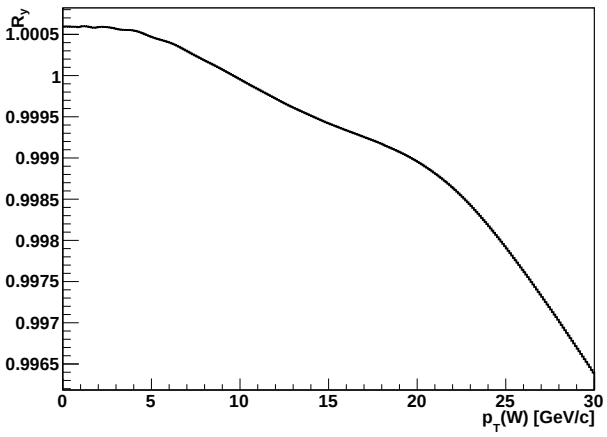

(a) Rapidity reweighting function

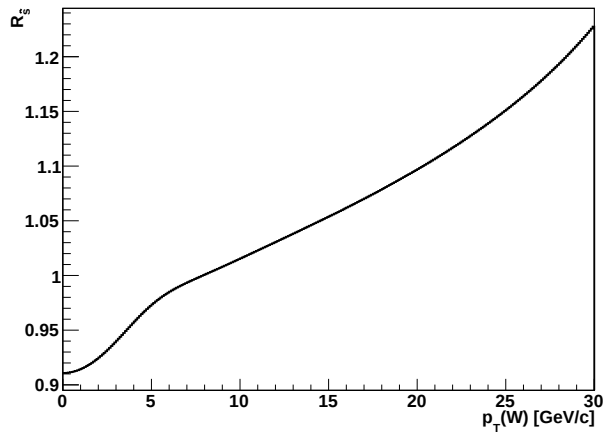

(b) $\hat{s}$ reweighting function

Figure 5.5: Two sample reweighting functions obtained using the $d\sigma/dp_T$ predictions in Figure 5.4. (a) The rapidity function reweights an event from $|y| = 0.35$ to $|y| = 0.1$. (b) The $\hat{s}$ function reweights an event from $\sqrt{\hat{s}} = 80.403$ GeV to $\sqrt{\hat{s}} = 100$ GeV.

where q_v is the charge of the boson and θ is the polar angle of the negatively (positively) charged lepton produced in the decay with respect to the proton (antiproton) direction. This asymmetry arises as a result of the V-A coupling in the electroweak sector that links left-handed antineutrinos with right-handed electrons and muons, and right-handed neutrinos with left-handed positrons and antimuons. For the case of W^+ (W^-) bosons the up quark (antiquark) is emitted by the incoming proton (antiproton) which gives the boson a preferential boost in the positive (negative) z-axis direction and the W^+ (W^-) has its spin aligned in the positive z-axis direction. The positively (negatively) charged lepton is preferentially emitted in the positive (negative) z-axis direction because the associated neutrino (antineutrino) is forbidden to have a right- (left-) handed helicity.

When higher-order terms in QCD are considered the differential cross-section is described by Equation (5.16) where p_T and q_v are the transverse momentum and charge of the boson, and ϕ and θ are the azimuthal and polar angles of the lepton produced in the decay as defined in the Collins-Soper frame [72]. The Collins-Soper frame, Figure 5.6, is an arrangement of the rest frame of the W where the plane of the incoming quarks defines the xz-plane and the y-axis is perpendicular to it. The azimuth and polar angles are defined by the lepton decaying from the W. The effects of QCD are folded up in p_T-dependent coefficients, A_i. In the zero-transverse momentum case the only non-zero coefficient is A_4 and Equation (5.15) is reproduced.

The effect of next-to-leading order QCD is not included in the `HORACE` generator and is added by means of a multiplicative weight. This is the first time that the systematic effect of the helicity effects arising from NLO QCD has been studied for a W measurement. The previous CDF M_W analysis

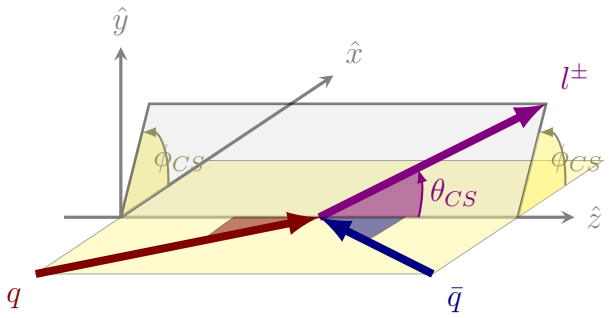

Figure 5.6: The Collins-Soper frame. The incoming quarks and antiquark, and the primary lepton are shown in the rest frame of the W.

[40] has evaluated the $|\mathbf{p}_T^W|$-dependence of the A_i functions in `RESBOS` but no systematic error was estimated.

$$\begin{aligned}\frac{d^3\sigma}{dp_T^2 d\phi d(\cos\theta)} &\propto (1+\cos^2\theta) + \frac{A_0}{2}(1-3\cos^2\theta) \\ &- A_1 q_v \sin 2\theta \cos\phi + \frac{A_2}{2}\sin^2\theta\cos 2\phi \\ &+ A_3 \sin\theta\cos\phi - A_4 q_v \cos\theta \\ &+ A_5 \sin^2\theta \sin 2\phi - A_6 q_v \sin 2\theta \sin\phi \\ &+ A_7 \sin\theta\sin\phi \\ &= f_{\mathrm{NLO}}(p_T,\theta,\phi). \end{aligned} \tag{5.16}$$

The additional angular information is implemented in the fast simulation by constructing the Collins-Soper frame from the final state particles, and re-weighting each event by the ratio of angular components:

$$w_{\mathrm{NLO}}(p_T,\theta,\phi) = \frac{f_{\mathrm{NLO}}(p_T,\theta,\phi)}{(1-q_v\cos\theta)^2} \tag{5.17}$$

where f_{NLO} is the angular term defined in Equation (5.16).

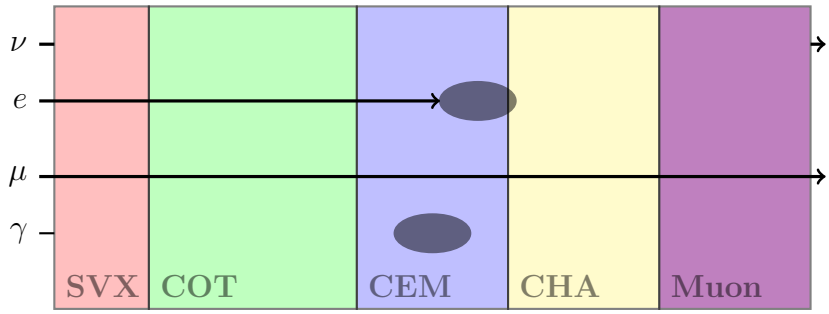

Figure 5.7: A schematic representation of the passage of particles through the detector: neutrinos are not detected; electrons leave track hits in the tracking chambers and deposit energy in the CEM; photons do not leave tracks and deposit energy in the CEM; and muons leave tracks and minimal energy deposits in the CEM and CHA. The time-of-flight counter (TOF) and magnetic solenoid are located between the COT and CEM.

5.5 Detector simulation

The particles produced by the event generator are propagated through a bespoke fast simulation of CDF. Many millions of events need to be simulated in order to study systematic uncertainties at the level of precision required for a 25–30 MeV measurement of the W mass. For this reason a fast parametric model of CDF has been expanded from a previous analysis [54]. A schematic overview of the response of CDF to particles is shown in Figure 5.7: only charged particles are detected in the tracking systems (silicon trackers and COT); electrons and photons produce electromagnetic showers in the CEM which may leak into the CHA; muons leave minimal energy deposits in the CEM and CHA, and are detected in the muon chambers (CMX, CMU and CMP); and neutrinos are not detected at all.

5.5.1 Particle energy loss

The energy loss of particles as they pass through the detector is simulated on a per-particle basis. Electrons are affected by bremsstrahlung induced by the nuclei of the material in the detector volume, Møller scattering (Bhabha scattering for positrons) off the electrons in the detector material, and ionisation.

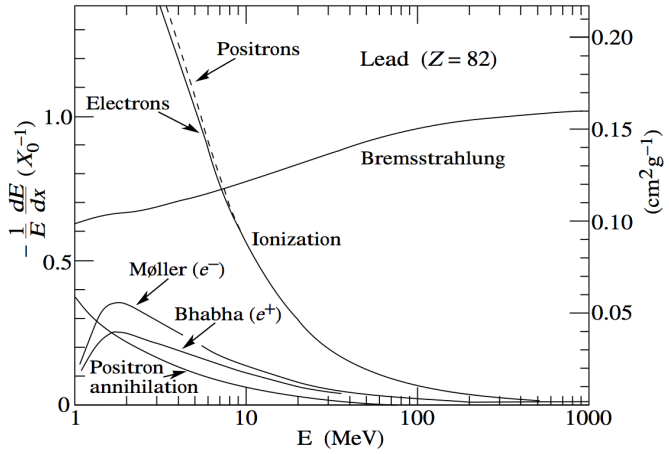

Figure 5.8: The sources of energy loss for electrons and positrons passing through lead. The electrons and positrons from the weak boson decay are typically of the order of 40 GeV which have bremsstrahlung and ionisation as the major cause of energy loss. [4]

An example of the amount of the energy lost from these processes is shown in Figure 5.8 for electrons traveling through lead (the passive material in the CEM).

The energy loss of electrons from bremsstrahlung and ionisation is simulated using a model based upon `GEANT4` [73] theory and cross-checked against `GEANT4` in a "test-beam" analysis. The material traversed by an electron is estimated using `SiliMap` [74], a geometric map of the material in CDF. `SiliMap` is too crude for a M_W analysis on its own; hence, the output of `SiliMap` is adjusted to match data (see Section 5.5.4).

For every electron in the event, the total bremsstrahlung cross-section and differential bremsstrahlung cross-section are calculated and sampled to produce photons. For every photon in the event, pair-production cross-sections are calculated and sampled to produce electron-positron pairs. The bremsstrahlung and pair production steps are repeated for any new particles created until all particles have been processed.

The fractional energy lost by an electron of energy E by emitting a photon with energy, k, is defined by $y = \frac{k}{E}$. A basic functional form describing the

bremsstrahlung cross-section is [4]:

$$\frac{d\sigma}{dy} = \frac{A}{yX_0N_A}\left(\frac{4}{3} - \frac{4}{3}y + y^2\right) \tag{5.18}$$

where A is the atomic number of the absorbing material, N_A is Avogadro's number, and X_0 is the number of radiation lengths in the absorbing material. This basic form breaks down as y approaches zero. At low-y, Equation (5.18) neglects dielectric suppression and the Landau-Pomeranchuk-Migdal (LPM) effect. The LPM effect arises from quantum interference between neighbouring atoms which suppresses the cross-section [75].

Muons from weak boson decays have energies of the order of 40 GeV which falls into the "Bethe" region of Figure 5.9 [4]. The mean energy loss can be described by

$$-\langle\frac{dE}{dx}\rangle = Kz^2\frac{Z}{A}\frac{1}{\beta^2}\left[\frac{1}{2}\ln\frac{2M_e\beta^2\gamma^2T_{\max}}{I^2} - \beta^2 - \frac{\delta(\beta\gamma)}{2}\right] \tag{5.19}$$

where Z and A are the atomic number and atomic mass of the absorbing material and I is the mean excitation energy, β and γ are the kinematic variables $|\mathbf{p}_T|/E$ and $(1-\beta^2)^{-1/2}$, respectively, encountered in Section 3.2, M_e is the mass of the electron, and $T_{\max}$ is the maximum kinetic energy that can be imparted on a electron in a single collision:

$$T_{\max} = \frac{2M_e\beta^2\gamma^2}{1 + 2\gamma M_e/M_\mu + (M_e/M_\mu)^2} \tag{5.20}$$

and M_μ is the mass of the muon.

5.5.2 Momentum resolution

A charged particle traveling through the tracking systems has a curved trajectory in the magnetic field according to Equation (2.8). The signed reciprocal

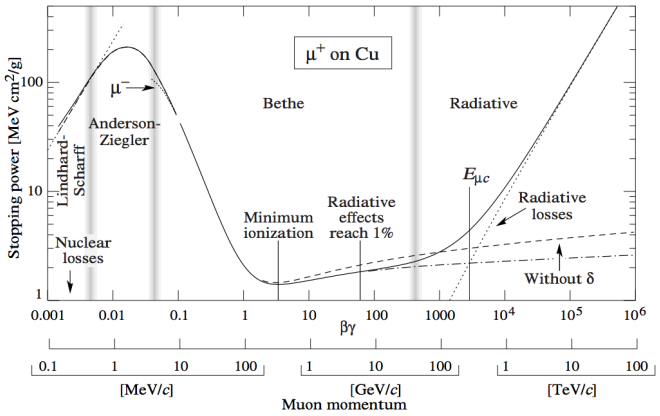

Figure 5.9: The stopping power, $-\langle dE/dx \rangle$, of copper for a muon over a large range of momentum. The muons from weak boson decays fall in the "Bethe" regime. [4]

of the transverse momentum for a particle with charge, q, and transverse momentum, p_T, is

$$P_r = \frac{q}{p_T}. \tag{5.21}$$

The momentum resolution, $\Delta(1/p_T)$, is related to the difference between the true reciprocal transverse momentum and the reconstructed track reciprocal transverse momentum:

$$\Delta P_r = \left(\frac{q}{p_T}\right)_{\text{reco.}} - \left(\frac{q}{p_T}\right)_{\text{true}} \tag{5.22}$$

via $\Delta(1/p_T) = \Delta(P_r/q)$.

The momentum resolution of the simulation is obtained from $W \rightarrow \mu\nu$ events using `cdfSim`. The distribution is approximately Gaussian with a mean centred at $\Delta P_r = 0$ and a standard deviation of 4.7×10^{-4} $(\text{GeV})^{-1}$ [54]. The momentum resolution obtained from `cdfSim` is sampled and the corresponding ΔP_r is applied to particles in the final state.

5.5.3 Calorimeter response

The central electromagnetic calorimeter (CEM) has an energy resolution described by Equation (2.9) in Section 2.2.2. In addition to the resolution the

measured energy differs from the input energy due to the response of the calorimeter which, in general, is not unity. This is assumed to be linear: $E_T^{\text{meas.}} = S_{\text{CEM}} \cdot E_T^{\text{input}}$ where S_{CEM} is variable extracted from data.

Variations in the calorimeter response arise from a number of different sources; however, these can be accounted for by offline calibrations of the data. The central region of a calorimeter tower can have a reduced response because the scintillator light has a greater distance to travel thereby increasing the amount of attenuation. The scintillators are also believed to be ageing which induces a time-dependent response. Any residual effects remaining after the calibration of the CEM performed by the collaboration propagate into S_{CEM} and κ_{CEM}.

The values of S_{CEM} and κ_{CEM} are obtained by fitting Monte Carlo events against $\text{Z}^0 \rightarrow e^+e^-$ invariant mass and $\text{W} \rightarrow e\nu$ E/p data. These distributions are sensitive to electron energy loss and photon production in flight: bremsstrahlung is assumed to be collinear with the parent electron and is clustered into the electromagnetic shower of the electron in the calorimeter; however, photons are not measured by the tracking systems and the total measured momentum associated with the electron is reduced. This gives E/p a long tail above unity. Alternatively, electron showers may be incident toward the edge of a tower and some of the resulting shower may be lost into uninstrumented regions of the detector, this causes the E/p distribution to have a tail below unity. The best-fit S_{CEM} and κ_{CEM} from the $\text{W} \rightarrow e\nu$ E/p distribution are determined to be $S_{\text{CEM}} = 1.01202 \pm 0.00009$ and $\kappa_{\text{CEM}} = (0.94 \pm 0.03)\%$.

5.5.4 Material scale

The amount of material traversed by an electron is obtained using the prediction of `SiliMap` compared with data. This affects the number of bremsstrahlung

photons produced and their energy which in turn affects the momentum measured in the tracking systems. These photons are clustered into the same shower as the parent electron which affects the E/p distribution. In addition, the probability of electron ionisation energy loss is also affected by the material present. The radiation length of material returned by `SiliMap` is adjusted by a scale factor, S_{Mat}, in the fast simulation. S_{Mat} is constrained by fitting to $\text{W} \to e\nu$ E/p data and the best fit S_{Mat} is determined to be 1.042 ± 0.004.

5.5.5 Recoil model

As previously mentioned in Section 3.2, the neutrino is inferred from the hadronic recoil of the event, Equation (3.22):

$$|\mathbf{p}_T^{\nu}| = -|\mathbf{U} + \mathbf{p}_T^{l}|. \tag{5.23}$$

The hadronic recoil is all the transverse energy in the calorimeter that is not from the charged lepton and arises from a number of different sources.

A large source of the recoil comes from gluons recoiling against the weak boson. Initial state gluon emission from the colliding quarks imparts a transverse momentum to the boson. This momentum must be conserved by the subsequent hadronic decay of the gluons into a jet-like structure. This component of the recoil is primarily parallel to the boson transverse momentum and in the opposite direction.

The spectator quarks which are not part of the hard scattering may produce hadronic jets or interact with initial state gluon radiation. Multiple interactions in the beam also contribute to the recoil. The number of multiple interactions is proportional to the number of particles in each beam crossing; hence, this soft component to the recoil is correlated with the instantaneous luminosity of the colliding beams.

The recoil in Z^0 events is decomposed into two directions: one parallel to $-|\mathbf{p}_T^Z|$, U_1 and one transverse to it, U_2. The recoil in each of these directions is simulated as a random Gaussian variable with the means and standard deviations obtained from the following:

$$\langle U_1 \rangle = -P_1 |\mathbf{p}_T^Z| \frac{\ln\left(|\mathbf{p}_T^Z| + P_2\right)}{\ln\left(15 + P_2\right)}, \tag{5.24}$$

$$\langle U_2 \rangle = 0, \tag{5.25}$$

$$\sigma(U_1) = \sigma_{\mathrm{MB}}\left(P_4 + P_5 \cdot |\mathbf{p}_T^Z|\right), \text{ and} \tag{5.26}$$

$$\sigma(U_2) = \sigma_{\mathrm{MB}}\left(P_6 + P_7 \cdot |\mathbf{p}_T^Z|\right) \tag{5.27}$$

where P_1–P_7 are parameters obtained by fitting to $Z^0 \rightarrow e^+e^-$ and $Z^0 \rightarrow \mu^+\mu^-$ data. U_2 has its mean set to zero because it is predominately affected by the soft component of the recoil from the underlying event and multiple interactions, and should have no preferred direction in ϕ. σ_{MB} is a luminosity-dependent function which parameterises the resolution of the underlying event [54].

The transverse momentum of the Z^0 boson is an important input for the model of the hadronic recoil and it is important to understand it before the effect of the detector resolution, acceptance and smearing. Obtaining this true transverse momentum distribution will be discussed in Chapter 7.

Chapter 6

W mass systematics

As has been discussed in the previous sections, the effects of higher-order QCD are inserted into the fast simulation manually. The uncertainty of these effects and their contribution to the systematic uncertainty of the W boson mass needs to be determined and is the focus of this chapter. The transverse momentum distribution of the W boson, $|\mathbf{p}_T^W|$, arising from initial state gluon emission is estimated using Z^0 decays. The $|\mathbf{p}_T^W|$-dependence of the higher-order corrections to the angular distribution of W bosons is investigated using the `DYRAD` [76] and `RESBOS` [60] generators. In addition, the uncertainty of the global fits used to obtain parton distribution function is propagated into the W boson mass.

6.1 Parton density functions

One of the larger systematic errors in the measurement of the W mass M_W at the Tevatron is that arising from the uncertainty in the flavour composition of the proton and the fraction of the (anti) proton momentum carried by quarks and gluons, and their evolution with momentum transfer. Researchers currently use parton distribution functions (PDFs) produced by dedicated groups obtained by global fits to appropriate experimental data.

Two of the main collaborations producing PDFs for the particle physics community are the US-based Coordinated Theoretical-Experimental Project on QCD (CTEQ), a group aimed toward understanding the effect of quantum chromodynamics on the standard model [77]. The other major collaboration is that of Martin, Stirling, Thorne, Watt and formerly Roberts (MRS/MRST/MSTW) [78].

In recent years the PDFs have been presented with a best fit and a number of alternative fits that allow researchers to estimate the effect of the PDF global fit uncertainty upon their own work. However, incompatibilities between datasets — for example, in the normalisation and large χ^2 deviance with respect to the best fit — often mean that phenomenologists sometimes forego rigorous statistical treatment in preference of a more pragmatic approach.

The effect of the uncertainty in parton density functions (PDFs) has become increasingly important in recent years. With large numbers of W bosons produced and recorded at the Tevatron, the relative contribution of statistical uncertainties to the overall error diminishes, leaving the errors that only have a weak dependence on the statistics of the data collected. The previous Run-II measurement of M_W at CDF using data with an integrated luminosity of 200 pb^{-1} had an uncertainty arising from uncertainties in PDFs of 11 MeV for the transverse mass fit [40]. The Run-Ib measurement at CDF using an integrated luminosity of 84 pb^{-1} found a 15 MeV systematic effect from PDFs [79]. Considering that the total errors in these published results were 48 MeV and 89 MeV, respectively, the PDF uncertainty is clearly not reducing as much as other uncertainties with increased integrated luminosity. These figures are presented along with previous DØ measurements in Table 6.1. Hence, the uncertainties arising from PDFs are more significant and are largely independent of statistics.

Experiment	Luminosity (pb^{-1})	ΔM_W^{PDF}	ΔM_W^{TOTAL}
DØ Run-I	82	9	84
CDF Run-Ib	84	15	89
CDF Run-II	200	11	48
DØ Run-II	1000	10	43

Table 6.1: The size of the PDF error in previous M_W measurements at the Tevatron in MeV. The uncertainty arising from PDFs is largely independent of the integrated luminosity of the data [40, 79, 80, 81].

In addition to the importance in single measurements, the contributions of PDFs are a large common error between CDF and DØ for electroweak combinations of the W boson mass and width. The recent electroweak combinations in summer 2009 estimated a total combined uncertainty from Tevatron measurements of 31 MeV on the W mass [82]. The effect of PDFs was assumed to be entirely correlated between CDF and DØ and was 11 MeV [82, 83]. This makes the effect of parton density functions an important error to understand with a goal of reducing the Tevatron M_W uncertainty.

6.1.1 Hessian method

The general form of the χ^2 function used to constrain the PDF models is a linear combination of χ^2 fits to each experiment:

$$\chi^2_{\text{global}} = \sum_n^N \chi^2_n \quad , \tag{6.1}$$

where the χ^2_n is the fit between the PDF model and the experimental data points:

$$\chi^2_n = \sum_{k=i}^{N} \left(\frac{D_{n,k} - M_{n,k}}{\sigma_{n,k}} \right)^2 \tag{6.2}$$

where $D_{n,k}$, $M_{n,k}$ and $\sigma_{n,k}$ are the observed data, global model prediction, and uncertainty of the kth data point of the nth experiment, respectively.[1]

[1] In reality the χ^2-functions can be more complicated if they are constructed to account for correlations.

The χ^2_{global} is then expanded around the minimum point where a region of $\Delta\chi^2$ is defined:

$$\Delta\chi^2_{\text{global}} \leq T^2 \quad , \tag{6.3}$$

where T is the *tolerance* in the fit. If the data used in the fit were all consistent and uncorrelated then the T^2 to obtain the 1σ uncertainty for one parameter would be 1; however, the data used in global fits are not all consistent with one another demanding a larger T^2 or $\Delta\chi^2_{\text{global}}$ than expected. The size of T^2 no longer has an a priori statistical meaning and instead is indicative of the range of alternative global fits deemed to be acceptable. The choice of an acceptable fit differs between CTEQ and MSTW, who choose $T = 10$ [84] and $T = \sqrt{50}$ [85] respectively. The size of the global tolerance is chosen so that $\Delta\chi^2_{\text{global}}$ in the global fit represents the 90% confidence interval.

The Hessian matrix of the global fit is diagonalised to obtain the associated sets of eigenvalues, ϵ, and eigenvectors, ν_i. The eigenvectors form an orthonormal representation of the global fit parameter space so that a displacement in one of the global fit parameters a_i is defined as a linear sum of displacements in the normalised eigenvector directions:

$$a_i - a_i^0 = \sum_{k=1}^{N} \nu_{ik} s_k z_k. \tag{6.4}$$

The normalisation factors, s_k, are chosen so that the sum of all the displacements is no greater than the total uncertainty in the fit: $\sum_{k=1}^{N} z_k^2 \leq T^2$. The quantity z_k represents a displacement along the kth eigenvector.

6.1.2 Error sets

A set of alternative PDF fits, $S_i^{\pm}$, are defined that correspond only to the influence of the ith eigenvector in the positive (S_i^+) and negative (S_i^-) directions. $z_k(S_i^{\pm})$ is set to $\pm t\delta_{ik}$ where t is the displacement along the eigenvector

directions. The Hessian approach requires that the χ^2 function be quadratic; therefore, a displacement t in one of the orthogonal fit parameters increases the T^2 by t^2; hence, $t \equiv T$ by construction. As an example error set, the first alternative PDF set S_1^+ has $z(S_1^+) = \{t, 0, 0, \ldots, 0\}$, the error in the global fit is directed along the first eigenvector and in the positive direction. Alternatively, $z(S_2^-) = \{0, -t, 0, \ldots, 0\}$ produces a PDF where the error is directed in the negative direction of the second eigenvector. $2N$ error sets are created in this fashion.

In the previous generation of MSTW [85] and all CTEQ error sets, the value of t was the same for each eigenvector and was chosen so that the uncertainty in the error sets sufficiently encompassed the experimental error in the global fit. The effect of an experiment on an eigenvector is described in more detail in Section 6.1.3.

If there is an observable $X(S)$ that depends upon PDFs then, from [87], the total uncertainty from all of the eigenvector contributions can be shown to be:

$$\Delta X = \frac{1}{2}\frac{T}{t}\sqrt{\sum_{i=1}^{N}\left(X(S_i^+) - X(S_i^-)\right)^2}. \tag{6.5}$$

For a given PDF and its associated error sets, the size of t is fixed; however, as ΔX is linear in T it is possible to rescale ΔX to estimate the effect if T^2 were chosen differently. This makes it possible to compare the total uncertainty obtained using CTEQ or MSTW PDF errors despite the different views on an acceptable fit tolerance.

6.1.3 Dynamic tolerance

The method outlined in Section 6.1.1 has been improved upon for the latest MSTW PDF sets [86]. Rather than setting a global shift t in the eigenvector

directions that form the total T^2, each eigenvector shift is extracted separately from the data. Recalling that the total χ^2-function is the combination of individual fits to each experiment, Equation (6.1), the shape of χ^2_i as z_k are varied can be used to obtain the confidence intervals for a given experiment and eigenvector.

Confidence intervals for specific eigenvectors can be defined by establishing $\Delta\chi^2_i$ ranges for each individual dataset. This $\Delta\chi^2_i$ range defines the maximum t_i for the eigenvector while maintaining agreement with the experimental data:

$$\Delta\chi^2_i < \frac{\chi^2_{i,0}}{\epsilon_{50}} \cdot (\epsilon_m - \epsilon_{50}) \tag{6.6}$$

where $\chi^2_{i,0}$ is the χ^2 using the global fit values to data from that experiment, and ϵ_m is the χ^2 that encloses the lower m percent of the χ^2 distribution for N data points in the experiment:

$$\frac{m}{100} = \int_0^{\epsilon_m} P_N(\chi^2) \;\; d\chi^2 \tag{6.7}$$

where

$$P_N(\chi^2) = \frac{(\chi^2)^{N/2-1}\, e^{-\chi^2/2}}{2^{N/2} \cdot \Gamma\left(N/2\right)}. \tag{6.8}$$

The median of the χ^2 distribution, ϵ_{50}, converges upon the mean as N gets large[2]; therefore, Equation (6.6) rescales the $\Delta\chi^2_i$ so that the global fit $\chi^2_{i,0}$ is assumed to be the most likely χ^2 for the N data points in the experiment. It is necessary to define the limit in terms of the rescaled $\Delta\chi^2_i$ parameter because some experiments do not agree well with the global fit and have a $\chi^2_{i,0}$ that is larger than the expected χ^2 for the 68% or 90% confidence interval.

Each individual dataset has different t_i parameters for a given eigenvector. MSTW pick the most constraining t_i to define the 68% and 90% confidence

[2]The mean for N degrees of freedon is N, the median is approximately $N\left(1 - \frac{2}{9N}\right)^3$

intervals. This approach permits that different datasets set the 68% and 90% confidence interval and for this reason the value of t_i that defines the 68% confidence interval may not be directly related to the t_i for the 90% confidence interval; therefore, the relative contribution of the eigenvector cannot be assumed to be constant for the different confidence intervals.

CTEQ also perform the same study but rather than set the eigenvector t_i contribution from the most constraining experiment shift, they use the 90% confidence region to determine how large the eigenvector shifts should be in a global sense to correspond to the 90% confidence interval from the individual datasets. This is typically $t \equiv T = 10$ which contrasts with MSTW's choice of $T = \sqrt{50}$ in sets prior to MSTW2008.

6.1.4 Estimating M_W shift

The error-set shifts are combined in quadrature to obtain a total M_W PDF systematic using a modified form of Equation (6.5) which corrects for cases where both the S_i^+ and S_i^- error sets have systematic shifts in the same direction ('odd') and a naïve difference would underestimate the contribution of that eigenvector, Equations (6.9) and (6.10). This is possible because M_W is not an input to the PDF global fit so there is no reason to expect the M_W obtained with the best-fit PDF to be straddled by the values of M_W obtained with the extrema of the fit.

$$\Delta M_W = \frac{1}{2}\sqrt{\sum_{i=1}^{N} \delta_i^2} \quad , \tag{6.9}$$

$$\delta_i = \begin{cases} M_W(S_i^+) - M_W(S_i^-) & \text{'Even'} \\ \max\left(|M_W(S_i^+) - M_W(S_0)|, |M_W(S_i^-) - M_W(S_0)|\right) & \text{'Odd'.} \end{cases} \tag{6.10}$$

The asymmetric systematic shifts are calculated by independently adding up the positive and the negative shifts in quadrature:

$$\Delta M_W^+ = \sqrt{\sum_{i=1}^{N} \delta_{i,+}^2} \quad , \quad \Delta M_W^- = \sqrt{\sum_{i=1}^{N} \delta_{i,-}^2} \quad , \tag{6.11}$$

$$\delta_{i,+} = \max\left(M_W(S_i^+) - M_W(S_0), M_W(S_i^-) - M_W(S_0), 0\right) \tag{6.12}$$

$$\delta_{i,-} = \min\left(M_W(S_i^+) - M_W(S_0), M_W(S_i^-) - M_W(S_0), 0\right). \tag{6.13}$$

6.2 Transverse momentum

As discussed in Section 5.4.1, the transverse momentum of weak bosons in Drell-Yan events arises from the emission of gluons prior to quark-antiquark annihilation. At the Tevatron these events predominantly occur at low-$|\mathbf{p}_T|$ where the prediction of perturbative QCD is unreliable and resummation is preferred. The resummation requires the assumption of an ad hoc parameterisation: the BLNY functional form is used in this analysis.

6.2.1 BLNY phenomenological parameters

The description of the p_T distribution is improved by constraining the phenomenological input g_i parameters with $\mathrm{Z}^0 \to e^+e^-$ and $\mathrm{Z}^0 \to \mu^+\mu^-$ data. At Tevatron center-of-mass energies the effect of g_1 and g_3 is small compared with g_2; therefore, it is only possible to constrain g_2 and the BLNY [69] fit values of g_1 and g_3 are assumed. The BLNY functional form, Equation (5.12), has a logarithmic relationship between $g_1 g_3$ and $x_1 x_2$. This $\hat{s}$-dependence explains the insensitivity to g_3 at the Tevatron where Drell-Yan events are produced predominantly at at fixed $x_1 x_2 = M_Z/\hat{s}$. The insensitivity of g_1 and g_3 can be seen in Figure 6.1 where the difference between $g_i - 3\sigma$ and $g_i + 3\sigma$ in $d\sigma/dp_T$

is shown for each parameter. The ratio plots show interesting features at very low-p_T but this is likely a result of one number that is approaching zero being divided by another number that is approaching zero. Very few events occur with transverse momentum this low so the effect is negligible.

6.2.2 Detector response

The effect of detector resolution and response is modelled using a matrix technique. A large statistics sample is used to generate a $N \times N$ matrix that transforms the generator level p_T^Z histogram of N bins, X_i^{true}, into that affected by detector smearing and response effects, X_j^{meas}. An element of the matrix, M_{ij}, is the sum of weighted events where an event in the ith generator level p_T^Z bin is found in the jth bin after smearing as shown in Equation (6.14). The matrix is normalised according to Equation (6.15).

$$X_j^{\text{meas}} = \sum_{i=0}^{N-1} M_{ij} X_i^{\text{true}} \tag{6.14}$$

$$\sum_{j=0}^{N-1} M_{ij} = 1 \tag{6.15}$$

6.2.3 Parameter fitting

The response matrix described in Section 6.2.2 is used to quickly produce a transverse distribution from a calculation of the p_T^Z-dependent cross-section. This allows for a specific choice of phenomenological parameters to be compared with data. Differential cross-sections are produced for a range of g_2 and ξ. ξ is the value of $\alpha_s(M_Z)$ used to calculate the p_T^Z-dependent cross-section and is used as an additional parameter to constrain the p_T^Z distribution. In all other situations $\alpha_s(M_Z)$ is unchanged from the best-fit $\alpha_s(M_Z)$ for the parton distribution function used.

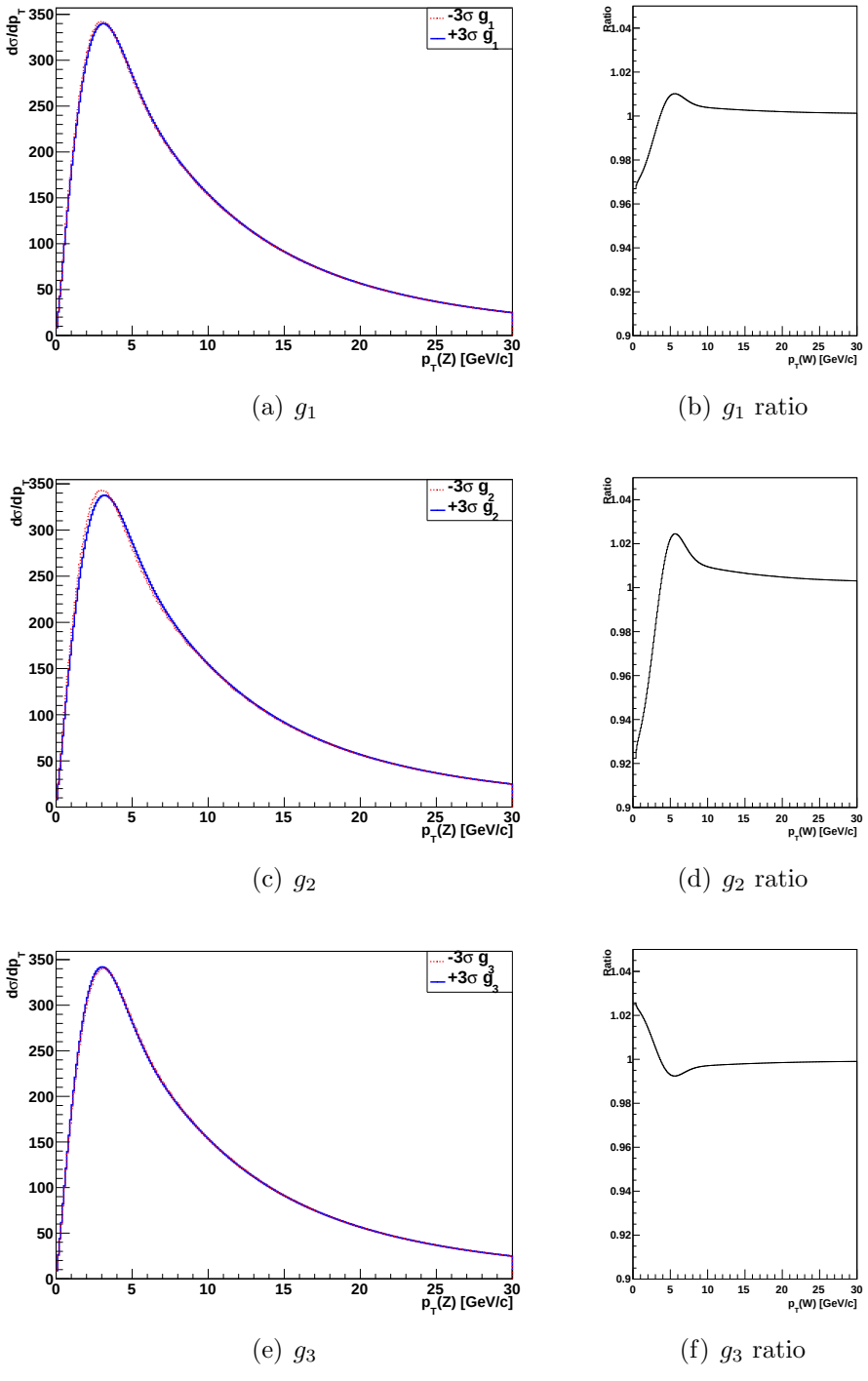

(a) g_1 (b) g_1 ratio

(c) g_2 (d) g_2 ratio

(e) g_3 (f) g_3 ratio

Figure 6.1: The change in $d\sigma/dp_T$ by replacing g_i with $g_i - 3\sigma$ and $g_i + 3\sigma$ for each of the BLNY parameters. The global fit error in [69] is used for each parameter. The ratio between $g_i - 3\sigma$ and $g_i + 3\sigma$ shows the sensitivity of each g_i parameter.

The fit is optimised by producing a binned p_T^Z-dependent cross-section for a grid of g_2 and ξ pairs, and a bicubic spline interpolation in each p_T^Z bin produces a distribution for any choice of g_2 and ξ.

6.3 Angular momentum

The interplay of QCD and the angular distribution is contained in the A_i coefficients of Equation (5.16). The standard model prediction for these coefficients has been obtained from `DYRAD` [76] by Strologas and Errede in [88]. The A_i functions were only obtained for $|\mathbf{p}_T^W| > 20$ GeV in [88] because `DYRAD` is only a perturbative NLO QCD calculation and does not include resummation. As shown in Section 5.4.1, resummation is important in the low-$|\mathbf{p}_T^W|$ region; therefore, `DYRAD` is inadequate for use in a M_W measurement because the majority of events occur at low-$|\mathbf{p}_T^W|$. The evolution of the function toward zero transverse momentum has been determined. The boundary conditions at $|\mathbf{p}_T^W| = 0$ GeV are obtained by assuming the angular dependence is purely V-A: $(1 - q_v \cos\theta)^2$. This expands to

$$1 - 2q_v \cos\theta + \cos^2\theta \tag{6.16}$$

and compared with Equation (5.16) it is obvious that A_4 is 2 and all other functions must be zero. Cubic splines are used to interpolate the A_i functions between the values at 20 GeV and zero. The A_i functions are presented in Figure 6.2.

6.3.1 Improving A_0 and A_4

The evolution of the $\cos\theta$ term in the low-$|\mathbf{p}_T^W|$ region is improved by fitting the relevant A_i functions against `RESBOS` using $\cos\theta$ distributions in different $|\mathbf{p}_T^W|$

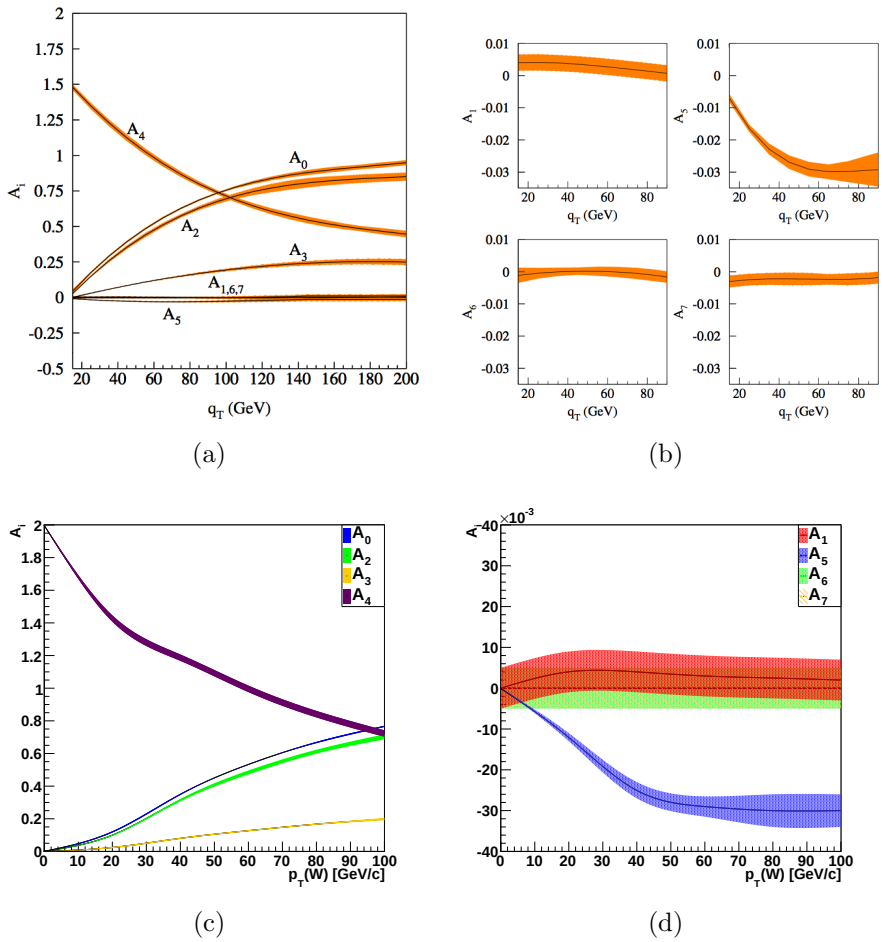

Figure 6.2: The evolution of the A_i coefficients in p_T^W. (a) and (b) show the functions obtained in [88], (c) and (d) show the implementation of these coefficients in the fast simulation. In both cases the shaded regions indicate the uncertainty.

p_T^W (GeV)	A_0	A_4
$0-5$	0.000	2.000
$5-10$	0.020	1.995
$10-20$	0.048	1.950
$20-30$	0.130	1.825
$30-50$	0.240	1.705
$50-100$	0.560	1.300

Table 6.2: The best fit A_0 and A_4 to RESBOS in $\cos\theta$ bins.

ranges. The θ- and ϕ-dependent differential cross-section, Equation (5.16), yields

$$\frac{d^2\sigma}{dp_T d(\cos\theta)} \propto 1 + q_v \frac{2A_4}{2+A_0}\cos\theta + \frac{2-3A_4}{2+A_0}\cos^2\theta \tag{6.17}$$

after integrating over the full range in ϕ.

The $|\mathbf{p}_T^W|$ distribution is partitioned into six ranges, each of which is fit independently to the distribution of $\cos\theta$ generated with RESBOS. The six ranged used are: $0 \leq |\mathbf{p}_T^W| < 5$ GeV, $5 \leq |\mathbf{p}_T^W| < 10$ GeV, $10 \leq |\mathbf{p}_T^W| < 20$ GeV, $20 \leq |\mathbf{p}_T^W| < 50$ GeV and $50 \leq |\mathbf{p}_T^W| < 100$ GeVc. The fit in a specific bin is performed by generating events for a range of values in A_4 with the fast simulation and computing the corresponding χ^2. A parabola is fit to the χ^2 and the minimum of the parabola is the best-fit A_4. This process is repeated to obtain the best-fit A_0.

The value of g_2 extracted from $Z^0 \to e^+e^-$ and $Z^0 \to \mu^+\mu^-$ data will be presented in Chapter 8 along with the ΔM_W contributions of the W transverse momentum, the W helicity cross-section, and the uncertainties arising from PDF error sets.

Chapter 7

Extracting the true Z transverse momentum

As has been discussed in Section 5.5.5, the transverse momentum of the Z^0 boson, $|\mathbf{p}_T^Z|$, is a key input parameter to the parameterisation of the hadronic recoil in W events. The recoil model is implemented before particles in the final state are propagated through the fast simulation of CDF; therefore, knowledge of the Z^0 transverse momentum before any detector effects is desirable. In addition, $|\mathbf{p}_T^Z|$ is also used to extract the g_2 parameter in the BLNY non-perturbative functional form described in Section 5.4.1.

7.1 Smearing matrix and unfolding

The finite resolution and response of the detection systems distort the observed distributions from the underlying true distributions. It is important to include a module that simulates the effect of the passage of particles from the point of generation to the point of detection.

This process can be time consuming so it is beneficial to construct a response or smearing matrix which maps unsmeared data bins to smeared data. Applying this matrix to generator (truth) distributions is intended to replicate

the effect of detector resolution and acceptance effects to allow a comparison between simulated Monte Carlo events and reconstructed data. It follows that if the smearing matrix is inverted then the resulting object can be applied to reconstructed data to estimate the true data without detector interference, this is known as unfolding. The unfolded distribution allows for an easier comparison of data between experiments.

7.1.1 Problems with unfolding

Calculating the mathematical inverse of the smearing matrix is computationally intensive as the size of the matrix increases nor is it guaranteed that the matrix is non-singular. In addition, the correlation between adjacent bins can lead to large fluctuations in the final result that are sensitive to small changes in the reconstructed data, and the final result can be dominated by one or two eigenvectors of the smearing matrix.

Following Blobel [89], a smearing matrix $\mathbf{A}$ which maps from true data $\mathbf{x}$ to the reconstructed data $\mathbf{y}$, can be defined by:

$$\mathbf{Ax} = \mathbf{y} \tag{7.1}$$

which can be inverted to obtain the true data from the measured data:

$$\mathbf{A^{-1}y} = \mathbf{x} \quad . \tag{7.2}$$

$\mathbf{A}$ is a symmetric matrix that can be decomposed into a diagonal matrix of eigenvalues $\mathbf{D}$ and a matrix of eigenvectors $\mathbf{U}$ where $\mathbf{U^T U} = 1$ such that

$$\mathbf{A} = \mathbf{UDU^T} \quad . \tag{7.3}$$

The matrix of eigenvectors $\mathbf{U}$ transforms the true data $\mathbf{x}$ and smeared data $\mathbf{y}$ into and out of a new basis:

$$\mathbf{x'} = \mathbf{U^T x} \quad , \quad \mathbf{y'} = \mathbf{U^T y} \quad , \quad \mathbf{x} = \mathbf{U x'} \quad , \quad \mathbf{y} = \mathbf{U y'} \quad . \tag{7.4}$$

Combining Equations (7.3) and (7.4) yields:

$$\mathbf{UDU^T x = y} \quad , \tag{7.5}$$

$$\mathbf{Dx' = y'} \quad . \tag{7.6}$$

Since $\mathbf{D}$ is a diagonal matrix with eigenvalues λ_i, it has an inverse matrix where $1/\lambda_i$ are the elements of the leading diagonal, leading to:

$$\mathbf{D^{-1}y' = x'} \quad , \tag{7.7}$$

and

$$\mathbf{U^T D^{-1} U y = x} \quad . \tag{7.8}$$

The elements of the unfolded data are sensitive to small eigenvalues of the smearing matrix as a result of the $1/\lambda_i$ factor. For cases where an eigenvector is very small ($\lambda_i \ll 1$) the entire result can be dominated by the statistical fluctuations of the reconstructed data in the transformed basis $\mathbf{y'}$.

7.2 Iterative Bayesian method

One solution to the statistical fluctuation of small eigenvalues in matrix inversion is to ignore the smaller eigenvectors and use a truncated solution. Alternatively, matrix inversion can be avoided entirely and Bayes' theorem used instead.

The smearing matrix can be thought of as a function that links the probability that an event that occurs within one bin in the true distribution x_i is observed in a particular reconstructed bin y_i. If an event has an initial probability of being in the ith bin $P(x_i)$ then $P(y_j|x_i)$ is the conditional probability that it will be reconstructed in a jth bin. Bayes' theorm [90] can then be used

to estimate the probability $P(x_i|y_j)$ that an event reconstructed in the jth bin of $\mathbf{y}$ is originally from the ith $\mathbf{x}$ bin:

$$P(x_i|y_j) = \frac{P(y_j|x_i)P(x_i)}{\sum_{k=1}^{N_x} P(y_j|x_k)P(x_k)}. \tag{7.9}$$

where N_x is the number of bins in $\mathbf{x}$. It should be noted that $\sum_{k=1}^{N_x} P(y_j|x_k)$ can be any value between zero and unity reflecting the possibility that some events are not reconstructed; it is the reconstruction efficiency ϵ_i for that bin. The fact that the total probability must sum to unity and a reconstructed event must come from one of the possible true bins gives the constraints:

$$\sum_{i=1}^{n_x} P(x_i) = 1 \text{ and} \tag{7.10}$$

$$\sum_{i=1}^{n_x} P(x_i|y_j) = 1. \tag{7.11}$$

7.2.1 Iterative algorithm

D'Agostini [91] has proposed an algorithm that uses Equation (7.9) to estimate $P(x_i|y_j)$, the conditional probability that an event reconstructed in the y_j bin is from the x_i true bin, from Monte Carlo events:

$$\hat{N}(x_i) = \frac{1}{\epsilon_i} \sum_{j=1}^{N_y} N(y_j)P(x_i|y_j) \tag{7.12}$$

where $N(y_j)$ is the number of events reconstructed in the y_j bin, $\hat{N}(x_i)$ is the estimated number of events in the x_i true bin, and ϵ_i is the detection efficiency for the x_i bin.

$P(x_i|y_j)$ requires an assumption about the prior probability $P(x_i)$ of an event occurring in the x_i true bin. This prior probability can be improved upon using the following estimator:

$$\hat{P}(x_i) = \frac{\hat{N}(x_i)}{\sum_{j=1}^{n_x} \hat{N}(x_j)} \tag{7.13}$$

and this improved estimate of the prior can be inserted into Equation (7.12) and the process repeated with the number of iterations acting as a controlling parameter.

The RooUnfold [92] ROOT module was used to implement the iterative Bayesian unfolding method.

7.2.2 Iteration parameter

The number of iterations is used to control whether the unfolding distribution is more biased by the Monte Carlo data used to obtain $P(y_j|x_k)$ (lower number) or the measured distribution being unfolded (larger number). Ideally a large number would be desirable but the greater the number of iterations the more susceptible the unfolded distribution is to statistical fluctuations in the reconstructed data.

Monte Carlo samples are generated to contain approximately the same number of events as in the data. Each sample is unfolded and this unfolded distribution is compared with the truth distribution for that sample. This process is repeated for different values of the iteration parameter. Figure 7.1 shows the relative shift in the bin values for one, five and ten iterations. The χ^2 values obtained comparing the unfolded samples with their truth distributions are used to pick the number of iterations and are given in Table 7.1. An iteration parameter of 1 is chosen as it produces unfolded Monte Carlo distribution that best matches the input truth Monte Carlo.

7.3 a_T and a_L kinematic variables

The transverse momentum of the Z^0 is an obvious parameter to unfold in order to extract effects that are sensitive to $|\mathbf{p}_T^Z|$; however, there are alternative variables that may perform better in [93].

Iterations	χ^2/dof
1	0.007/30
2	0.008/30
3	0.009/30
4	0.010/30

Table 7.1: The χ^2 obtained comparing unfolded Monte Carlo samples with the original truth distribution for various iterations of the unfolding algorithm.

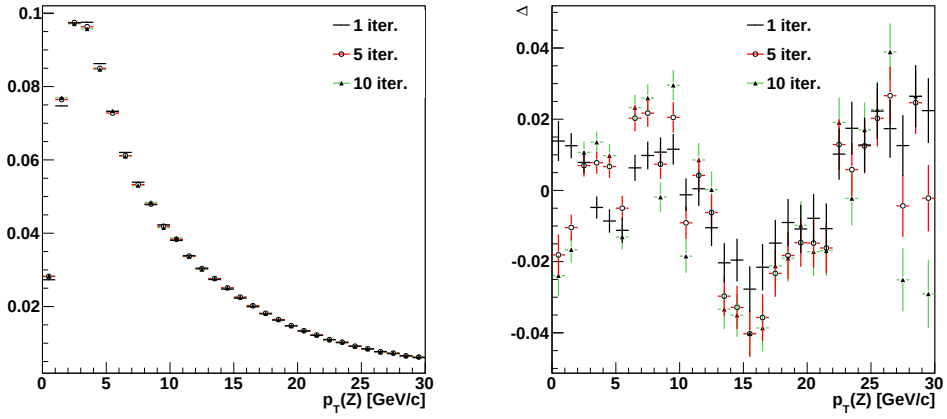

(a) Transverse momentum (b) Relative shift, Δ

Figure 7.1: The effect of increasing the number of iterations of the unfolding algorithm. The greater the number of iterations, the more statistical features in the measured distribution begin to dominate. Monte Carlo samples with the same number of events as in the data are unfolded 1, 5 and 10 times. The parameter Δ is the relative shift of one bin from the corresponding true distribution.

An axis in the rest frame of the Z^0 that is perpendicular to the ϕ bisector between the decaying leptons is defined:

$$\hat{t} = \frac{\mathbf{p}_T^a - \mathbf{p}_T^b}{|\mathbf{p}_T^a - \mathbf{p}_T^b|} \tag{7.14}$$

where $\mathbf{p}_T^a$ and $\mathbf{p}_T^b$ are the transverse momenta of the two leptons. The transverse momentum of the Z^0 is decomposed into components perpendicular (a_T^Z) and parallel (a_L^Z) to $\hat{t}$:

$$a_T^Z = \begin{cases} |(\mathbf{p}_T^a + \mathbf{p}_T^b) \times \hat{t}| & = |\mathbf{p}_T^Z \times \hat{t}| \quad \text{if } \Delta\phi(\mathbf{p}_T^a, \mathbf{p}_T^b) \geq \frac{\pi}{2} \\ |\mathbf{p}_T^a + \mathbf{p}_T^b| & = |\mathbf{p}_T^Z| \quad \text{if } \Delta\phi(\mathbf{p}_T^a, \mathbf{p}_T^b) < \frac{\pi}{2} \end{cases} \tag{7.15}$$

and

$$a_L^Z = (\mathbf{p}_T^a + \mathbf{p}_T^b) \cdot \hat{t} = |\mathbf{p}_T^Z \cdot \hat{t}| \quad . \tag{7.16}$$

The a_T^Z and a_L^Z parameters are believed to be less sensitive to the momentum resolution of a detector and use the angular resolution which can be more sensitive. A toy Monte Carlo study found that a_T^Z and a_L^Z are more sensitive to changes in g_2 when the momentum resolution of the detector is significant, for example, $\Delta(1/p_T) = 0.003$ $(\text{GeV})^{-1}$; however, $|\mathbf{p}_T^Z|$ has a greater sensitivity when the momentum resolution is smaller, i.e. $\Delta(1/p_T) = 0.001$ $(\text{GeV})^{-1}$ [93]. The sensitivity of a_T^Z and a_L^Z in determining g_2 will be compared with p_T^Z in Chapter 8.

7.4 Background subtraction and unfolding

The background shapes defined in Section 7.7 are subtracted from data distributions prior to the unfolding algorithm being used to reconstruct the distribution before detector smearing and acceptance. One iteration of the D'Agostini algorithm is used.

7.5 Uncertainty due to iterative method

The systematic effect induced by the iterative Bayesian method was estimated using 250 pseudo-data samples. Each pseudo-data sample was generated to have approximately the same statistical power as the $\text{Z}^0 \to e^+e^-$ sample after cuts. The smearing matrix was generated using Monte Carlo events with a nominal choice of BLNY parameters and the pseudo-data samples with a different choice. For each pseudo-data sample the reconstructed distribution is unfolded and compared bin-by-bin with the known true distribution. For each bin a relative error is constructed for a specific pseudo-data sample:

$$\Delta_i = \frac{N_i^{\text{test}} - N_i^{\text{nom.}}}{N_i^{\text{nom.}}} \tag{7.17}$$

where N_i^{test} and $N_i^{\text{nom.}}$ are the sum of weights in the ith bin of the histograms for the unfolded pseudo-data sample and nominal true distribution, respectively. Both distributions are normalised to unity.

The mean of all 250 Δ_i is assumed to be the systematic bias in the unfolding technique for each of the distributions of interest. The mean is chosen because the size and sign of Δ_i will fluctuate as a result of the finite statistics in the measured distribution being unfolded, but any leftover effect cannot be a result of statistical fluctuations and is assumed to be a systematic effect induced by the unfolding algorithm. The standard deviation of the 250 Δ_i shifts is taken as the error on each bin induced by the finite statistics of the data sample being unfolded. The mean and standard deviation distributions are shown in Figure 7.2.

7.6 Detector simulation effects

The statistical and systematic error of the unfolding algorithm has been discussed in the previous section. Next the systematic effect of detector effects will be considered.

The control parameters of the fast simulation used to train the unfolding matrix are varied within their error to estimate the corresponding effect on the unfolded distributions. The smearing matrices and a comparison between the true and measured distributions are shown in Figure 7.3 and Figure 7.4.

7.6.1 Calorimeter response

The best fit S_{CEM} and κ_{CEM} are $S_{\text{CEM}} = 1.01202 \pm 0.00009$ and $\kappa_{\text{CEM}} = (0.94 \pm 0.03)\%$. Monte Carlo events were generated for the lower edge and upper edge of these parameters. These events were used to create smearing matrices which were then used to unfold nominal pseudo-data. The standard

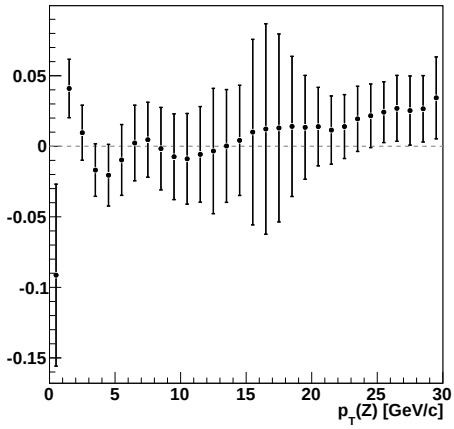

(a) p_T^Z

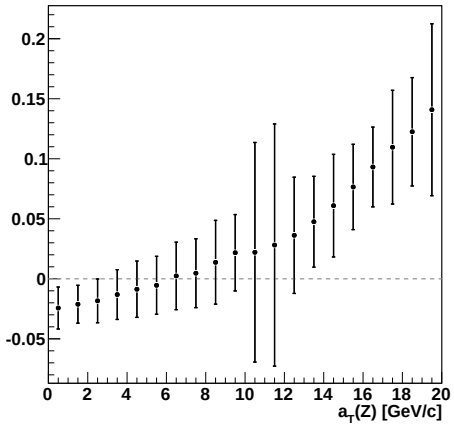

(b) a_T^Z

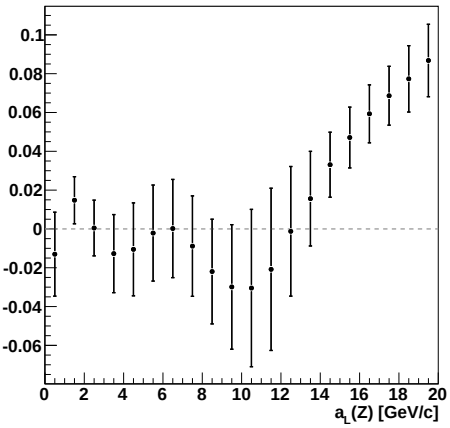

(c) a_L^Z

Figure 7.2: The mean and standard deviation of the shifts in each bin from the unfolding algorithm using 250 pseudo-data samples. Δ_i, the relative shift in the ith bin is estimated for each pseudo-data sample where the mean Δ_i is the systematic error induced by the algorithm in that bin and the standard deviation is the statistical error.

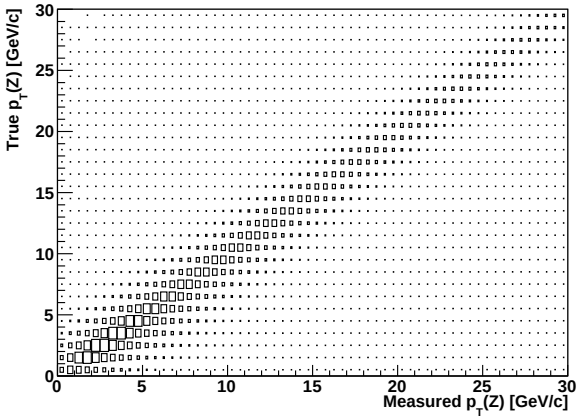

(a) p_T^Z

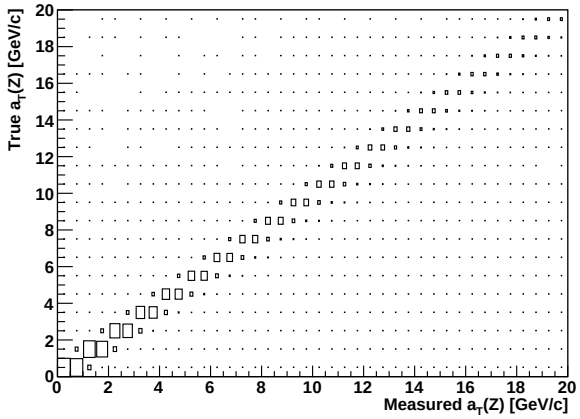

(b) a_T^Z

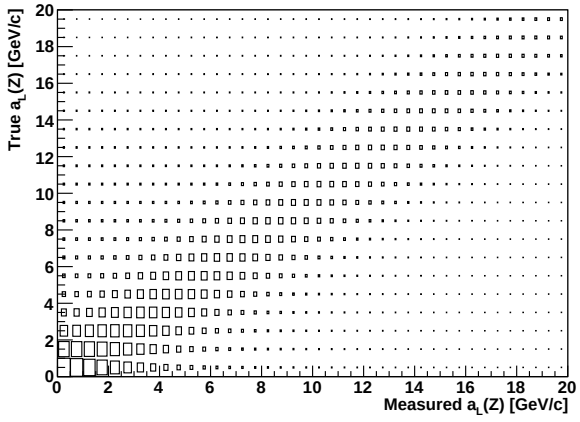

(c) a_L^Z

Figure 7.3: The smearing matrices for (a) p_T^Z, (b) a_T^Z and (c) a_L^Z.

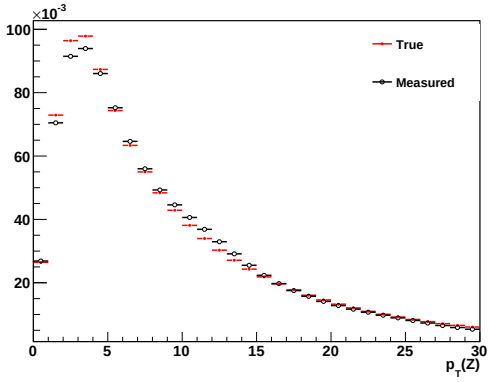

(a) p_T^Z

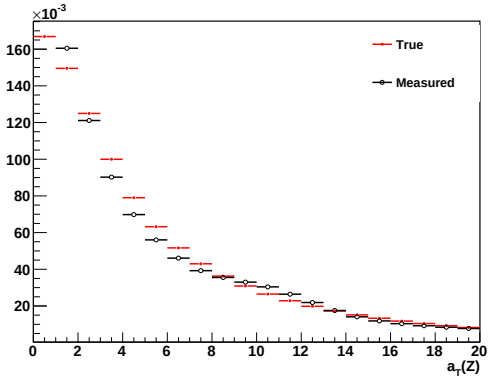

(b) a_T^Z

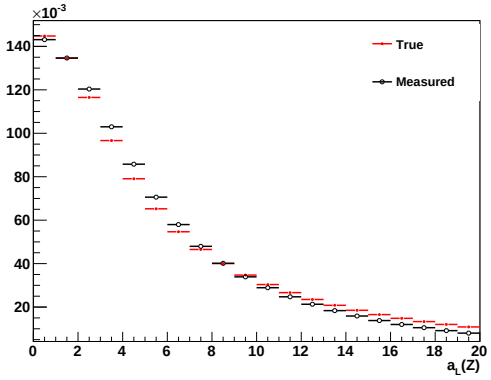

(c) a_L^Z

Figure 7.4: The true distribution of training events compared with the measured or smeared distributions that are reconstructed.

deviation of all the bin deviations, assuming that the mean of the shifts is zero, is assumed to be the systematic uncertainty on the unfolded distribution as a result of S^{CEM} uncertainty. The shifts are shown in Figures 7.5–7.6 with the dashed line representing the systematic uncertainty.

S_{CEM} is assumed to have a systematic uncertainty of 0.11% on the p_T^Z distribution and κ_{CEM} has a 0.12% effect. The a_T^Z distribution has a systematic uncertainty of 0.23% as a result of S_{CEM} uncertainty and 0.20% from κ_{CEM}. The a_L^Z distribution has a systematic uncertainty of 0.07% as a result of S_{CEM} uncertainty and 0.06% from κ_{CEM}.

7.6.2 Material scale

The amount of material encountered by electrons as they pass through the detector is obtained from `SiliMap` [74] previously discussed in Section 5.5.4. This amount of material returned by `SiliMap` controls the probabilities of bremsstrahlung and electron ionisation which results in the upper tail of the E/p distribution. The response of `SiliMap` is scaled so that the Monte Carlo E/p distribution matches data. The scale parameter, S_{Mat}, obtained is 1.042 ± 0.004. Response matrices $S_{\mathrm{Mat}} - \sigma$ and $S_{\mathrm{Mat}} + \sigma$ are generated and nominal smeared Monte Carlo is unfolded. The shifts relative to nominal true Monte Carlo are shown in Figure 7.7.

The systematic contribution of the material scale uncertainty on the unfolded p_T^Z, a_T^Z and a_L^Z distributions are 0.12%, 0.42% and 0.07%, respectively.

7.7 Background processes

An estimated $(0.85 \pm 0.22)\%$ of Z^0 bosons produced at the Tevatron and reconstructed by CDF are from diffractive collisions [94]. In a fraction of inelastic $p\bar{p}$ collisions at least one of the colliding hadrons remains intact in the final

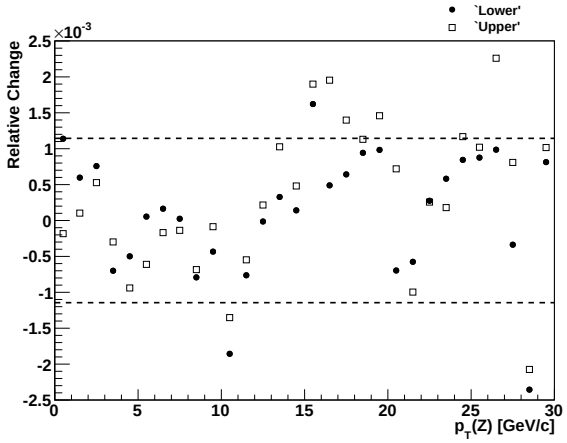

(a) p_T^Z

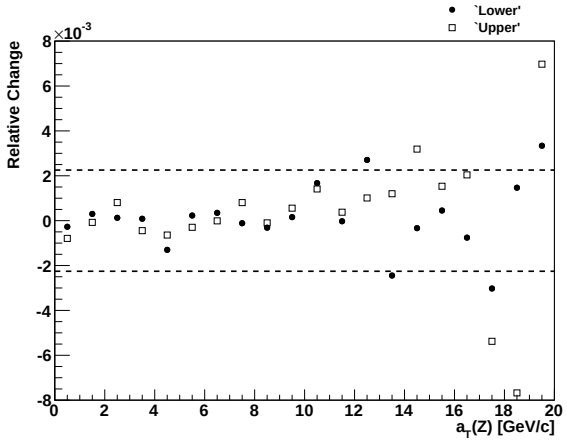

(b) a_T^Z

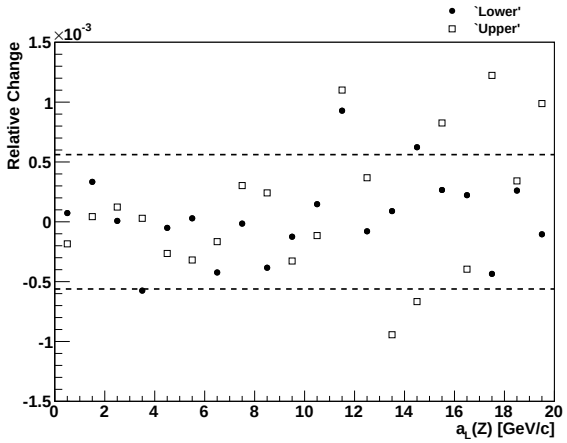

(c) a_L^Z

Figure 7.5: The relative error on an unfolded distribution incurred by adjusting the S_{CEM} parameter by one standard deviation. The standard deviation of the shifts is marked by the dashed line.

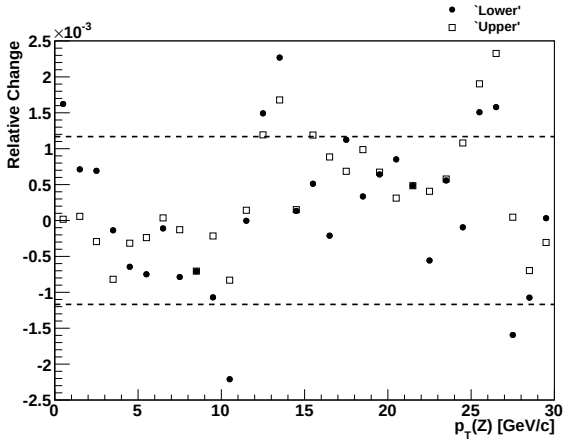

(a) p_T^Z

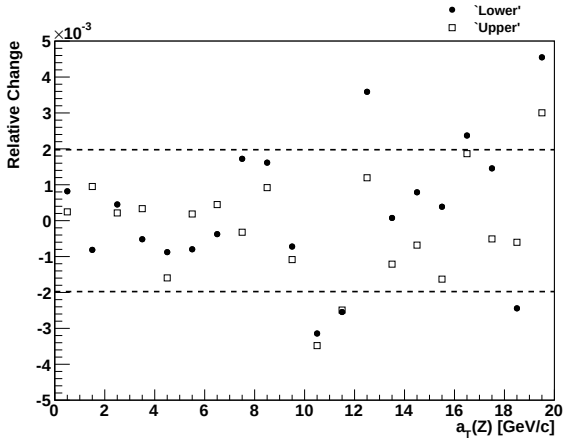

(b) a_T^Z

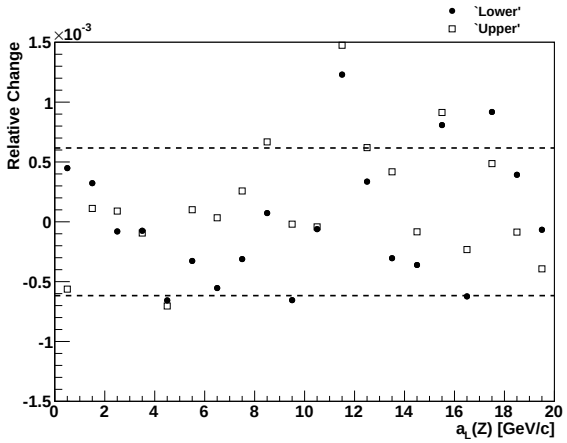

(c) a_L^Z

Figure 7.6: The relative error on an unfolded distribution incurred by adjusting the κ_{CEM} parameter by one standard deviation. The standard deviation of the shifts is marked by the dashed line.

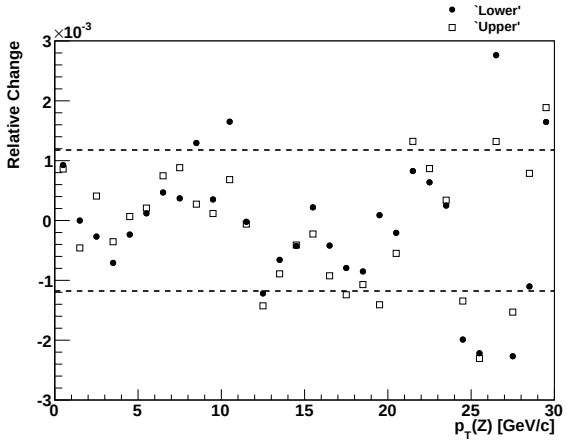

(a) p_T^Z

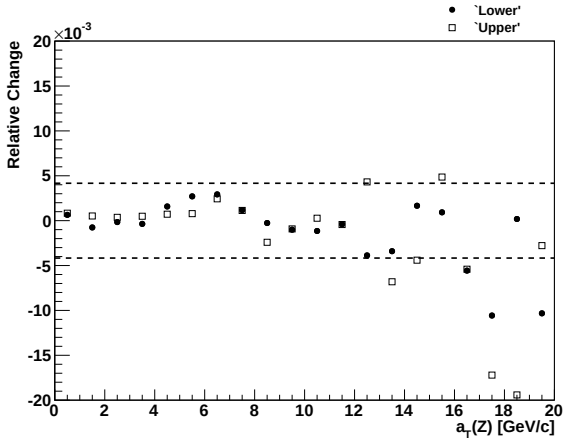

(b) a_T^Z

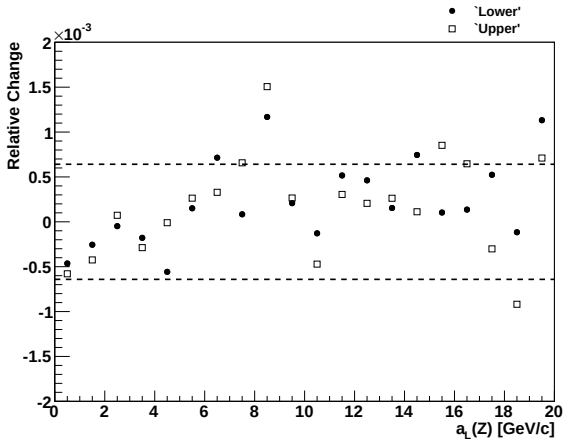

(c) a_L^Z

Figure 7.7: The relative error on an unfolded distribution incurred by adjusting the S_{Mat} parameter by one standard deviation. The standard deviation of the shifts is marked by the dashed line.

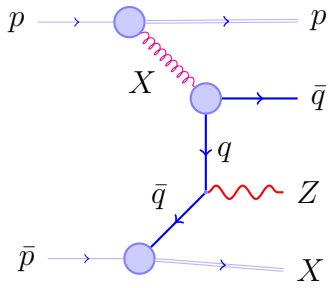

Figure 7.8: The diffractive production of Z^0 bosons. The proton emits an object, X, and remains intact; this object decays into a quark-antiquark pair. The quark (antiquark) from the Pomeron annihilates with an antiquark (quark) from the antiproton.

state. A strongly-interacting colour singlet object is emitted from the proton or antiproton which decays into a quark-antiquark pair which interact with quarks from the other hadron, Figure 7.8. These Z^0s are not modelled by the fast simulation so an estimate of this background is added to fast simulation Monte Carlo prior to fitting to data in Section 6.2.3. It is subtracted from the data before unfolding.

The shape of the diffractive Z^0 background is estimate by fitting to `cdfSim` Monte Carlo events. A Landau distribution is used to describe $|\mathbf{p}_T^Z|$, and exponentials are used to describe a_T^Z and a_L^Z. The parameterisations are presented in Figure 7.9.

A number of electroweak processes can form a background to $Z^0 \rightarrow e^+e^-$ decays where dileptons are misidentified as an electron-positron pair. The acceptance and efficiency of the detector is obtained from `cdfSim` Monte Carlo samples. The number of expected events can be estimated using

$$N_{\text{events}} = \mathcal{L} \cdot \sigma \cdot \epsilon A \cdot BR \tag{7.18}$$

where $\mathcal{L}$ is the integrated luminosity of the corresponding data, σ is the production cross-section for the process, ϵ is the the efficiency of reconstructing an electron-positron pair, A is the detector acceptance, and BR is the branching

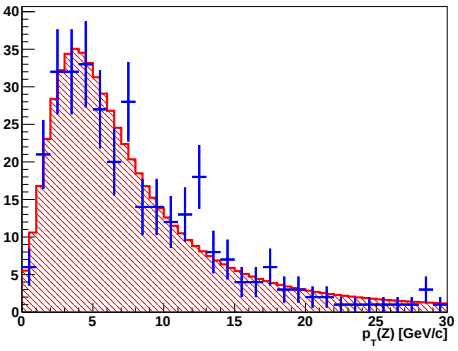

(a) p_T^Z

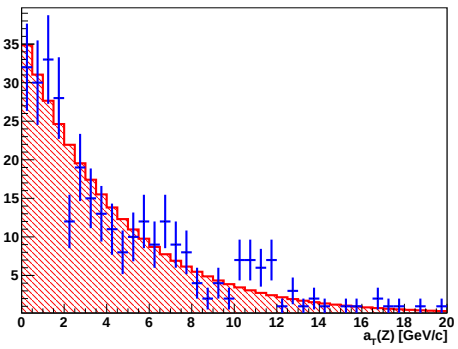

(b) a_T^Z

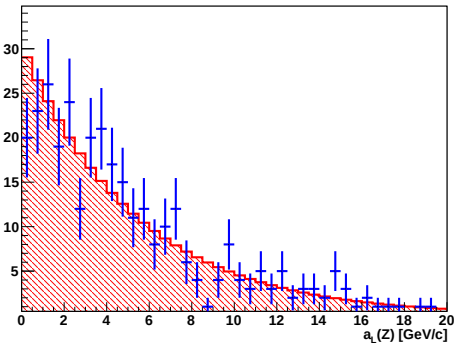

(c) a_L^Z

Figure 7.9: The diffractive Z^0 background from Monte Carlo and fitted parameterisation (shaded area).

ratio for the process into the final state. To obtain a fractional background, $N_{\rm BG}/N_{\rm signal}$, the integrated luminosity is the same; hence

$$\frac{N_{\rm BG}}{N_{\rm signal}} = \frac{\sigma_{\rm BG}}{\sigma_{p\bar{p}\to Z}} \frac{(\epsilon A)_{\rm BG}}{(\epsilon A)_{\rm signal}} \frac{BR_{\rm BG}}{BR_{\rm signal}}. \tag{7.19}$$

The contribution of $Z^0 \to \mu^+\mu^-$, $Z^0 \to \tau^+\tau^-$, $W \to e\nu$, $W \to \mu\nu$, and $W \to \tau\nu$ to the fractional background of $Z^0 \to e^+e^-$ signal is estimated using `cdfSim` Monte Carlo. No significant background is observed.

There are many hadronic processes occurring at CDF as a result of the large cross-section for QCD process compared with weak boson production. QCD events with two back-to-back jets can be misidentified as an electron and pass selection and identification cuts. The size of this background for electron-positron pairs where both leptons are in the central region has been estimated as $(0.24 \pm 0.03)\%$ [95]. The size of this background is approximately the same order as the uncertainty in the diffractive Z^0 background and has the same signal-like shape obtained in Figure 7.9. The background processes are added to give $(1.09 \pm 0.22)\%$ as the total background.

The systematic uncertainty arising from the error in the background fraction is obtained by varying the background fraction by one standard deviation before unfolding the distributions. Figure 7.10 shows the systematic shift in each bin and the dashed line is the standard deviation of the shifts. The shift in each bin is assumed to be the background systematic uncertainty.

7.8 Total systematic uncertainty

Many sources of uncertainty on the unfolded distributions have been discussed. The systematic and statistical uncertainties arising from the unfolding method appear to dominate the uncertainty. Figure 7.11 shows the systematic uncertainty due to the unfolding method as the shift from zero. The statistical

uncertainty of the unfolding method is shown as the first error bar. The contribution of all the other systematic uncertainties are added in quadrature to the statistical uncertainty as shown as the second error bar (Figure 7.12 is the same as Figure 7.11 but the additional systematic contributions are scaled by 10). The statistical error clearly dominates these systematic uncertainties so they are neglected. The results in Chapter 8 will only use the statistical error and the unfolding systematic error added in quadrature.

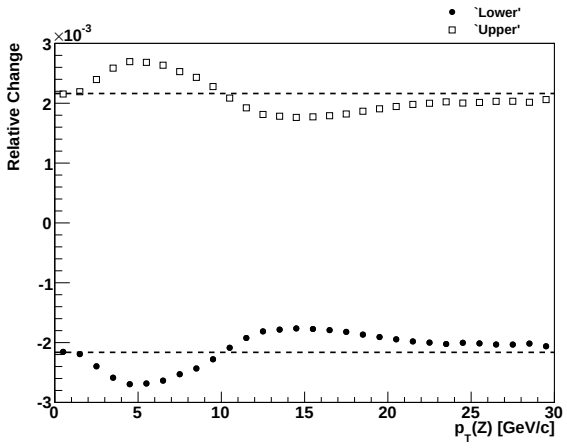

(a) p_T^Z

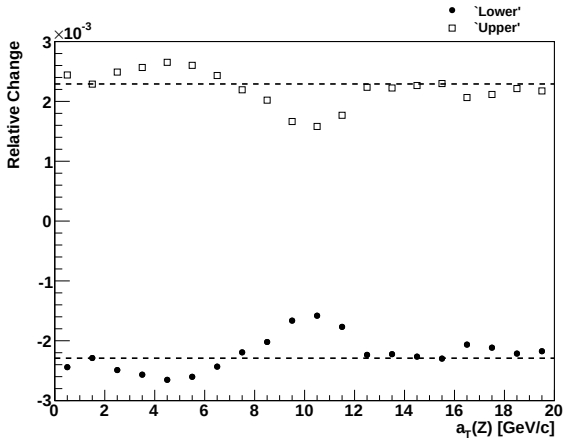

(b) a_T^Z

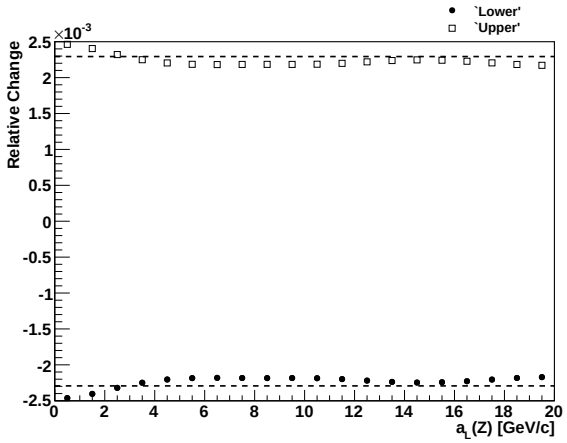

(c) a_L^Z

Figure 7.10: The relative error on an unfolded distributions incurred by adjusting the background fraction by one standard deviation. The standard deviation of the shifts is marked by the dashed line.

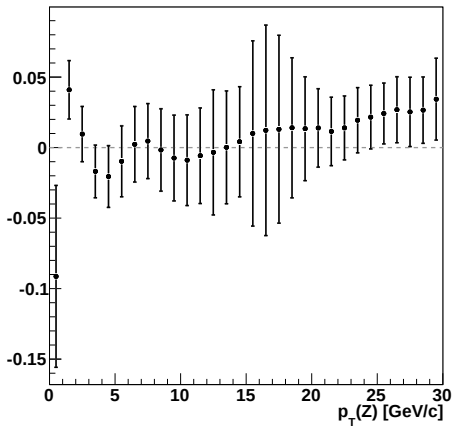

(a) p_T^Z

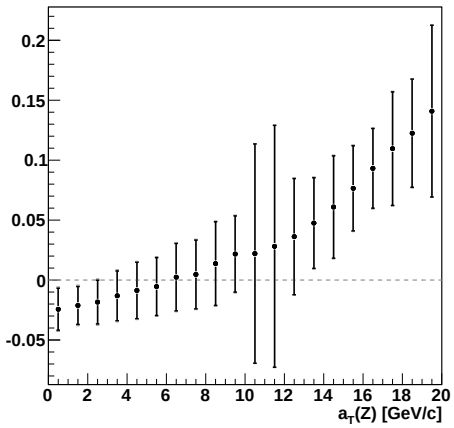

(b) a_T^Z

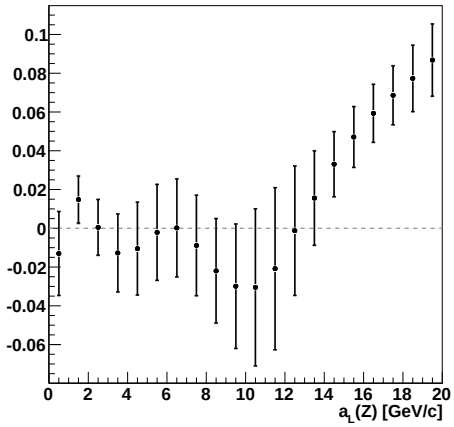

(c) a_L^Z

Figure 7.11: The statistical uncertainty of the unfolding method on the unfolded distributions is shown with the systematic shift of the unfolding method. The additional error bar shows the contribution of the CEM and material scale systematic uncertainties and the background fraction uncertainty added in quadrature (the effect is not large enough to be visible on the plot).

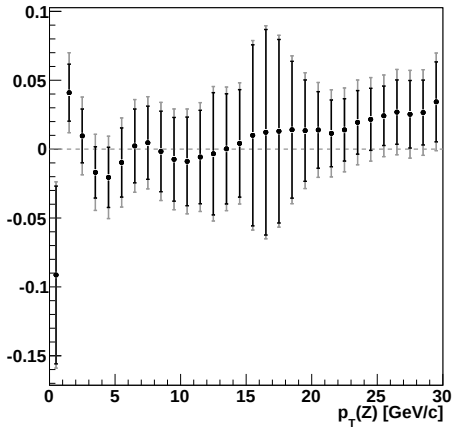

(a) $\langle\Delta\rangle(p_T^Z)$

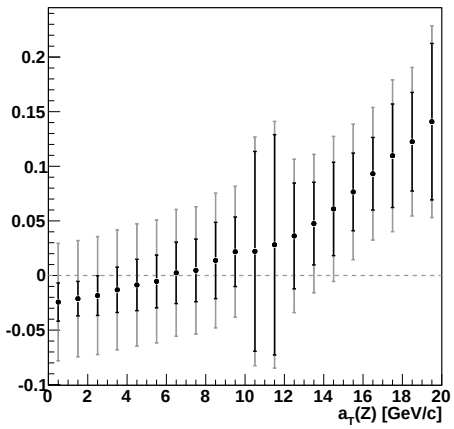

(b) $\langle\Delta\rangle(a_T^Z)$

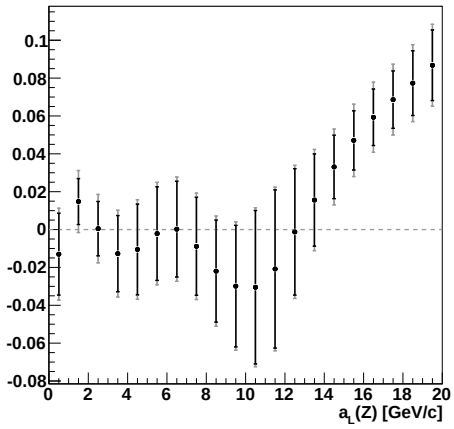

(c) $\langle\Delta\rangle(a_L^Z)$

Figure 7.12: The statistical uncertainty of the unfolding method on the unfolded distributions is shown with the systematic shift of the unfolding method. The additional error bar shows the contribution of the CEM and material scale systematic uncertainties and the background fraction uncertainty all scaled by a factor of 10 and added in quadrature.

Chapter 8

Estimation of the systematic contributions to the W mass

The systematic effects of parton distribution functions and next-to-leading order quantum chromodynamics on the mass of the W boson are presented in the following sections. The determination of the systematic shifts make extensive use of a template fitting approach. Fast simulation Monte Carlo events are produced and templates are created for a range of input M_W values. The change in input M_W is propagated into the templates by re-weighting the events by the change in the Breit-Wigner weight (Section 5.1):

$$\frac{1}{\left(\hat{s} - M_W^2\right)^2 + \Gamma_W^2 M_W^2}. \tag{8.1}$$

The templates are fit against pseudo-data distributions containing the effect being tested and the shift in the fitted M_W from the nominal M_W (80403 MeV) is assumed to be the systematic shift. 40 million Monte Carlo events are used in the templates which implies that the statistical uncertainty is 6 MeV; however, the events in each template are identical such that the extracted shifts are real and not statistical.

8.0.1 Parton density functions

The total symmetric and asymmetric systematic shifts for all the eigenvectors in MSTW2008 NLO and CTEQ6.6 are presented in Tables 8.1 and 8.2, respectively. For comparison with previous M_W analyses, the mass shifts obtained using the older CTEQ6M and CTEQ6.1 PDF error sets are shown in Table 8.3. The shifts are presented visually in Figures 8.1–8.5. Some theoretical assumptions underpinning the CTEQ PDF sets changed between CTEQ6.1 (Figure 8.5) and CTEQ6.6 (Figure 8.3) rendering a direct comparison of the eigenvector shifts impossible. The CTEQ6M and CTEQ6.1 eigenvector shifts are presented for completeness.

A common error for the electron and muon channels is assumed and the larger of the two is taken as the error. The systematics on M_W obtained using M_T^W, p_T^l and $\not\!\!E_T$ fits are: 10 MeV, 9 MeV and 11 MeV using MSTW2008 NLO at 68% confidence interval (C.I.); 22 MeV, 19 MeV and 24 MeV using MSTW2008 NLO at 90% C.I.; and 25 MeV, 22 MeV and 26 MeV using CTEQ6.6 (90% C.I.).

The 1σ systematic shifts on M_W for CTEQ6.6 are estimated by recognising that the global tolerance for CTEQ6.6 using the 68% C.I. limits of the experimental datasets for $T_{68\%}$ does not necessarily equal 6.25[1] if $T_{90\%}$ is 10. This effect is observed in the MSTW 2008 systematic shifts where the 90% C.I. systematic is more than twice as large as the corresponding 68% C.I. systematic ($R(\frac{M90}{M68}) > 2$) when it is expected to be 1.6 . Three procedures to estimate the CTEQ6.6 1σ systematic are used:

(i) scale the CTEQ 90% C.I. error by the corresponding MSTW2008 68% C.I. to MSTW2008 90% C.I. ratio, $R(\frac{M68}{M90})$;

[1]The figure of 6.25 is obtained by taking the value of 10 and dividing it by the expected ratio of 1.6.

(ii) scale the CTEQ 90% C.I. error by the average MSTW2008 68% C.I. to MSTW2008 90% C.I. ratio over all the fit variables for the whole channel, $\langle R(\frac{M68}{M90})\rangle$;

(iii) scale the MSTW2008 68% C.I. error by the average CTEQ 90% C.I. to MSTW2008 90% C.I. ratio over all the fit variables for the whole channel, $\langle R(\frac{C90}{M90})\rangle$.

The largest of these three estimates is taken as the 1σ systematic shift using CTEQ6.6 and is found to be 12 MeV, 10 MeV and 12 MeV for the M_T^W, p_T^l and $\not\!\!E_T$ fits, Table 8.4.

The central values obtained with MSTW2008 NLO and CTEQ6.6 differ by 8 MeV in the electron channel and 4 MeV in the muon channel for the M_T^W fit, both within the uncertainty arising from the MSTW (10 MeV) and CTEQ (12 MeV) error-sets.

The eigenvectors inducing the largest shifts in M_W in the MSTW2008 NLO set, Figures 8.1 and 8.2, are those numbered 7, 10, 12 and 14. These eigenvectors are largely dominated by uncertainties in the valence down quark distribution, d_v (eigenvectors 7, 10 and 14) and the $\bar{d}-\bar{u}$ distributions (eigenvector 12). Future improvements in the understanding of lepton and W charge asymmetry may improve this systematic in the future but difficulties in obtaining consistent fits to recent Tevatron asymmetry data may hamper efforts to further constrain the d_v uncertainty [96].

MSTW have also produced NNLO versions of the MSTW2008 PDF sets. The shifts in M_W obtained by re-weighting the best-fit NLO pseudo-data with the best-fit NNLO are shown in Table 8.5. The systematic uncertainties are 6.0 MeV, 4.5 MeV and 6.5 MeV for the M_T^W, p_T^l and $\not\!\!E_T$ fits, respectively. This is an incomplete study because NNLO Monte Carlo generators should also be used

Process	Fit	68% C.I.	90% C.I.	$R\left(\frac{M90}{M68}\right)$
$W \to e\nu$	M_T^W	10.2 +9.4 −12.4	21.9 +18.6 −29.1	2.15 1.98 2.34
	p_T^e	8.9 +8.3 −10.9	19.3 +16.4 −25.5	2.17 1.98 2.34
	$\not{E}_T$	11.2 +10.4 −13.5	24.1 +20.6 −31.9	2.15 1.98 2.36
$W \to \mu\nu$	M_T^W	10.0 +9.2 −12.2	21.5 +18.2 −28.7	2.15 1.98 2.35
	p_T^μ	8.6 +7.9 −10.4	18.4 +15.6 −24.4	2.14 1.97 2.35
	$\not{E}_T$	11.0 +10.2 −13.4	23.8 +20.3 −31.5	2.16 1.99 2.35

Table 8.1: The symmetric and asymmetric systematic shifts in M_W for all the eigenvectors for MSTW2008 NLO PDFs. The ratios, $R(\frac{M90}{M68})$, of the 90% C.I. error to the 68% C.I. error are shown.

Process	Fit	CTEQ6.6	MSTW 90%	$R\left(\frac{C90}{M90}\right)$
$W \to e\nu$	M_T^W	24.7 +23.0 −28.3	21.9 +18.6 −29.1	1.13 1.24 0.97
	p_T^e	21.5 +20.0 −24.8	19.3 +16.4 −25.5	1.11 1.22 0.97
	$\not{E}_T$	25.8 +23.9 −29.6	24.1 +20.6 −31.9	1.07 1.16 0.93
$W \to \mu\nu$	M_T^W	24.1 +22.4 −27.9	21.5 +18.2 −28.7	1.12 1.23 0.97
	p_T^e	20.3 +18.9 −23.5	18.4 +15.6 −24.4	1.10 1.21 0.96
	$\not{E}_T$	26.3 +24.5 −30.1	23.8 +20.3 −31.5	1.11 1.21 0.96

Table 8.2: The symmetric and asymmetric systematic shifts in M_W for all the eigenvectors in CTEQ6.6 PDFs. MSTW2008 NLO at 90% C.I. is shown for comparison.

Process	Fit	CTEQ6M	CTEQ6.1	CTEQ6.6
W $\to e\nu$	M_T^W	$24.8^{+31.9}_{-23.0}$	$24.8^{+31.9}_{-23.0}$	$24.7^{+23.0}_{-28.3}$
	p_T^e	$21.4^{+27.5}_{-19.8}$	$21.5^{+27.5}_{-19.8}$	$21.4^{+20.0}_{-24.8}$
	$\not\!\!E_T$	$26.3^{+33.0}_{-24.6}$	$26.3^{+33.4}_{-24.6}$	$25.8^{+23.9}_{-29.6}$
W $\to \mu\nu$	M_T^W	$23.4^{+30.6}_{-21.0}$	$23.8^{+30.9}_{-21.9}$	$24.1^{+22.4}_{-27.9}$
	p_T^e	$19.4^{+25.2}_{-17.6}$	$19.7^{+25.6}_{-18.0}$	$20.3^{+18.9}_{-23.5}$
	$\not\!\!E_T$	$25.9^{+33.6}_{-23.4}$	$26.9^{+34.6}_{-24.9}$	$26.3^{+24.5}_{-30.1}$

Table 8.3: The symmetric and asymmetric systematic shifts in M_W for all the eigenvectors in CTEQ6M, CTEQ6.1 and CTEQ6.6 PDFs.

Process	Fit	$R(\frac{M68}{M90})$	$\langle R(\frac{M68}{M90})\rangle$	$\langle R(\frac{C90}{M90})\rangle$	(i)	(ii)	(iii)
W $\to e\nu$	M_T^W	2.15^{-1}	2.16^{-1}	1.10	11.5	11.5	11.3
	p_T^e	2.17^{-1}			9.9	10.0	9.9
	$\not\!\!E_T$	2.15^{-1}			12.0	12.0	12.4
W $\to \mu\nu$	M_T^W	2.15^{-1}	2.15^{-1}	1.11	11.2	11.2	11.1
	p_T^μ	2.14^{-1}			9.5	9.4	9.6
	$\not\!\!E_T$	2.16^{-1}			12.3	12.3	12.3

Table 8.4: The specific values used to estimate the 1σ systematic shift in M_W for CTEQ6.6 PDFs. The three estimates are denoted as (i), (ii) and (iii) and show the result in MeV of $\Delta M_W^{\mathrm{C90}} \cdot R(\frac{M68}{M90})$, $\Delta M_W^{\mathrm{C90}} \cdot \langle R(\frac{\mathrm{M68}}{\mathrm{M90}})\rangle$ and $\Delta M_W^{\mathrm{M68}} \cdot \langle R(\frac{\mathrm{C90}}{\mathrm{M90}s})\rangle$, respectively. The largest of (i), (ii) or (iii) is chosen as the 1σ systematic for that leptonic process and fit.

Process	Fit	ΔM_W
$W \to e\nu$	M_T^W	6.1
	p_T^e	4.8
	$\not{E}_T$	6.4
$W \to \mu\nu$	M_T^W	6.0
	p_T^μ	4.3
	$\not{E}_T$	6.6

Table 8.5: The systematic shifts in MeV incurred by re-weighting pseudo-data events generated using the best-fit MSTW2008 NLO with MSTW2008 NNLO.

to include the effect of the NNLO QCD matrix element calculation. NNLO corrections to weak boson production [97] have been available for a number of years, and there are calculations that predict experimental observables such as the rapidity of Z^0 bosons at NNLO [98] but these calculations have not been resummed in the the low-p_T^W region.

While the effect of NNLO matrix element calculations and the correlation with NNLO PDF sets has not been explicitly determined in this analysis, there are expected to be cancellations which imply that the systematic error obtained by replacing a NLO PDF set with a NNLO PDF set may be an overestimate.

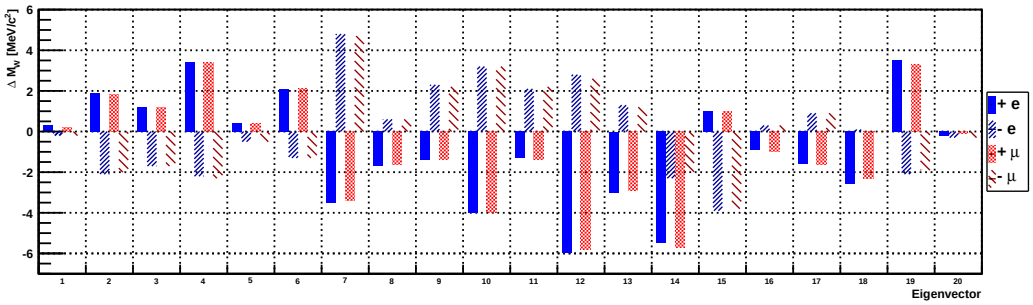

(a) M_T^W fit

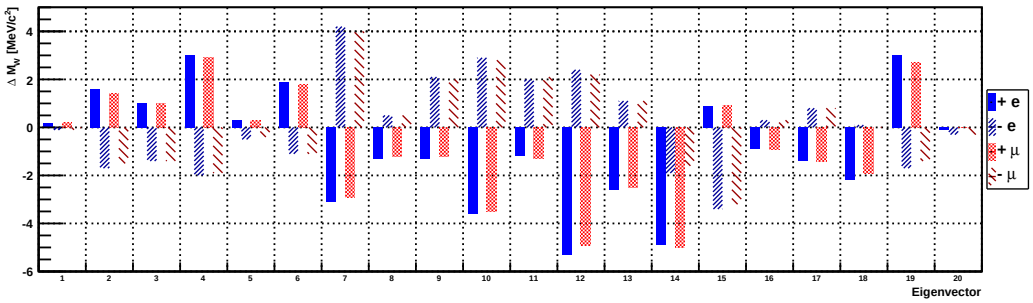

(b) p_T^{lep} fit

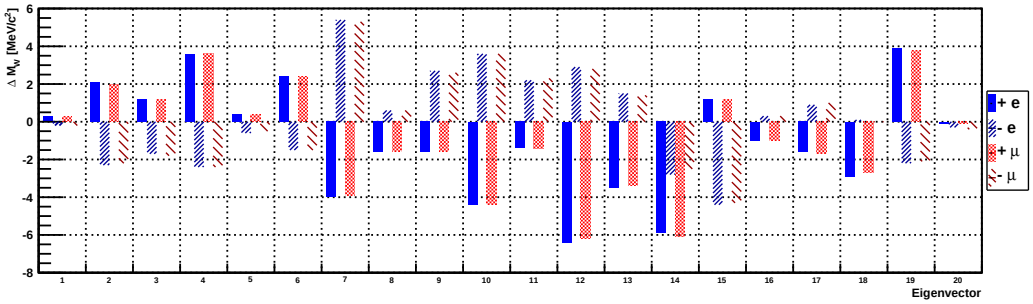

(c) $\not{E}_T$ fit

Figure 8.1: The observed shift for M_W in MeV by fitting Monte Carlo pseudo-data against templates generated with the nominal PDF set using the 68% confidence interval MSTW 2008 NLO set. The observed shift in the electron and muon channels is shown for the S_k^+ and S_k^- for each eigenvector, k.

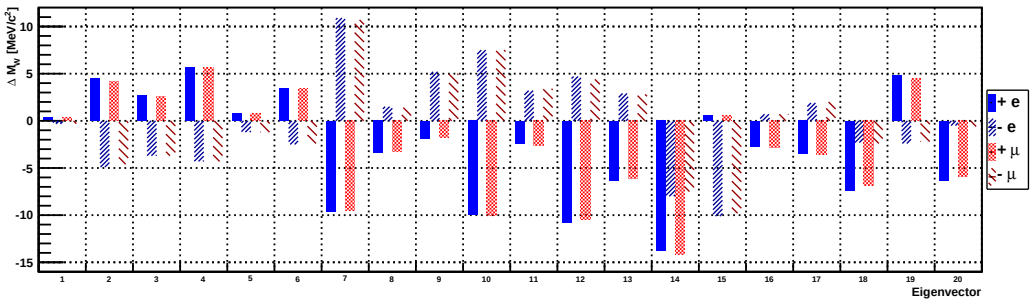

(a) M_T^W fit

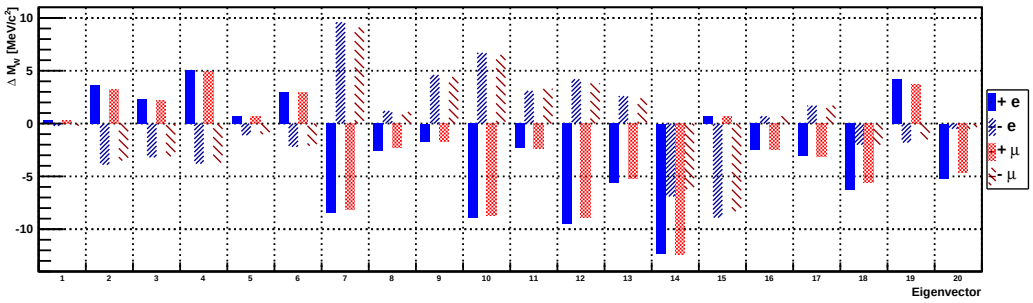

(b) p_T^{lep} fit

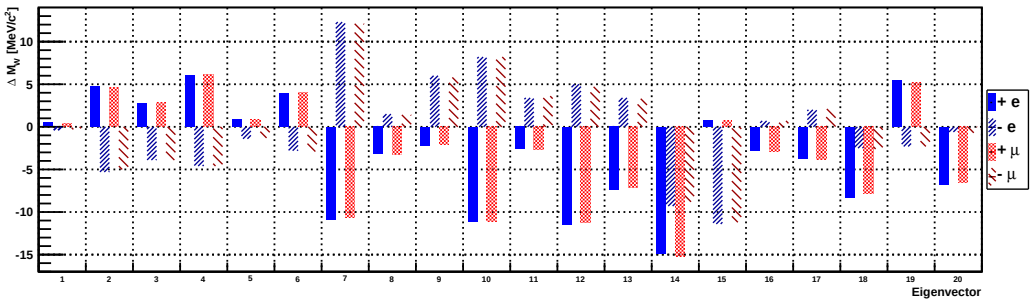

(c) $\not\!\!E_T$ fit

Figure 8.2: The observed shift for M_W in MeV by fitting Monte Carlo pseudo-data against templates generated with the nominal PDF set using the 90% confidence interval MSTW 2008 NLO set. The observed shift in the electron and muon channels is shown for the S_k^+ and S_k^- for each eigenvector, k.

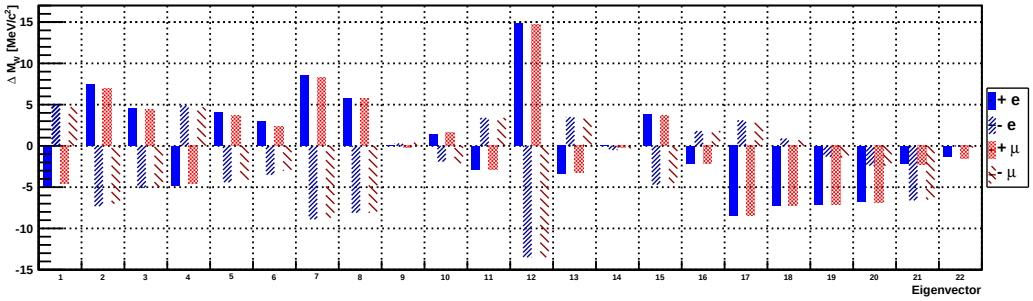

(a) M_T^W fit

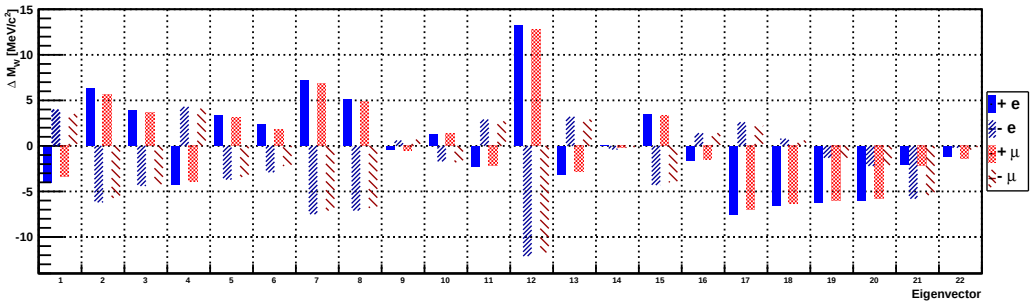

(b) p_T^{lep} fit

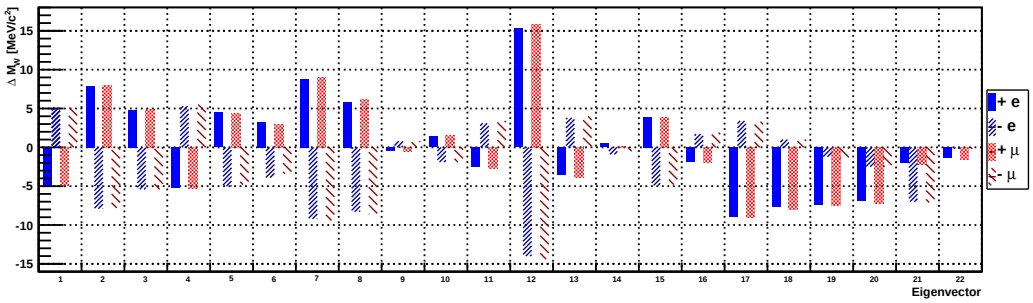

(c) $\not\!\!E_T$ fit

Figure 8.3: The observed shift for M_W in MeV by fitting Monte Carlo pseudo-data against templates generated with the nominal PDF set using the CTEQ6.6 set. The observed shift in the electron and muon channels is shown for the S_k^+ and S_k^- for each eigenvector, k.

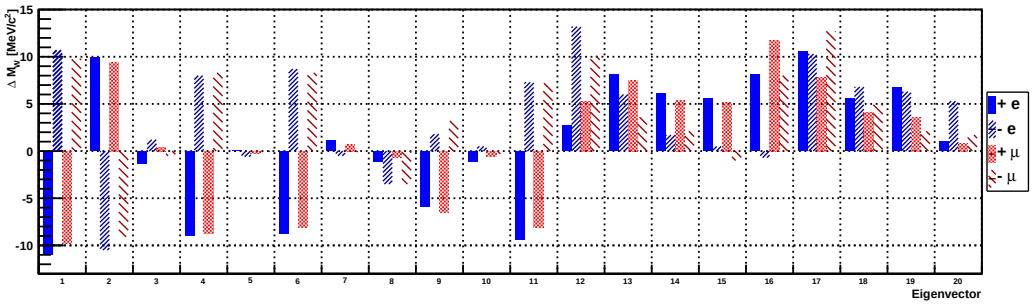

(a) M_T^W fit

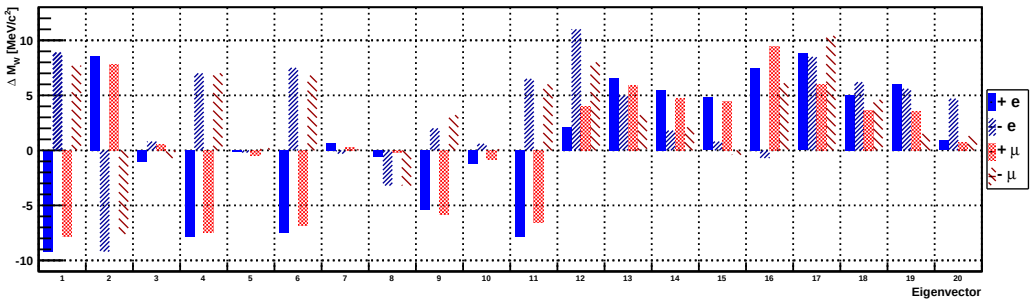

(b) p_T^{lep} fit

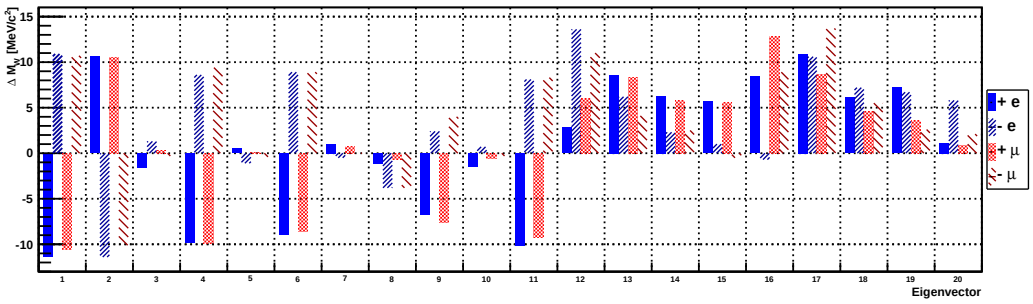

(c) $\not\!\!E_T$ fit

Figure 8.4: The observed shift for M_W in MeV by fitting Monte Carlo pseudo-data against templates generated with the nominal PDF set using the CTEQ6M set. The observed shift in the electron and muon channels is shown for the S_k^+ and S_k^- for each eigenvector, k.

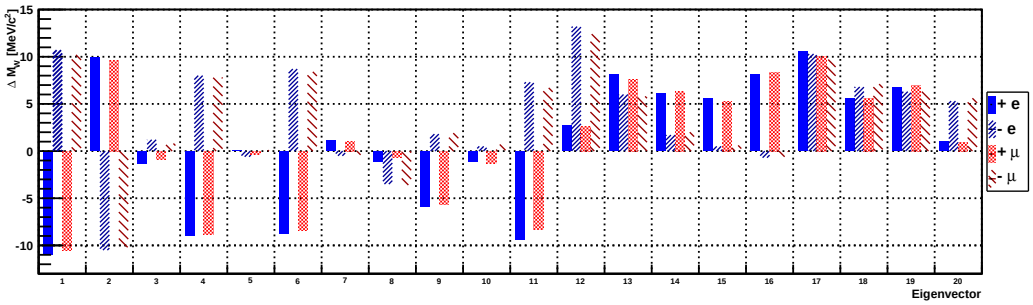

(a) M_T^W fit

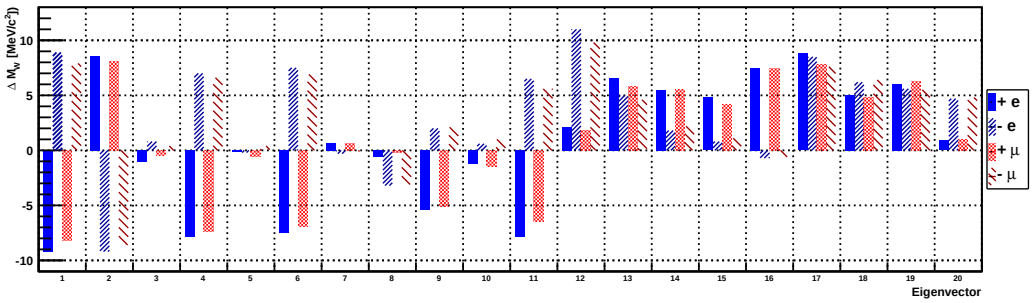

(b) p_T^{lep} fit

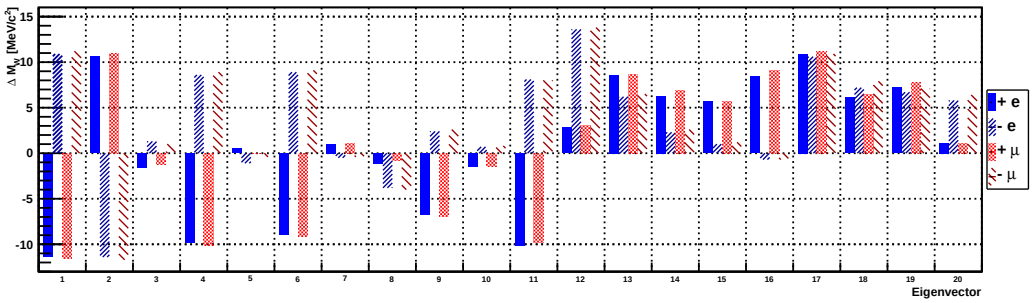

(c) $\not\!\!E_T$ fit

Figure 8.5: The observed shift for M_W in MeV by fitting Monte Carlo pseudo-data against templates generated with the nominal PDF set using the CTEQ6.1 set. The observed shift in the electron and muon channels is shown for the S_k^+ and S_k^- for each eigenvector, k.

8.0.2 W polarisation and angular distribution

The effect of the uncertainty in the A_i coefficients is used to estimate the systematic error in the modelling of the W angular distribution. The error bands obtained in [88] for A_1–A_3 and A_5–A_7 are used. Each A_i function is replaced in the fast simulation by $A_i + 20\sigma_{A_i}$ and $A_i - 20\sigma_{A_i}$ and each event is re-weighted by the change using Equation (5.16). Each reweighted pseudo-data sample is fit with nominal templates and the respective shifts taken as the systematic effect for that coefficient. None of the tested coefficients induced a 20σ shift greater than 5 MeV in either of the M_T^W, p_T^l or $\not\!\!E_T$ fits. Uncertainties in A_1–A_3 and A_5–A_7 functions are therefore assumed to have a negligible systematic contribution.

The systematic effect of the A_0 and A_4 uncertainty is estimated by re-weighting Monte Carlo events to match the $\cos\theta$ distributions obtained from `RESBOS` [60]. The shift in the fitted M_W incurred is taken as the systematic error as a result of tuning the $|\mathbf{p}_T^W|$ evolution of the A_0 and A_4 functions. Identical shifts in both the electron and muon channels of 3 MeV, 1 MeV and 4 MeV for the M_T^W, p_T^e and $\not\!\!E_T$ fits, respectively, are obtained.

8.0.3 W transverse momentum

The fit to both $Z^0 \to e^+e^-$ and $Z^0 \to \mu^+\mu^-$ decays give $g_2 = 0.721 \pm 0.018$ GeV^2 and $\xi = 0.117 \pm 0.001$ with a combined χ^2/ndf of 139.3/116, and is shown in Figure 8.6. The correlation between the two parameters, ρ, is -0.71. The sub-fit χ^2/ndf are 75.1/58 and 64.2/58 for $Z^0 \to e^+e^-$ and $Z^0 \to \mu^+\mu^-$ data, respectively. As cross-checks, constraining the fit parameters using only $Z^0 \to e^+e^-$ data gives $g_2 = 0.729 \pm 0.042$ GeV^2 and $\xi = 0.117 \pm 0.001$ with a χ^2 fit to $Z^0 \to e^+e^-$ ($Z^0 \to \mu^+\mu^-$) data of 74.8/57 (65.3/57). Constraining

the fit parameters using only $Z^0 \to \mu^+\mu^-$ data gives $g_2 = 0.718 \pm 0.027$ GeV^2 and $\xi = 0.117 \pm 0.001$ with a χ^2 fit to $Z^0 \to \mu^+\mu^-(Z^0 \to e^+e^-)$ data of 64.1/57 (75.4/57). The agreement between the central values of these cross-checks and the similar χ^2 values of the best fits indicate that the electron and muon g_2 and ξ are compatible; therefore, a single g_2-ξ pair describes the electron and muon channels simultaneously.

The effect of fixing ξ to the PDF set value of $\alpha_s(M_Z)$ is shown in Figure 8.7. The fit to both $Z^0 \to e^+e^-$ and $Z^0 \to \mu^+\mu^-$ data with ξ fixed gives $g_2 = 0.623 \pm 0.013$ GeV^2 with a combined χ^2/ndf of 180.1/117. The smaller g_2 uncertainty indicated that fixing ξ does not allow enough flexibility to describe the uncertainty in the Z^0 data: changes in g_2 do not affect the perturbative QCD calculation and have a reduced effect in the tail of the distribution where perturbative QCD dominates the resummed contribtion. This demonstrates the g_2-ξ correlation where a higher value of ξ forces a lower value of g_2. The best description of the data is obtained using $\xi = 0.117$ which is consistent with the world average $\alpha_s(M_Z) = 0.1184 \pm 0.0007$ [99] but lower than the nominal value of the PDF set.

To estimate the systematic uncertainty on M_W arising from the uncertainty in g_2 and ξ, Equation (8.2) is used to re-weight Monte Carlo events. Each of the free parameters in the p_T^Z fit is perturbed by 1σ in turn and the change in the p_T shape is applied as a corrective weight. The change in the shape of the rapidity re-weighting functions, Equations (5.13) and (5.14), induced by the shift in g_2 and ξ is also applied as a corrective weight:

$$w = \frac{\frac{d\sigma}{dp_T}(g_2 = g_2^0 \pm \Delta g_2, \xi = \xi_0 + \Delta\xi)}{\frac{d\sigma}{dp_T}(g_2 = g_2^0, \xi = \xi_0)}. \tag{8.2}$$

The distributions of re-weighted events are fit using nominal templates and the change in the fitted M_W is taken as the systematic shift for that parameter. Since $\not\!\!E_T$ is determined from p_T^l and U where U is parameterised in terms of p_T^W, the $\not\!\!E_T$ distribution is affected by the true p_T^W and the recoil model. In order to ascertain only the sensitivity to the underlying p_T^W, the transverse momentum of the neutrino in the generator before smearing effects is used as a fit variable, p_T^ν. The ratio of true charged lepton transverse momentum, $(p_T^l)_t$, and measured charged lepton transverse momentum, p_T^l, is used to estimate $\not\!\!E_T$ without the effect of the recoil where $\not\!\!E_T^{\rm nr} = p_T^\nu \cdot p_T^l/(p_T)_t$. The values obtained are shown in Table 8.6. The shifts for the two parameters are combined according to

$$\Delta M_W(g_2\text{-}\xi) = \sqrt{\left(\Delta M_W(g_2)\right)^2 + \left(\Delta M_W^2(\xi)\right)^2 + \rho \Delta M_W(g_2)\Delta M_W(\xi)} \quad (8.3)$$

in the electron channel giving ΔM_W of 4.9 MeV, 5.8 MeV and 6.4 MeV for the M_T^W, p_T^e and $\not\!\!E_T^{\rm nr}$ fits, respectively. The systematics in the muon channel are 4.7 MeV, 5.6 MeV and 7.0 MeV. In the following it is assumed that the electron and muon systematic uncertainties are the same.

The effect corresponding to the uncertainty in g_1 and g_3 is estimated using the BLNY fit uncertainties, Table 5.1, using the same method as used to estimate the effect of g_2 and ξ. Adding the shifts for g_1 and g_3 in quadrature[2], the 1σ systematics are 2.5 MeV, 2.7 MeV and 3.2 MeV for the M_T^W, p_T^l and $\not\!\!E_T^{\rm nr}$ fits, respectively.

The electron and muon channel g_2-ξ errors are combined and the g_1 and g_3 errors are added in quadrature. This gives a final systematic of 5.4 MeV,

[2]The g_1 and g_3 parameters are correlated in the BLNY global fit but no correlation coefficient is presented in the paper. A previous global fit presents g_1-g_2, g_1-g_3 and g_2-g_3 ellipses which reveals that g_1 and g_3 are anti-correlated so the g_1-g_3 systematic is likely an overestimate [69].

Process	Fit	$(g_2 - \Delta g_2)$	$(g_2 + \Delta g_2)$	$(\xi - \Delta\xi)$	$(\xi + \Delta\xi)$
$W \to e\nu$	M_T^W	−5.2	5.2	−2.9	3.0
	p_T^e	−5.8	5.7	−4.3	4.4
	$(p_T^e)_t$	−5.9	5.9	−4.2	4.3
	p_T^ν	−6.5	6.4	−4.6	4.6
	$\not\!\!E_T^{\rm nr}$	−6.3	6.2	−4.7	4.8
	$\not\!\!E_T$	−14.1	13.9	−8.1	8.6
$W \to \mu\nu$	M_T^W	−5.0	4.9	−2.6	2.7
	p_T^μ	−5.7	5.6	−4.3	4.4
	$(p_T^\mu)_t$	−5.8	5.8	−4.3	4.3
	p_T^ν	−7.1	7.0	−5.2	5.3
	$\not\!\!E_T^{\rm nr}$	−6.9	6.8	−5.3	5.3
	$\not\!\!E_T$	−13.4	13.2	−7.7	7.8

Table 8.6: The values of M_W in MeV obtained using the different input g_2 and ξ. The shifts are obtained by fitting nominal fast simulation Monte Carlo to pseudo-data generated with the tested parameter perturbed by one standard deviation of the error obtained in the Z^0 fit.

6.4 MeV and 7.6 MeV for the M_T^W, p_T^l and $\not\!\!E_T^{\rm nr}$ fits as a result of the finite Z^0 statistics (and BLNY data) used to tune the p_T^Z and p_T^W distributions.

8.1 True Z^0 distributions

The determination of g_2 in the previous section used a smearing matrix to produce measured distributions which were compared with data. The following section will use the unfolded data to extract g_2 using truth distributions. If the unfolding is robust then the extracted values of g_2 should agree. In addition, the a_T^Z and a_L^Z distributions will be used to compare the sensitivity of each in determining g_2 with the p_T^Z distribution.

The unfolded p_T^Z, a_T^Z and a_L^Z distributions are presented in Tables 8.7–8.8 and the training data are shown in Figure 7.4. The statistical and systematic errors arising from the unfolding method for each bin have been added in quadrature.

The fast simulation is used to produce generator-level events with the

p_T^Z	$\frac{1}{\sigma}\frac{d\sigma}{dp_T^Z}$	p_T^Z	$\frac{1}{\sigma}\frac{d\sigma}{dp_T^Z}$	p_T^Z	$\frac{1}{\sigma}\frac{d\sigma}{dp_T^Z}$
0.5	(0.027 ± 0.003)	10.5	(0.038 ± 0.001)	20.5	(0.013 ± 0.001)
1.5	(0.073 ± 0.003)	11.5	(0.034 ± 0.001)	21.5	(0.012 ± 0.001)
2.5	(0.096 ± 0.003)	12.5	(0.031 ± 0.001)	22.5	(0.011 ± 0.001)
3.5	(0.097 ± 0.003)	13.5	(0.027 ± 0.001)	23.5	(0.010 ± 0.001)
4.5	(0.087 ± 0.003)	14.5	(0.024 ± 0.001)	24.5	(0.009 ± 0.001)
5.5	(0.075 ± 0.002)	15.5	(0.021 ± 0.002)	25.5	(0.008 ± 0.001)
6.5	(0.065 ± 0.002)	16.5	(0.019 ± 0.001)	26.5	(0.008 ± 0.001)
7.5	(0.056 ± 0.002)	17.5	(0.017 ± 0.001)	27.5	(0.007 ± 0.001)
8.5	(0.049 ± 0.002)	18.5	(0.016 ± 0.001)	28.5	(0.007 ± 0.001)
9.5	(0.043 ± 0.001)	19.5	(0.014 ± 0.001)	29.5	(0.006 ± 0.001)

Table 8.7: The unfolded p_T^Z distribution after subtracting background and using one iteration of the unfolding algorithm.

a_T^Z	$\frac{1}{\sigma}\frac{d\sigma}{da_T^Z}$	a_T^Z	$\frac{1}{\sigma}\frac{d\sigma}{da_T^Z}$
0.5	(0.165 ± 0.005)	10.5	(0.028 ± 0.003)
1.5	(0.149 ± 0.004)	11.5	(0.024 ± 0.003)
2.5	(0.120 ± 0.004)	12.5	(0.020 ± 0.001)
3.5	(0.099 ± 0.003)	13.5	(0.017 ± 0.001)
4.5	(0.078 ± 0.002)	14.5	(0.015 ± 0.001)
5.5	(0.063 ± 0.002)	15.5	(0.013 ± 0.001)
6.5	(0.053 ± 0.002)	16.5	(0.012 ± 0.001)
7.5	(0.045 ± 0.002)	17.5	(0.011 ± 0.001)
8.5	(0.036 ± 0.001)	18.5	(0.009 ± 0.001)
9.5	(0.033 ± 0.001)	19.5	(0.008 ± 0.001)

Table 8.8: The unfolded a_T^Z distribution after subtracting background and using one iteration of the unfolding algorithm.

a_L^Z	$\frac{1}{\sigma}\frac{d\sigma}{da_L^Z}$	a_L^Z	$\frac{1}{\sigma}\frac{d\sigma}{da_L^Z}$
0.5	(0.144 ± 0.004)	10.5	(0.031 ± 0.002)
1.5	(0.134 ± 0.004)	11.5	(0.027 ± 0.002)
2.5	(0.116 ± 0.003)	12.5	(0.024 ± 0.001)
3.5	(0.096 ± 0.003)	13.5	(0.021 ± 0.001)
4.5	(0.079 ± 0.002)	14.5	(0.019 ± 0.001)
5.5	(0.066 ± 0.002)	15.5	(0.017 ± 0.001)
6.5	(0.055 ± 0.002)	16.5	(0.015 ± 0.001)
7.5	(0.047 ± 0.001)	17.5	(0.013 ± 0.001)
8.5	(0.040 ± 0.001)	18.5	(0.012 ± 0.001)
9.5	(0.035 ± 0.002)	19.5	(0.011 ± 0.001)

Table 8.9: The unfolded a_L^Z distribution after subtracting background and using one iteration of the unfolding algorithm.

BLNY global best fit parameters and $g_2 = 0.66$ GeV^2. These events are re-weighted to produce template distributions for a 0.60–0.80 GeV^2 range in g_2 with a 0.02 GeV^2 step size and ξ fixed to 0.117. A χ^2-test is used to determine the goodness-of-fit for each generator-level distribution to the unfolded $Z^0 \to e^+e^-$ data. A quadratic fit to the χ^2 scan was used to estimate the best fit value of g_2. This is repeated for the a_T^Z and a_L^Z distributions.

The χ^2 scans and closest g_2 templates are presented in Figures 8.8–8.10. The best fit g_2 values are 0.733 ± 0.038 GeV^2, 0.715 ± 0.071 GeV^2 and 0.684 ± 0.073 GeV^2 for the p_T^Z, a_T^Z and a_L^Z distributions, respectively. The p_T^Z distribution is more sensitive to changes in g_2 than the a_T^Z and a_L^Z distributions. This is not unexpected considering the results of the toy study in [93] where p_T^Z was shown to have a greater sensitivity for $\Delta(1/p_T) \sim 0.001$ (GeV)$^{-1}$ which is the case for CDF.

Recently the BLNY phenomenological model has been adjusted by Konychev and Nadolsky (KN) to improve its description of low $\hat{s}$ data and the authors have performed a new global fit including the low-energy data [100]. The new model is:

$$\widetilde{W}_{NK}^{NP}(b) = \exp\left(-a_1 - a_2 \ln\left(\frac{Q}{2Q_0}\right) - a_3 \ln\left(100 \cdot x_1 x_2\right)\right) b^2 \qquad (8.4)$$

which is similar to BLNY only this parameterisation removes the explicit correlation between g_1 and g_3. The new best fit is $a_1 = 0.201 \pm 0.011$ GeV^2, $a_2 = 0.184 \pm 0.018$ GeV^2 and $a_3 = -0.026 \pm 0.007$ GeV^2.

Fast Monte Carlo templates are generated over the same 0.60–0.80 GeV^2 range in $g_2 \equiv a_2$ as before. ξ is fixed to the value determined by the PDF set but the new values of g_1 and a_3 in the KN global fit are used. The results are presented in Figures 8.11–8.13 and the best-fit g_2 obtained are 0.699 ± 0.035

GeV^2, 0.696 ± 0.066 GeV^2 and 0.684 ± 0.068 GeV^2 for the p_T^Z, a_T^Z and a_L^Z fits respectively.

Interestingly, the value of g_2 does not agree with the KN global fit but it has already been shown that the sensitivity of p_T^Z to changes in g_1 and $g_1 g_3 \equiv a_3$ at the Tevatron is low; therefore, it is not unexpected that the g_2 consistent with previous Tevatron g_2 measurements is returned [40, 54, 69, 101].

To gauge the performance of the fast simulation with the NLO QCD corrections with other generators available, `PYTHIA` 8.14 Monte Carlo events are compared with the unfolded $Z^0 \to e^+e^-$ data in Figure 8.14. The inability of the default `PYTHIA` configuration to describe the transverse momentum distribution coupled with the slower execution time supports the use of a bespoke generator and detector simulation where higher-order effects can be controlled and studied with more ease.

There have been efforts to improve the p_T^Z description of Monte Carlo generators for the Large Hadron Collider but these have been predominantly been at high-p_T [102].

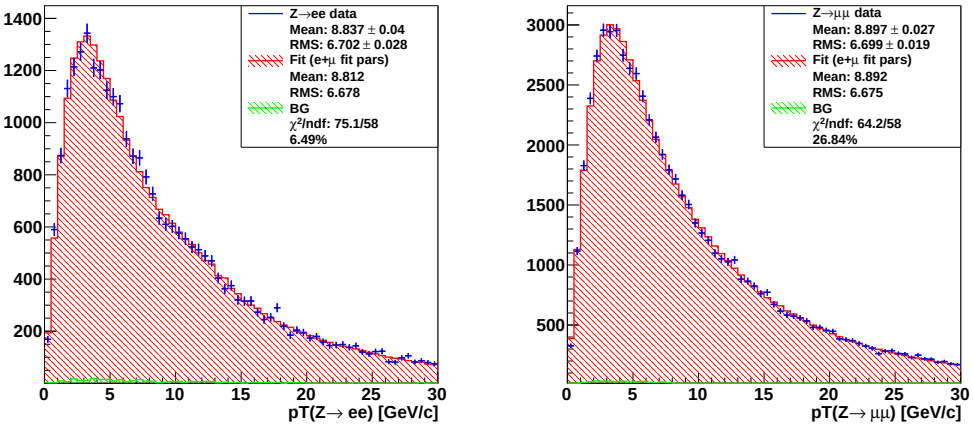

(a) $Z^0 \to e^+e^-$ (b) $Z^0 \to \mu^+\mu^-$

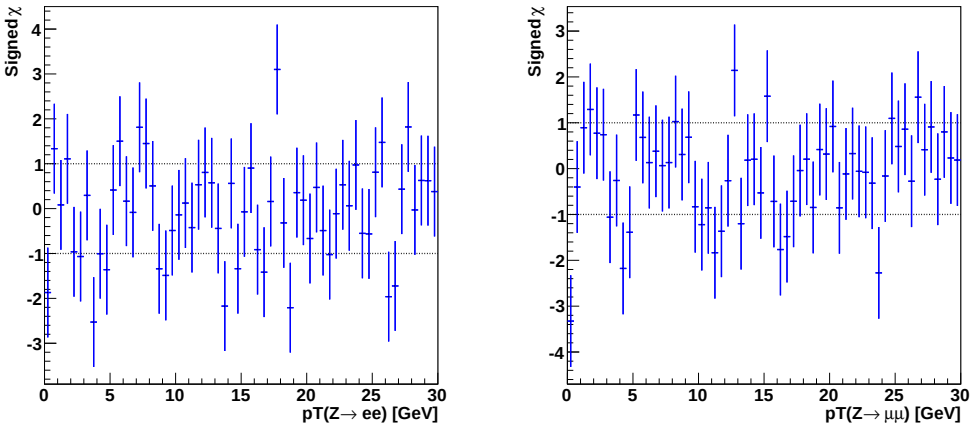

(c) $Z^0 \to e^+e^-$ (d) $Z^0 \to \mu^+\mu^-$

Figure 8.6: The best fit Monte Carlo p_T^Z distribution compared against (a) $Z^0 \to e^+e^-$ and (b) $Z^0 \to \mu^+\mu^-$ data using $g_2 = 0.721$ GeV^2 and $\xi = 0.1167$. The signed χ distributions are also shown for (c) $Z^0 \to e^+e^-$ and (d) $Z^0 \to \mu^+\mu^-$.

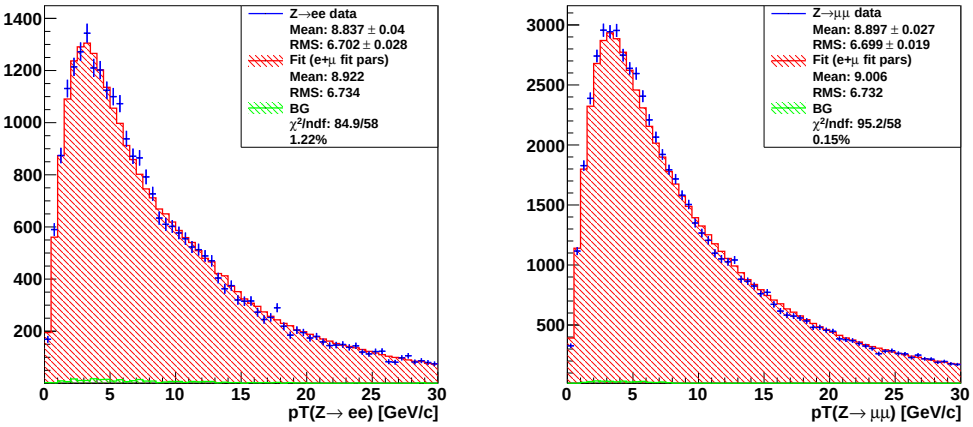

(a) $Z^0 \to e^+e^-$ (b) $Z^0 \to \mu^+\mu^-$

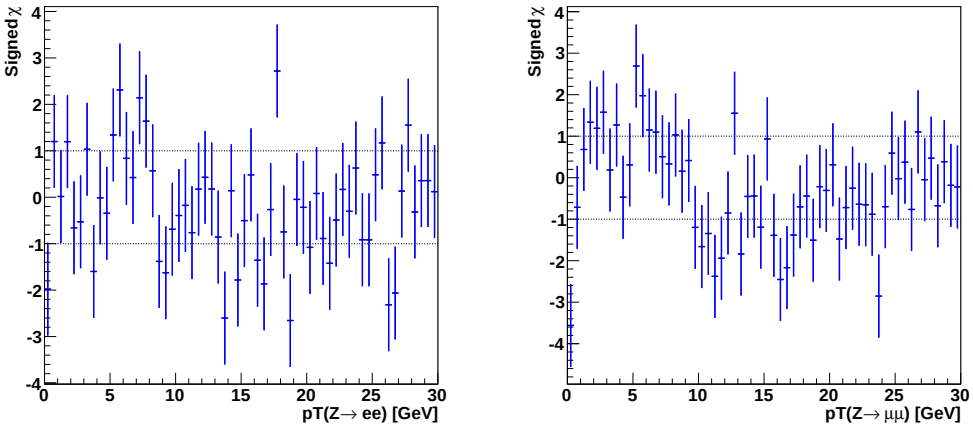

(c) $Z^0 \to e^+e^-$ (d) $Z^0 \to \mu^+\mu^-$

Figure 8.7: The best fit Monte Carlo p_T^Z distribution compared against (a) $Z^0 \to e^+e^-$ and (b) $Z^0 \to \mu^+\mu^-$ data using $g_2 = 0.623$ GeV^2 and with ξ fixed at 0.1201 (PDF set value). The signed χ distributions are also shown for (c) $Z^0 \to e^+e^-$ and (d) $Z^0 \to \mu^+\mu^-$.

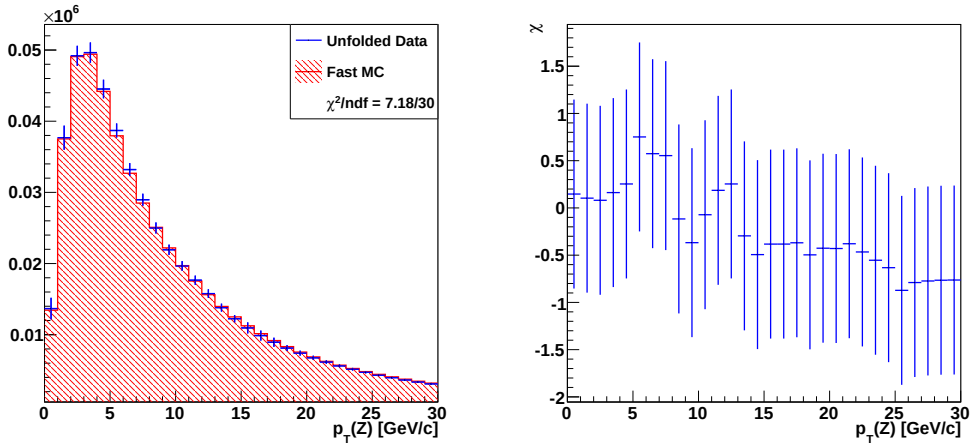

(a) p_T^Z (b) Signed χ

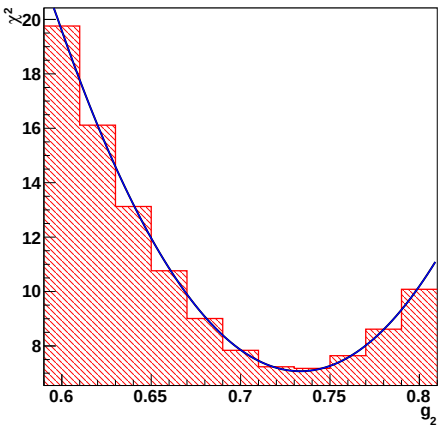

(c) g_2 χ^2 scan

Figure 8.8: The best χ^2 fit between the background subtracted and unfolded $Z^0 \rightarrow e^+e^-$ data and g_2-reweighted fast Monte Carlo for the p_T^Z distribution. One iteration of the unfolding algorithm has been used to unfold the data.

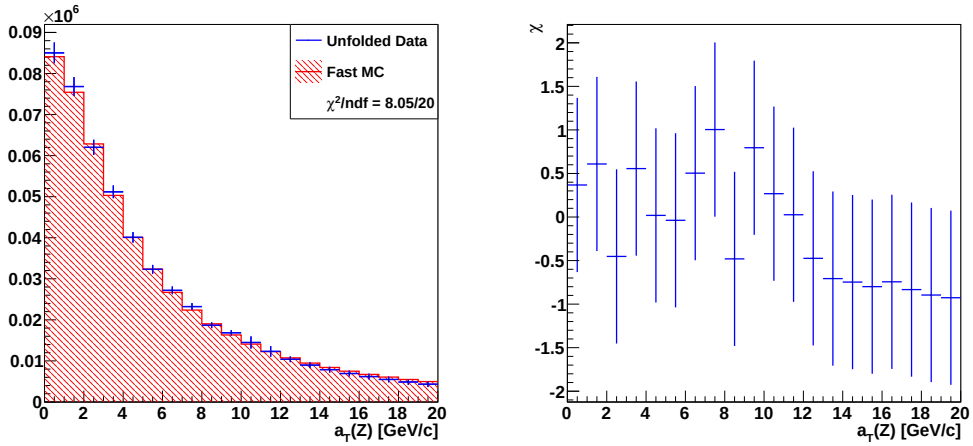

(a) a_T^Z (b) Signed χ

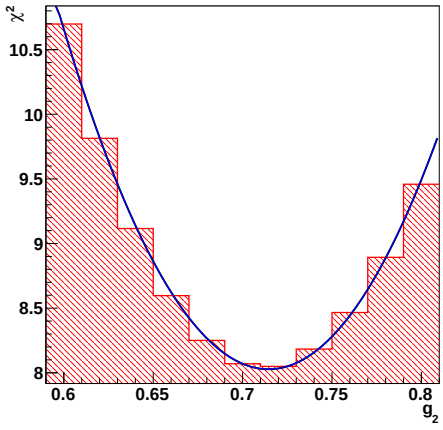

(c) g_2 χ^2 scan

Figure 8.9: The best χ^2 fit between the background subtracted and unfolded $Z^0 \rightarrow e^+e^-$ data and g_2-reweighted fast Monte Carlo for the a_T^Z distribution. One iteration of the unfolding algorithm has been used to unfold the data.

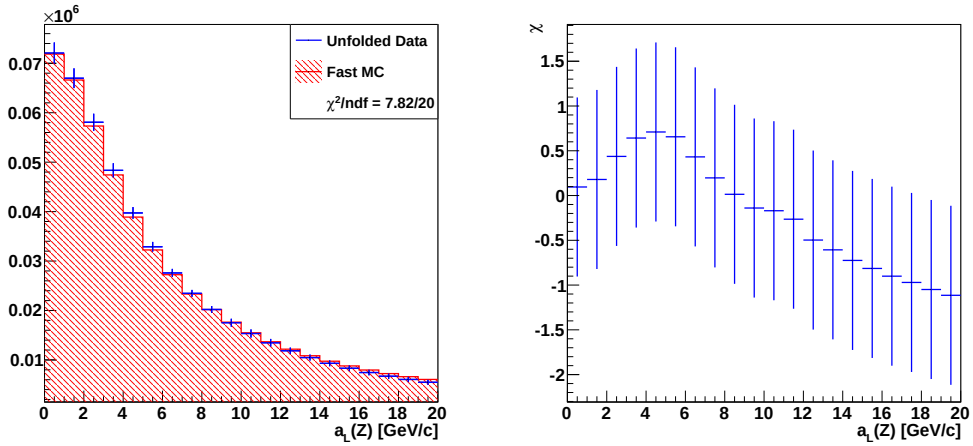

(a) a_L^Z (b) Signed χ

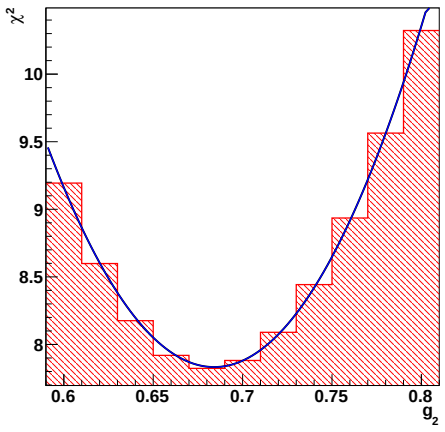

(c) g_2 χ^2 scan

Figure 8.10: The best χ^2 fit between the background subtracted and unfolded $Z^0 \rightarrow e^+e^-$ data and g_2-reweighted fast Monte Carlo for the a_L^Z distribution. One iteration of the unfolding algorithm has been used to unfold the data.

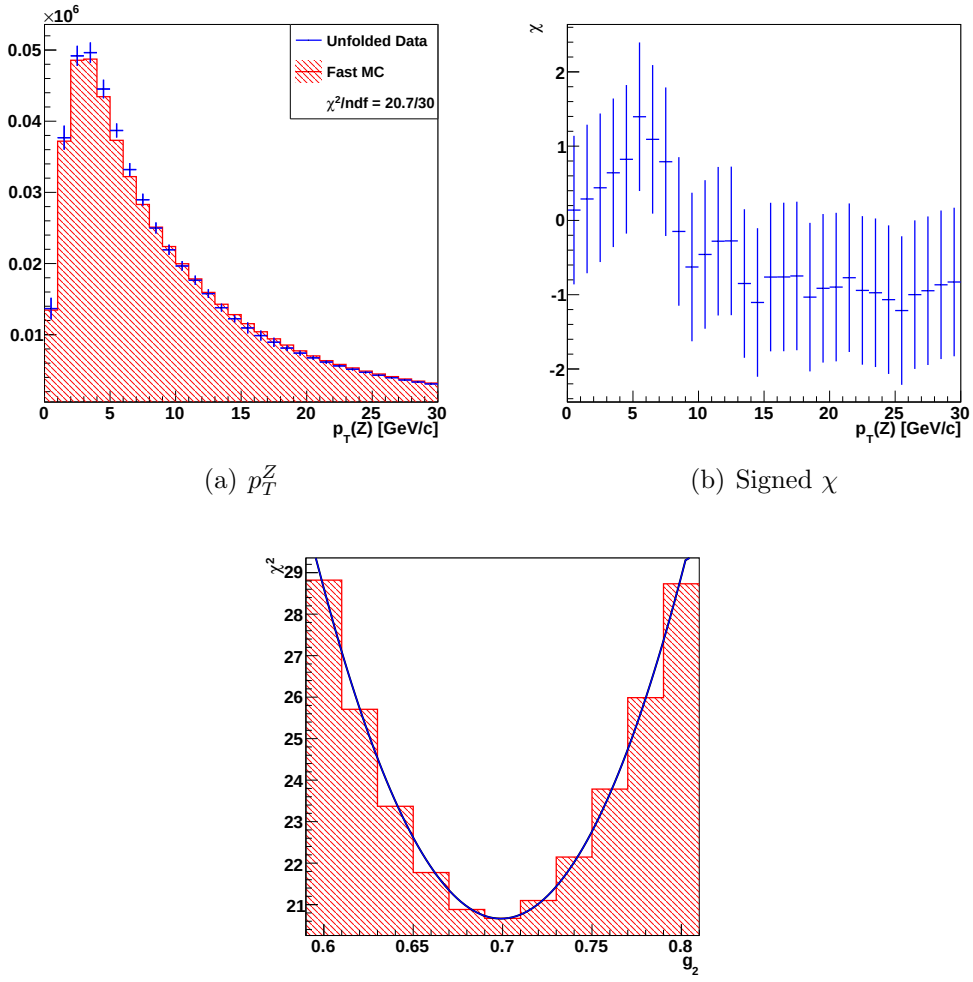

(a) p_T^Z

(b) Signed χ

(c) g_2 χ^2 scan

Figure 8.11: The best χ^2 fit between the background subtracted and unfolded $Z^0 \rightarrow e^+e^-$ data and a g_2-reweighted fast Monte Carlo p_T^Z distribution using the KN global fit parameters for g_1 and g_3. One iteration of the unfolding algorithm has been used to unfold the data.

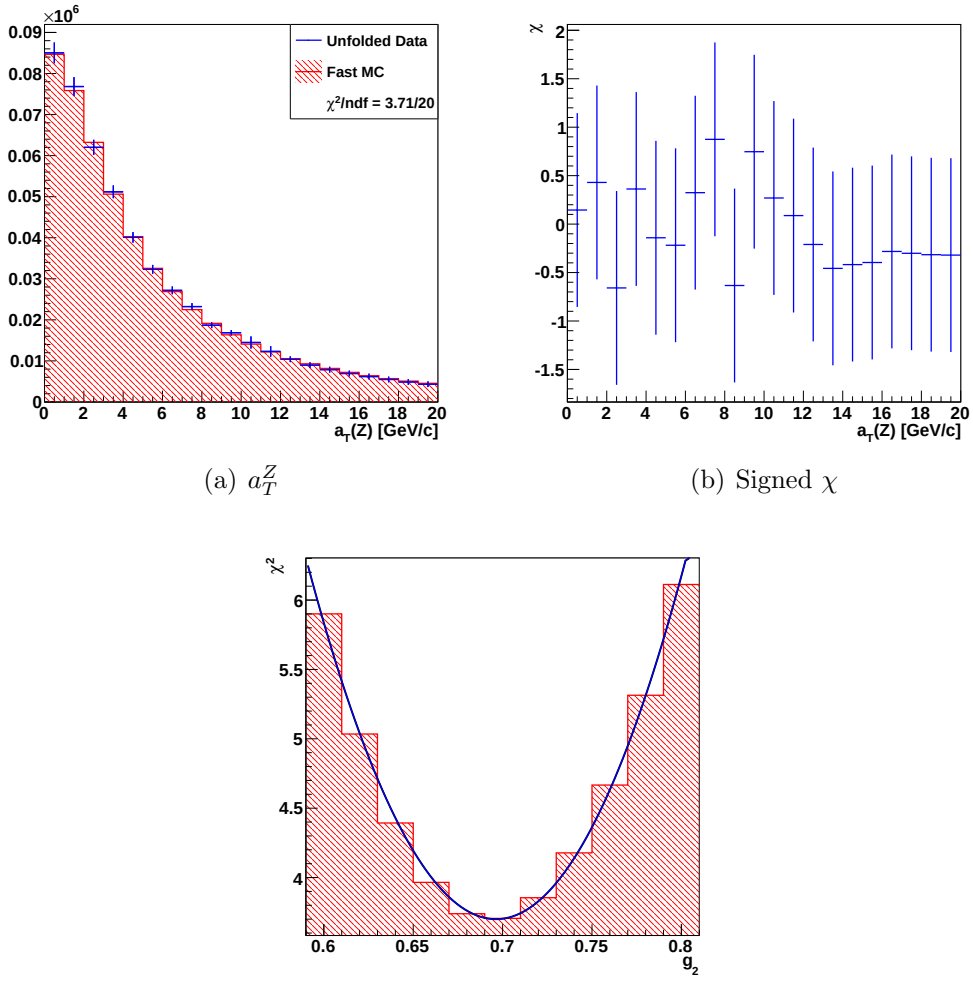

(a) a_T^Z

(b) Signed χ

(c) g_2 χ^2 scan

Figure 8.12: The best χ^2 fit between the background subtracted and unfolded $Z^0 \rightarrow e^+e^-$ data and a g_2-reweighted fast Monte Carlo a_T^Z distribution using the KN global fit parameters for g_1 and g_3. One iteration of the unfolding algorithm has been used to unfold the data.

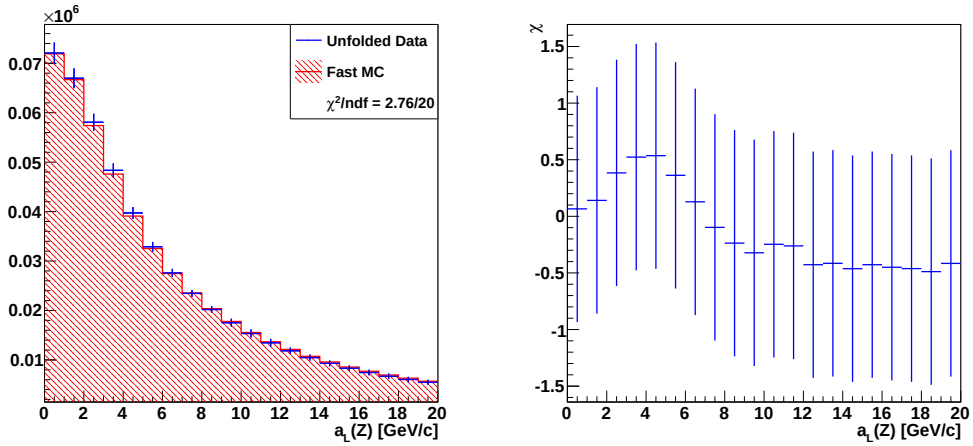

(a) a_L^Z (b) Signed χ

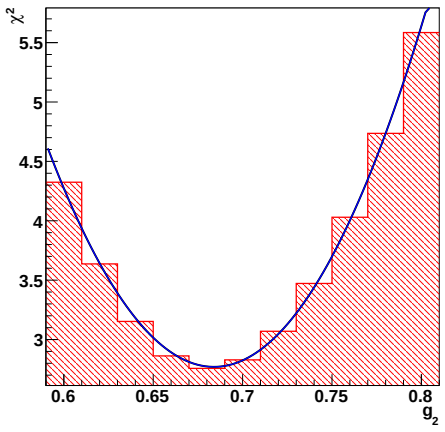

(c) g_2 χ^2 scan

Figure 8.13: The best χ^2 fit between the background subtracted and unfolded $Z^0 \rightarrow e^+e^-$ data and a g_2-reweighted fast Monte Carlo a_L^Z distribution using the KN global fit parameters for g_1 and g_3. One iteration of the unfolding algorithm has been used to unfold the data.

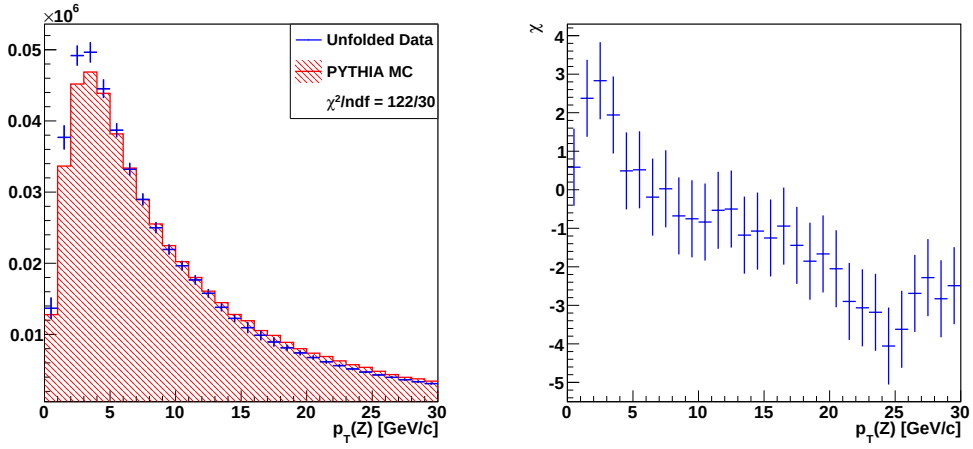

(a) (b)

Figure 8.14: Default PYTHIA 8.14 compared with unfolded $Z^0 \rightarrow e^+e^-$ data. No detector smearing or acceptance effects have been simulated.

Chapter 9

Conclusions

The mass of the W boson remains important as an input in determining the mass of the as of yet unobserved Higgs boson; therefore, reducing the uncertainty of the W mass helps to further constrain the standard model prediction of the Higgs. The standard model prediction of M_W is 80379 MeV [50], whereas the current world average mass is 80399 ± 23 MeV [4]. While the world average and fitted masses only differ by a standard deviation, the current fits indicate a slight tension between the standard model and the mass obtained by direct measurement. This can be seen in Figure 9.1 where the direct measurement of the W mass is more massive than the standard model prediction. In addition, a heavier M_W suggests a lighter Higgs boson. The combination of M_W results at the Tevatron by CDF and DØ is 80420 ± 31 MeV [82] and is even more massive than the world average; therefore, reducing the uncertainty while maintaining a similar central value may pull the world average mass higher. In turn, this would lower the upper bound on the standard model Higgs mass toward the LEP exclusion region. This future scenario may be speculative but it would imply that the standard model does not agree with data. It is hoped that this can be achieved with a reduced M_W uncertainty expected from the next W mass measurement at CDF and subsequent combinations.

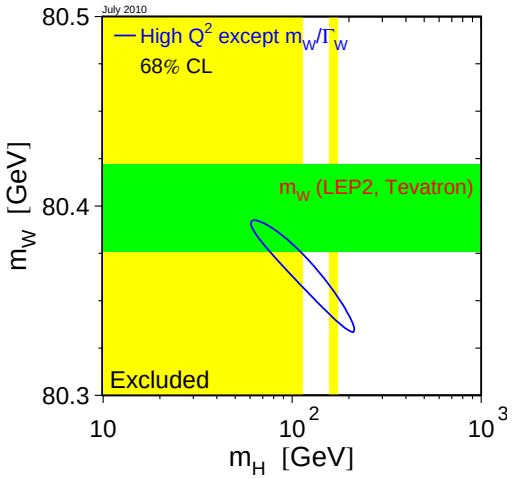

Figure 9.1: The standard model Higgs prediction contour from the recent LEP and Tevatron Electroweak Working group results [49, 50]. The contour is the 68% confidence interval excluding W mass data, where the horizontal shaded area represents direct measurements of M_W and one standard deviation error. Vertical shaded regions of the plot are where a standard model Higgs has been excluded.

The two major effects of next-to-leading order quantum chromodynamics on the extraction of the W mass have been estimated: the contribution of initial state gluon emission to the transverse momentum of W bosons and the effect of higher-order QCD on the W boson angular distribution.

The uncertainty on M_W arising from initial state gluon emission is 6 MeV, 7 MeV and 8 MeV for the M_T^W, p_T^l and $\not\!\!E_T$ fits.[1] For the first time, the systematic effect of next-to-leading order QCD on the helicity of W bosons has been investigated and is found to be 3 MeV, 1 MeV and 4 MeV for the M_T^W, p_T^l and $\not\!\!E_T$ fits.

The effect of parton distribution functions (PDF) has been investigated, and the 1σ uncertainties arising from the MSTW2008 NLO global fit errors are 10 MeV, 1 MeV and 4 MeV for the M_T^W, p_T^l and $\not\!\!E_T$ fits. The 1σ uncertainties from CTEQ6.6 are measured to be 12 MeV, 10 MeV and 12 MeV for the

[1] Final uncertainties have been rounded up to the nearest MeV.

	Electron		Muon	
	200 pb^{-1}	2.3 fb^{-1}	200 pb^{-1}	2.3 fb^{-1}
Momentum scale	17	10	17	10
Energy scale	25	8	—	—
Backgrounds	8	6	9	5
PDFs	11	10	11	10
Electroweak corrections	11	5	12	5
Statistical	48	15	54	16

Table 9.1: A comparison of the larger systematic effects between the previous M_W measurement at CDF and the measurement in preparation. Excluded systematics are in progress and were less than 10 MeV in the 200 pb^{-1} measurement. The uncertainty arising from PDFs remains relatively unchanged compared with other systematics.

M_T^W, p_T^l and $\not\!\!E_T$ fits. In addition, the first investigation of the effect of NNLO PDF sets on the W mass measurement at CDF has been performed, and the systematic contribution is estimated to be 6 MeV, 5 MeV and 7 MeV for the M_T^W, p_T^l and $\not\!\!E_T$ fits.

Precision measurements of M_W are reaching a point where systematic errors are largely unaffected by statistics, and theoretical errors begin to dominate the expected total uncertainty. The uncertainty of PDF sets is fast becoming one of the biggest sources of error in the efforts to reduce the M_W uncertainty and is a common error between CDF and DØ in Tevatron mass combinations. The importance of these PDF uncertainties, to be used in the current M_W measurement in preparation at CDF, should not be underestimated. Table 9.1 shows how several of the larger systematic effects in the M_W measurement are expected to reduce with increased data, but the contribution of PDF uncertainty remains stable. In general, PDF uncertainties will become more important in future measurements.

Furthermore, the effect of higher-order QCD on M_W should not be discounted. The total systematic uncertainty arising from initial state gluon radiation and higher-order corrections to the angular distribution of W bosons

is 9 MeV. This includes the 6 GeV arising from NNLO PDFs which may partially cancel out when NNLO perturbative QCD generators become more widespread. There is no generator using a resummed calculation in the non-perturbative regime matched to NNLO QCD, and a significant number of W bosons detected at CDF have a low transverse momentum. This makes the future prospect of determining the full impact of NNLO QCD on M_W difficult or incomplete.

In addition, the transverse momentum of Z^0 bosons arising from initial state gluon radiation has been constrained in the electron and muon channels. The g_2 parameter has been extracted and is found to be 0.623 ± 0.014 GeV^2 albeit with a χ^2/ndf of 180/117. Adding an additional parameter, ξ, improves the fit agreement and obtains $g_2 = 0.721 \pm 0.018$ GeV^2 and $\xi = 0.117 \pm 0.001$ with a χ^2/ndf of 139/116. This improvement in the fit suggests that constraining additional BLNY parameters using Tevatron data may provide a better description of the transverse momentum of Z^0 bosons in future work.

Finally, $Z^0 \rightarrow e^+e^-$ data has been unfolded and $g_2 = 0.733 \pm 0.038$ GeV^2 extracted for $\xi = 0.117$. Two alternative kinematic variables proposed to replace p_T^Z have been investigated but are found to be inferior to p_T^Z for determining g_2 at CDF.

In conclusion, the contribution of a number of effects to the measurement of M_W at CDF has been investigated. The uncertainty as a result from next-to-leading order quantum chromodynamics arises through the transverse momentum of W bosons and the angular momentum of the bosons. The effect of both on the W boson mass has been determined. The contribution of patron distribution functions to the measurement of the W boson mass has been investigated and found to be of increasing importance in the current measurement and that of future work.

References

[1] S. Abachi *et al.* [D0 Collaboration], "Observation Of The Top Quark," Phys. Rev. Lett. **74**, 2632 (1995) [arXiv:hep-ex/9503003].

[2] F. Abe *et al.* [CDF Collaboration], "Observation Of Top Quark Production In $\bar{p}p$ Collisions," Phys. Rev. Lett. **74**, 2626 (1995) [arXiv:hep-ex/9503002].

[3] S. Ansoldi *et al.*, "What Comes Beyond The Standard Models. Proceedings, 9th Workshop, Bled, Slovenia, September 16-26, 2006," [arXiv:hep-ph/0612250].

[4] K. Nakamura *et al.* [Particle Data Group], "Review Of Particle Physics," J. Phys. G **37**, 075021 (2010).

[5] T. Aaltonen *et al.* [CDF Collaboration], "Search For New Particles Leading To $Z+$ Jets Final States In $p\bar{p}$ Collisions At $\sqrt{s} = 1.96$-TeV," Phys. Rev. D **76**, 072006 (2007) [arXiv:hep-ex/0706.3264].

[6] V. M. Abazov *et al.* [D0 Collaboration], "Search For Long-lived Particles Decaying Into Electron Or Photon Pairs With The D0 Detector," Phys. Rev. Lett. **101**, 111802 (2008) [arXiv:hep-ex/0806.2223].

[7] T. Aaltonen *et al.* [CDF Collaboration], "Search For Heavy Top-like Quarks Using Lepton Plus Jets Events In 1.96-TeV $p\bar{p}$ Collisions," Phys. Rev. Lett. **100**, 161803 (2008) [arXiv:hep-ex/0801.3877].

[8] Z. Maki, M. Nakagawa and S. Sakata, "Remarks On The Unified Model Of Elementary Particles," Prog. Theor. Phys. **28**, 870 (1962).

[9] Y. Fukuda *et al.* [Super-Kamiokande Collaboration], "Evidence For Oscillation Of Atmospheric Neutrinos," Phys. Rev. Lett. **81**, 1562 (1998) [arXiv:hep-ex/9807003].

[10] Q. R. Ahmad *et al.* [SNO Collaboration], "Direct Evidence For Neutrino Flavor Transformation From Neutral-current Interactions In The Sudbury Neutrino Observatory," Phys. Rev. Lett. **89**, 011301 (2002) [arXiv:nucl-ex/0204008].

[11] R. K. Ellis, W. J. Stirling, and B. R. Webber. *QCD And Collider Physics.* Cambridge University Press, 2003.

[12] S. L. Glashow, "Partial Symmetries Of Weak Interactions," Nucl. Phys. **22**, 579 (1961).

[13] S. Weinberg, "A Model Of Leptons," Phys. Rev. Lett. **19**, 1264 (1967).

[14] A. Salam and J. A. Strathdee, "A Renormalizable Gauge Model Of Lepton Interactions," Nuovo Cim. **11A**, 397 (1972).

[15] N. Cabibbo, "Unitary Symmetry nd Leptonic Decays," Phys. Rev. Lett. **10**, 531 (1963).

[16] M. Kobayashi and T. Maskawa, "CP Violation In The Renormalizable Theory Of Weak Interaction," Prog. Theor. Phys. **49**, 652 (1973).

[17] G. Arnison *et al.* [UA1 Collaboration], "Experimental Observation Of Isolated Large Transverse Energy Electrons With Associated Missing Energy At $\sqrt{s} = 540$ GeV," Phys. Lett. B **122**, 103 (1983).

[18] G. Arnison *et al.* [UA1 Collaboration], "Experimental Observation Of Lepton Pairs Of Invariant Mass Around 95 GeV At The CERN SPS Collider," Phys. Lett. B **126**, 398 (1983).

[19] M. Banner *et al.* [UA2 Collaboration], "Observation Of Single Isolated Electrons Of High Transverse Momentum In Events With Missing Transverse Energy At The CERN Anti-p p Collider," Phys. Lett. B **122**, 476 (1983).

[20] P. Bagnaia *et al.* [UA2 Collaboration], "Evidence For $Z^0 \to e^+e^-$ At The CERN Anti-p p Collider," Phys. Lett. B **129**, 130 (1983).

[21] R. Barate *et al.* [LEP Working Group for Higgs boson searches and ALEPH Collaboration and DELPHI Collaboration and L3 Collaboration and OPAL Collaboration], "Search For The Standard Model Higgs Boson At LEP," Phys. Lett. B **565**, 61 (2003) [arXiv:hep-ex/0306033].

[22] T. Aaltonen *et al.* [CDF and D0 Collaborations], "Combination Of Tevatron Searches For The Standard Model Higgs Boson In The W+W- Decay Mode," Phys. Rev. Lett. **104**, 061802 (2010) [arXiv:hep-ex/1001.4162].

[23] [The TEVNPH Working Group of the CDF and D0 Collaborations], "Combined CDF And D0 Upper Limits On Standard Model Higgs-Boson Production With Up To 6.7 fb^{-1} Of Data," [arXiv:hep-ex/1007.4587].

[24] W. W. Armstrong *et al.* [ATLAS Collaboration], "ATLAS: Technical Proposal For A General-purpose p p Experiment At The Large Hadron Collider At CERN," CERN-LHCC-94-43

[25] G. L. Bayatian *et al.* [CMS Collaboration], "CMS Technical Design Report, Volume II: Physics Performance," J. Phys. G **34**, 995 (2007).

[26] Fermi National Accelerator Laboratory, Accessed August 2010. `http://www.fnal.gov/pub/about/whatis/mission.html`.

[27] Fermilab Visual Media Services, Fermilab Accelerator Chain - Schematic drawing of Accelerator Complex, 00-0635D.

[28] The Northern Illinois University Institute for Neutron Therapy at Fermilab, Accessed September 2010. `http://www.neutrontherapy.niu.edu/neutrontherapy/`.

[29] S. E. Kopp, "The NuMI neutrino Beam At Fermilab," [arXiv:physics/0508001].

[30] Tevatron luminosity summary plots, Accessed August 2010. `http://www.fnal.gov/pub/now/tevlum.html`.

[31] F. Abe *et al.* [CDF Collaboration], "The CDF Detector: An Overview," Nucl. Instrum. Meth. A **271**, 387 (1988).

[32] R. Blair *et al.* [CDF-II Collaboration], "The CDF-II Detector: Technical Design Report," FERMILAB-PUB-96-390-E

[33] P. T. Lukens [CDF IIb Collaboration], "The CDF IIb Detector: Technical Design Report," CDF-DOC-CDF-PUBLIC-6261

[34] T. K. Nelson [CDF Collaboration], "The CDF-II Silicon Tracking System," Nucl. Instrum. Meth. A **485**, 1 (2002).

[35] J. Antos *et al.*, "The SVX II Silicon Vertex Detector Upgrade At CDF," Nucl. Instrum. Meth. A **383**, 13 (1996).

[36] A. A. Affolder *et al.*, "Construction Report Of The Intermediate Silicon Layers (ISL) Ladders," Nucl. Instrum. Meth. A **461**, 216 (2001).

[37] A. A. Affolder *et al.* [CDF Collaboration], "CDF Central Outer Tracker," Nucl. Instrum. Meth. A **526**, 249 (2004).

[38] M. E. Binkley *et al.*"Aging In Large CDF Tracking Chambers," Nucl. Instrum. Meth. A **515**, 53 (2003).

[39] R. S. Lu [CDF Collaboration], "Operation Aspects Of CDF Tracking And Vertexing Detectors," Nucl. Instrum. Meth. A **566**, 114 (2006).

[40] T. Aaltonen *et al.* [CDF Collaboration], "First Run II Measurement Of The W Boson Mass," Phys. Rev. D **77**, 112001 (2008) [arXiv:hep-ex/0708.3642].

[41] L. Balka *et al.* [CDF Collaboration], "The CDF Central Electromagnetic Calorimeter," Nucl. Instrum. Meth. A **267**, 272 (1988).

[42] F. Abe *et al.* [CDF Collaboration], "A Measurement Of The Ratio $\sigma \times B(p\bar{p} \to W \to e\nu)/\sigma \times B(p\bar{p} \to Z^0 \to ee)$ In $p\bar{p}$ Collisions At $\sqrt{s} = 1800$ GeV," Phys. Rev. D **52**, 2624 (1995)

[43] S. Bertolucci *et al.* [CDF Collaboration], "The CDF Central And Endwall Hadron Calorimeter," Nucl. Instrum. Meth. A **267**, 301 (1988).

[44] G. Ascoli *et al.*, "CDF Central Muon Detector," Nucl. Instrum. Meth. A **268**, 33 (1988).

[45] A. Artikov *et al.*, "Design And Construction Of New Central And Forward Muon Counters for CDF II," Nucl. Instrum. Meth. A **538**, 358 (2005) [arXiv:physics/0403079].

[46] H. Frisch *et al.*, "Conceptual Design Of A Deadtimeless Trigger For The CDF Upgrade," CDF-DOC-TRIGGER-CDFR-2038 (1993).

[47] CDF Summary of Stores, Accessed August 2010. `http://www-cdfonline.fnal.gov/ops/opshelp/stores/`.

[48] M. J. G. Veltman, "Second Threshold In Weak Interactions," Acta Phys. Polon. B **8**, 475 (1977).

[49] LEP/TEV EW WG Plots for Summer 2010, Accessed August 2010. `http://lepewwg.web.cern.ch/LEPEWWG/plots/summer2010/`.

[50] J. Alcaraz [ALEPH Collaboration and CDF Collaboration and D0 Collaboration and DELPHI Collaboration and L3 Collaboration and OPAL Collaboration and SLD Collaboration], "Precision Electroweak Measurements And Constraints On The Standard Model," [arXiv:hep-ex/0911.2604].

[51] A. B. Arbuzov *et al.*, "ZFITTER: A Semi-Analytical Program For Fermion Pair Production In e+ e- Annihilation, From Version 6.21 To Version 6.42," Comput. Phys. Commun. **174**, 728 (2006) [arXiv:hep-ph/0507146].

[52] P. Renton, "Global Electroweak Fits and the Higgs Boson Mass," [arXiv:hep-ph/0809.4566].

[53] W. K. Sakumoto, "Event $|Z_{\rm vtz}| \leq 60$ cm Cut Acceptance For Run II," CDF-ANAL-ELECTROWEAK-CDFR-8318 (2006).

[54] T. Aaltonen *et al.* [CDF Collaboration], "A Direct Measurement Of The W Boson Width In $p\bar{p}$ Collisions At $\sqrt{s} = 1.96$ TeV," Phys. Rev. Lett. **100**, 071801 (2008) [arXiv:hep-ex/0710.4112].

[55] GEANT3 Detector Description And Simulation Tool. *CERN Program Writeup W5013*, 1993.

[56] I. Bizjak *et al.*, "An Improved Measurement Of The W Boson Mass With CDF In Run II : First Plots Of The Data," CDF-ANAL-ELECTROWEAK-CDFR-9328 (2008).

[57] S. D. Drell and T. M. Yan, "Massive Lepton Pair Production In Hadron-Hadron Collisions At High-Energies," Phys. Rev. Lett. **25**, 316 (1970) [Erratum-ibid. **25**, 902 (1970)].

[58] C. M. Carloni Calame, G. Montagna, O. Nicrosini and A. Vicini, "Precision Electroweak Calculation Of The Production Of A High Transverse-momentum Lepton Pair At Hadron Colliders," JHEP **0710**, 109 (2007) [arXiv:hep-ph/0710.1722].

[59] P. B. Arnold, R. K. Ellis, and M. H. Reno, "High p_T W And Z Production At The Tevatron," Phys. Rev. D **40**, 912 (1989)

[60] G. A. Ladinsky and C. P. Yuan, "The Nonperturbative Regime In QCD Resummation For Gauge Boson Production At Hadron Colliders," Phys. Rev. D **50**, 4239 (1994) [arXiv:hep-ph/9311341].

[61] M. R. Whalley, D. Bourilkov and R. C. Group, "The Les Houches Accord PDFs (LHAPDF) And Lhaglue," [arXiv:hep-ph/0508110].

[62] C. M. Carloni Calame, G. Montagna, O. Nicrosini and A. Vicini, "Precision Electroweak Calculation Of The Charged Current Drell-Yan Process," JHEP **0612**, 016 (2006) [arXiv:hep-ph/0609170].

[63] U. Baur and D. Wackeroth, "Electroweak Radiative Corrections To $p\bar{p} \to W^{\pm} \to \ell^{\pm}\nu$ Beyond The Pole Approximation," Phys. Rev. D **70**, 073015 (2004) [arXiv:hep-ph/0405191].

[64] C. Buttar *et al.*, "Les Houches Physics At TeV Colliders 2005, Standard Model And Higgs Working Group: Summary report," [arXiv:hep-ph/0604120].

[65] C. E. Gerber *et al.* [TeV4LHC-Top and Electroweak Working Group], "Tevatron-for-LHC Report: Top And Electroweak Physics," [arXiv:hep-ph/0705.3251].

[66] G. Balossini *et al.*, "Combination Of Electroweak And QCD corrections To Single W Production At The Fermilab Tevatron And The CERN LHC," JHEP **1001**, 013 (2010) [arXiv:hep-ph/0907.0276].

[67] J. C. Collins, D. E. Soper and G. F. Sterman, "Transverse Momentum Distribution In Drell-Yan Pair And W And Z Boson Production," Nucl. Phys. B **250**, 199 (1985).

[68] C. T. H. Davies, B. R. Webber and W. J. Stirling, "Drell-Yan Cross-Sections At Small Transverse Momentum," Nucl. Phys. B **256**, 413 (1985).

[69] F. Landry, R. Brock, G. Ladinsky and C. P. Yuan, "New Fits For The Non-perturbative Parameters In The CSS Resummation Formalism," Phys. Rev. D **63**, 013004 (2001) [arXiv:hep-ph/9905391].

[70] F. Landry, R. Brock, P. M. Nadolsky and C. P. Yuan, "Tevatron Run-1 Z Boson Data And Collins-Soper-Sterman Resummation Formalism," Phys. Rev. D **67**, 073016 (2003) [arXiv:hep-ph/0212159].

[71] P. B. Arnold and R. P. Kauffman, "W And Z Production At Next-to-leading Order: From Large Q_T To Small," Nucl. Phys. B **349**, 381 (1991).

[72] E. Mirkes, "Angular Decay Distribution Of Leptons From W Bosons At NLO In Hadronic Collisions," Nucl. Phys. B **387**, 3 (1992).

[73] S. Agostinelli *et al.* [GEANT4 Collaboration], "GEANT4: A Simulation Toolkit," Nucl. Instrum. Meth. A **506**, 250 (2003).

[74] K. Rinnert. "A Fast-Access Material Map For The SVX II/ISL Silicon Tracking Volume at CDF 2,". CDF-DOC-BOTTOM-PUBLIC-5846 (2002).

[75] A. B. Migdal, "Bremsstrahlung And Pair Production In Condensed Media At High-Energies," Phys. Rev. **103**, 1811 (1956).

[76] W. T. Giele, E. W. N. Glover and D. A. Kosower, "Higher Order Corrections To Jet Cross-sections In Hadron Colliders," Nucl. Phys. B **403**, 633 (1993) [arXiv:hep-ph/9302225].

[77] CTEQ Meta Page, August 2010. `http://www.phys.psu.edu/~cteq/`.

[78] MRS/MRST/MSTW Parton Distributions, August 2010. `http://durpdg.dur.ac.uk/hepdata/mrs.html`.

[79] A. A. Affolder *et al.* [CDF Collaboration], "Measurement Of The W Boson Mass With The Collider Detector At Fermilab," Phys. Rev. D **64**, 052001 (2001) [arXiv:hep-ex/0007044].

[80] V. M. Abazov *et al.* [D0 Collaboration], "Improved W Boson Mass Measurement With The DØ Detector," Phys. Rev. D **66**, 012001 (2002) [arXiv:hep-ex/0204014].

[81] V. M. Abazov *et al.* [D0 Collaboration], "Measurement Of The W Boson Mass," Phys. Rev. Lett. **103**, 141801 (2009) [arXiv:hep-ex/0908.0766].

[82] [Tevatron Electroweak Working Group and CDF Collaboration and D0 Collaboration], "Updated Combination Of CDF And D0 Results For The Mass Of The W Boson," [arXiv:hep-ex/0908.1374].

[83] [Tevatron Electroweak Working Group and CDF Collaboration and D0 Collaboration], "Combination Of CDF And D0 Results On The W Boson Mass And Width," [arXiv:hep-ex/0808.0147].

[84] J. Pumplin, D. R. Stump, J. Huston, H. L. Lai, P. M. Nadolsky and W. K. Tung, "New Generation Of Parton Distributions With Uncertainties From Global QCD Analysis," JHEP **0207**, 012 (2002) [arXiv:hep-ph/0201195].

[85] A. D. Martin, R. G. Roberts, W. J. Stirling and R. S. Thorne, "Uncertainties Of Predictions From Parton Distributions. 1: Experimental Errors," Eur. Phys. J. C **28**, 455 (2003) [arXiv:hep-ph/0211080].

[86] A. D. Martin, W. J. Stirling, R. S. Thorne and G. Watt, "Parton Distributions For The LHC," Eur. Phys. J. C **63**, 189 (2009) [arXiv:hep-ph/0901.0002].

[87] J. Pumplin *et al.*, "Uncertainties Of Predictions From Parton Distribution Functions. 2. The Hessian Method," Phys. Rev. D **65**, 014013 (2001) [arXiv:hep-ph/0101032].

[88] J. Strologas and S. Errede, "Study Of The Angular Coefficients And Corresponding Helicity Cross Sections Of The W Boson In Hadron Collisions," Phys. Rev. D **73**, 052001 (2006) [arXiv:hep-ph/0503291].

[89] V. Blobel, "An Unfolding Method For High Energy Physics Experiments," [arXiv:hep-ex/0208022].

[90] R. J. Barlow. *Statistics: A Guide To The Use Of Statistical Methods In The Physical Sciences*. Wiley, 1999.

[91] G. D'Agostini, "A Multidimensional Unfolding Method Based On Bayes' Theorem," Nucl. Instrum. Meth. A **362**, 487 (1995).

[92] RooUnfold: ROOT Unfolding Framework. `http://hepunx.rl.ac.uk/ adye/software/unfold/RooUnfold.html`.

[93] M. Vesterinen and T. R. Wyatt, "A Novel Technique For Studying The Z Boson Transverse Momentum Distribution At Hadron Colliders," Nucl. Instrum. Meth. A **602**, 432 (2009) [arXiv:hep-ex/0807.4956].

[94] T. Aaltonen *et al.* [CDF Collaboration], "Diffractive W And Z Production At The Fermilab Tevatron," [arXiv:hep-ex/1007.5048].

[95] T. A. Aaltonen *et al.* [CDF Collaboration], "Measurement Of $d\sigma/dy$ Of Drell-Yan e^+e^- Pairs In The Z Mass Region From $p\bar{p}$ Collisions At $\sqrt{s} =$ 1.96 TeV," Phys. Lett. B **692**, 232 (2010) [arXiv:hep-ex/0908.3914].

[96] R. Thorne, Talk given at PDF4LHC Meeting, July 2010. `http://indico.cern.ch/conferenceDisplay.py?confId=98883`.

[97] R. Hamberg, W. L. van Neerven and T. Matsuura, "A Complete Calculation Of The Order $\alpha - s^2$ Correction To The Drell-Yan K Factor," Nucl. Phys. B **359**, 343 (1991) [Erratum-ibid. B **644**, 403 (2002)].

[98] C. Anastasiou, L. J. Dixon, K. Melnikov and F. Petriello, "High Precision QCD At Hadron Colliders: Electroweak Gauge Boson Rapidity Distributions At NNLO," Phys. Rev. D **69**, 094008 (2004) [arXiv:hep-ph/0312266].

[99] S. Bethke, "The 2009 World Average Of $\alpha_s(M_Z)$," Eur. Phys. J. C **64**, 689 (2009) [arXiv:hep-ph/0908.1135].

[100] A. V. Konychev and P. M. Nadolsky, "Universality Of The Collins-Soper-Sterman Nonperturbative Function In Gauge Boson Production," Phys. Lett. B **633**, 710 (2006) [arXiv:hep-ph/0506225].

[101] V. M. Abazov *et al.* [D0 Collaboration], "Measurement Of The Shape Of The Boson Transverse Momentum Distribution In $p\bar{p} \to Z/\gamma^* \to e^+e^- + X$ Events Produced At $\sqrt{s}$=1.96-TeV," Phys. Rev. Lett. **100**, 102002 (2008) [arXiv:hep-ex/0712.0803].

[102] M. G. Albrow *et al.* [TeV4LHC QCD Working Group], "Tevatron-for-LHC Report Of The QCD Working Group," [arXiv:hep-ph/0610012].